

# **Dark Matter Searches and Measurement of the Cosmic Muon Flux with the LUX-ZEPLIN (LZ) experiment**

---

**Dissertation**

**zur**

**Erlangung der naturwissenschaftlichen Doktorwürde  
(Dr. sc. nat.)**

**vorgelegt der**

**Mathematisch-naturwissenschaftlichen Fakultät**

**der**

**Universität Zürich**

**von**

Harvey J. Birch

**aus**

dem Vereinigten Königreich

**Promotionskommission**

Prof. Dr. Björn Penning (Vorsitz)

Prof. Dr. Laura Baudis

Prof. Dr. Ben Kilminster

**Zürich, 2025**

# **Abstract**

Abstract goes here

# **Dedication**

Always for you.  
KJCB

# **Declaration**

I declare that..

# **Acknowledgements**

I want to thank...

# Contents

<b>1</b>	<b>Introduction</b>	<b>8</b>
1.1	Evidence for Dark Matter . . . . .	8
1.2	Candidates for Dark Matter . . . . .	8
1.3	Direct Detection of Dark Matter . . . . .	8
<b>2</b>	<b>The LUX-ZEPLIN Dark Matter Experiment</b>	<b>9</b>
2.1	Liquid Xenon Time Projection Chamber . . . . .	10
2.1.1	Particle-Xenon interactions within a TPC . . . . .	10
2.1.2	NR and ER Discrimination . . . . .	12
2.2	Xenon Skin . . . . .	12
2.3	Outer Detector . . . . .	13
2.3.1	Liquid Scintillator . . . . .	14
2.3.2	PMT system . . . . .	15
2.3.3	Outer Detector Optical Calibration System . . . . .	15
2.4	Calibration Systems and Sources . . . . .	18
2.5	Data Acquisition System . . . . .	20
2.6	Simulation Techniques . . . . .	21
2.7	Assembly and Operation of the LZ Detector . . . . .	23
<b>3</b>	<b>Outer Detector Commissioning and Monitoring</b>	<b>24</b>
3.1	OD PMT Calibration . . . . .	24
3.1.1	Single Photo-electron Response Model . . . . .	24
3.1.2	Single Photo-electron Calibration . . . . .	25
3.2	Reconstructed Gain . . . . .	26
3.2.1	Monitoring PMT Response Over Time . . . . .	27
3.2.2	Gain Curves . . . . .	28
3.3	Trigger Efficiency . . . . .	28
3.4	Optical Calibration System Development . . . . .	28
3.4.1	UV LED commissioning . . . . .	28
3.4.2	Monitoring PMT . . . . .	28
<b>4</b>	<b>Veto Efficiency Studies</b>	<b>35</b>
4.1	Simulation Matching . . . . .	35
4.1.1	Tuning OD . . . . .	35
4.2	Veto Selection Optimisation . . . . .	35
4.2.1	Deadtime Stability . . . . .	38
4.3	Neutron Veto Efficiency . . . . .	39
4.3.1	Efficiency Calculation . . . . .	39
4.3.2	Neutrons From Calibration Sources . . . . .	39
4.3.3	Simulated Neutrons From Calibration Source . . . . .	50
4.3.4	Background Neutrons . . . . .	52
4.3.5	Background Neutron Efficiency From Data . . . . .	53
4.4	Veto Efficiency and the WIMP search . . . . .	55

<b>5 Muons</b>	<b>57</b>
5.1 Veto for WIMP Search . . . . .	57
5.1.1 Motivation . . . . .	57
5.1.2 Cut Description . . . . .	57
5.2 Flux Measurement . . . . .	57
5.2.1 Outline of Model . . . . .	57
5.2.2 Data selection . . . . .	59
5.2.3 NEST - Muon Simulations and Light-Energy Conversion . . . . .	61
5.2.4 Comparison Between Data and Simulation . . . . .	64
5.2.5 Muon Rate Results . . . . .	66
5.2.6 Reconstruction of the Muon Flux . . . . .	68
5.2.7 Evaluation of Average Rock Density . . . . .	69
5.3 Modulation . . . . .	69
5.3.1 Muon Pulse Shape in the Outer Detector . . . . .	69
5.3.2 MMS Analysis . . . . .	69
<b>6 Conclusion</b>	<b>71</b>
<b>Bibliography</b>	<b>72</b>

# List of Figures

2.1	Schematic of the LZ detector showcasing the major subsystems. At the center is the liquid xenon TPC (1), monitored by two arrays of PMTs and serviced by various cable and fluid conduits (upper and lower). The TPC is contained in a double-walled vacuum insulated titanium cryostat and surrounded on all sides by a GdLS Outer Detector (2). The cathode high voltage connection is made horizontally at the lower left (5). The GdLS is observed by a suite of 8" PMTs (3) standing in the water (4) which provides shielding for the detector. The pitched conduit on the right (6) allows for neutron calibration sources to illuminate the detector [2].	9
2.2	Dual phase liquid noble TPC operating principle and components. <b>2.2a:</b> Each particle interaction with the LXe atoms produces two signals: an initial prompt scintillation (S1) and a second, delayed one from ionisation (S2) [4]. The combination of these two signals allows for precise 3D position reconstruction and discrimination between nuclear and electron recoils. <b>2.2b:</b> CAD drawing of the TPC & Skin components: 1-Top PMT array; 2-Gate-anode and weir region (liquid level); 3-Side skin PMTs (1-inch); 4-Field cage; 5-Cathode ring; 6-Reverse field region; 7-Lower side skin PMTs (2-inch); 8-Dome skin PMTs (2-inch) [2]. <i>should I ref figures or use left/right?</i>	10
2.3	A schematic of the signal production and collection in a dual phase xenon time projection chamber.	11
2.4	Discrimination between ER and NR can be seen in LZ calibration events in $\log_{10}S2_c - S1_c$ for the tritium source (dark blue points, 5343 events) and the DD neutron source (orange points, 6324 events). Solid blue (red) lines indicate the median of the ER (NR) simulated distributions, and the dotted lines indicate the 10 % and 90 % quantiles. Thin gray lines show contours of constant electron-equivalent energy ( $keV_{ee}$ ) and nuclear recoil energy ( $keV_{nr}$ ) [11].	12
2.5	The Outer Detector vessels in an exploded view. The four large side vessels (SATs) are shown in green, the five small vessels (two top (TATs) and three bottom (BATs)) are shown in blue. The stainless steel base can be seen in grey and the foam water displacers in red. There is an additional small vessel shown in green at the top which is removed for photoneutron calibration source deployment [2].	13
2.6	Illustration of the multi-step $\gamma$ -ray emission of an excited $^{158}\text{Gd}^*$ following the thermal $^{157}\text{Gd}(n, \gamma)$ reaction. The de-excitation to the ground state can occur via many intermediate levels. Adapted from Ref.[14].	15
2.7	AmLi energy spectrum measured with LZ Outer Detector with coincident single scatter signals in the TPC, here simple data quality cuts have been applied. The distinctive hydrogen capture peak can be seen at 2.2 MeV, whilst the continuous $\gamma$ -ray spectrum from the Gd Capture has the expected end point at $\sim$ 8 MeV.	16
2.8	Plan view of the OD PMT support system. The 20 PMT ladders are mounted to a circular track attached to the walls of the water tank [4].	16
2.9	A comparison of the wavelength dependence of key optical parameters for both the GdLS and PMTs.	17

2.10 <b>Left:</b> A cross-section of a CAD drawing of the OD. The three heights of the 10 azimuthal positions of the optical fibre injection points are labelled 1-3. Two injection positions under the side acrylic tanks which point upwards are labelled 4 and 5. <b>Right:</b> A photograph of the OD PMT array showing the point of an injection point relatively to the surrounding PMTs. . . . .	17
2.11 Quality assurance measurement data taken during the commissioning of the acrylic tanks. The QA measurement data is the average transmission of light at a particular wavelength across 46 points. Vertical lines indicate the 390 nm and 435 nm LEDs with respect to the transmission of light. . . . .	18
2.12 A schematic of the OD OCS. An example of one Optical Calibration Card (OCC) is shown with its eight LED pulser boards and two photodiode boards. A total of five OCCs make up the OCS and are powered by a VME crate. Lines with arrows show the paths light takes down various fibres to different positions in the system. Labels 1-3 represent the three heights within the PMT array, while Label 4-5 denote the injection points to monitor the GdLS/acrylic, as shown in Figure 2.10. Adapted from Ref.[18, 19]. <b>NEED TO CHANGE THE COLOURS IN THIS SCHEMATIC!</b> . . . . .	19
2.13 A simplified schematic depicting how PMT signals are processed using the LZ DAQ system. Adapted from Ref.[23]. . . . .	21
2.14 Simulation framework for the LZ experiment. “Full” and “Fast” simulation chains are shown. Both chains begin with BACCARAT and end with an output LZap RQ file. . . . .	22
2.15 . . . . .	23
3.1 The response of the OD PMTs to 200k injections of 2000 photons during a monthly SPhE measurement. The pulse area is plotted against the start time of the pulse relative to the trigger plus the peak time relative to the start of the pulse. The OCS pulses are distributed around a peak of 560 ns. The two vertical dashed red lines indicate the inclusive timing selection criteria. . . . .	26
3.2 Pulse area distributions of PMT 800 from 200k OCS injections of 2000 photons during OD SPhE measurement. <b>Left:</b> Reconstructed pulse area measured in photons detected. <b>Right:</b> Pulse area taken from the area measured in the raw waveform in mVns, and converted to pC by dividing by the $50 \Omega$ termination at the amplifier. The fit applied in red is Equation 3.3 and the constants can be seen in the respective statistics boxes on each plot. . . . .	27
3.3 A scatter plot of the OD SPhE Area size measured in phd versus PMT ID for each OD PMT from a measurement taken on July 10th 2024. . . . .	29
3.4 A scatter plot of the OD SPhE Area size measured in mVns versus PMT ID for each OD PMT from a measurement taken on July 10th 2024. . . . .	30
3.5 A scatter plot of the OD PMT Gain versus PMT ID for each OD PMT from a measurement taken on July 10th 2024. . . . .	31
3.6 <b>Top:</b> A scatter plot of the relative change in OD PMT Gain over WS2022 science run. The reduced gain of PMT 811 can be seen in orange. <b>Bottom:</b> A scatter plot of the average relative change in OD PMT Gain across all OD PMTs over WS2022 science run. . . . .	32
3.7 <b>Top:</b> A scatter plot of the relative change in OD PMT Gain since the start of the WS2024 science run (until the time of writing). <b>Bottom:</b> A scatter plot of the average relative change in OD PMT Gain across all OD PMTs since the start of the WS2024 science run (until the time of writing). . . . .	33

3.8	<b>Top:</b> A scatter plot of the relative change in OD PMT Gain since the gain matching campaign in May 2024 (until the time of writing). <b>Bottom:</b> A scatter plot of the average relative change in OD PMT Gain across all OD PMTs since the gain matching campaign in May 2024 (until the time of writing). . . . .	34
4.1	Geometry in the simulation used for SR3. . . . .	36
4.2	An example of the plot used to compare neutron capture timing in data with the baseline simulation and the modified simulation. . . . .	36
4.3	Large scale canvas of all possible simulation configurations. Each plot is similar in style to Figure 4.2. Here AmLi at 700mm in CSD3 has been shown as an example.	37
4.4	Time difference between TPC single-scatter and Veto pulses. This is used to determine the prompt veto windows. . . . .	39
4.5	OD Prompt heatmap. The z-axis shows the efficiency associated with a given pulse requirement. The veto time window considered is [-300, 300]ns. . . . .	40
4.6	Skin Prompt heatmap. In each bin, either the pulse coincidence or the pulse threshold has been varied. The z-axis shows the efficiency associated with a given pulse requirement. The veto time window considered is [-250, 250]ns. . . . .	41
4.7	OD Delayed heatmap. In each bin, either the veto window or the pulse threshold has been varied. The z-axis shows the deadtime associated with a given veto window and pulse threshold. In addition to the pulse area threshold, the pulse must have a coincidence greater than 5. . . . .	42
4.8	Delayed vetoes heatmap. In each bin, the OD pulse threshold or the Skin pulse threshold has been varied. The z-axis shows the veto efficiency associated with a given pulse thresholds. In addition to the pulse area threshold, the OD pulse must have a coincidence greater than 5, and the Skin pulse greater than 2. The veto window in this case is $500\mu\text{s}$ . . . . .	43
4.9	Deadtime-vs-efficiency highlighting a number of considered cuts. At each point, the numbers in brackets are; the delayed veto window length after the TPC single-scatter, the Skin threshold pulse area, and the OD threshold pulse area. . . . .	44
4.10	Cuts determined to be optimal for SR3. The SR3 thresholds have a position correction in Z. The SR1 cuts are also included. . . . .	44
4.11	Deadtime from the Skin and OD veto cuts during each month of SR3. The error shown in purely statistical. . . . .	45
4.12	Rate of OD pulses above 200keV as defined by SR1 not SR3. . . . .	45
4.13	X-Y distribution of events in the TPC for AmLi sources positioned at 700mm. Each of the circular cuts are overlaid onto the plot. . . . .	46
4.14	The veto efficiency (from all analysis cuts) at using AmLi at 700mm. The ratio plot shows the less than 2% difference between method 1 and method 2. . . . .	47
4.15	The three different NR bands used for the NR-band cut for the respective sources, AmLi, DD and AmBe. . . . .	47
4.16	$P_a(> 0)$ <sub>all window</sub> AmLi Accidental correction factors for varying veto window size for different windows of interest. . . . .	49
4.17	$1 - P_a(> 0)$ <sub>anywindow</sub> AmLi Accidental correction factors for varying veto window size for different windows of interest. . . . .	49
4.18	The impact of the accidental correction applied to the different veto efficiencies for the given windows of interest. AmLi data at a height of 700 mm in CSD1 has been used here as an example. . . . .	49
4.19	$P_a(> 0)$ <sub>all window</sub> DD Accidental correction factors for varying veto window size for different windows of interest. . . . .	50
4.20	$1 - P_a(> 0)$ <sub>anywindow</sub> DD Accidental correction factors for varying veto window size for different windows of interest. . . . .	51

4.21	The impact of the accidental correction applied to the different veto efficiencies for the given windows of interest. . . . .	51
4.22	Inefficiency plots for AmLi, comparing simulations to data. Left: Total. Middle: Delayed Only. Right: OD Delayed. In each case, the average from all CSD positions are used. . . . .	51
4.23	Inefficiency plots for DD, comparing simulations to data. Left: Total. Middle: Delayed Only. Right: OD Delayed. . . . .	52
4.24	Efficiency for tagging a neutron on Detector-NR simulations. . . . .	52
4.25	Summary of efficiency from all simulations and calibration sources. The CSD sources are averaged at each height. Circle marks are from data. Start marks are from simulations. The driftTime is defined as when mean(driftTime) of events which pass all other cuts. . . . .	56
5.1	Angular distributions and the kinetic energy spectrum of muons at SURF, Davis Campus, as generated by the MUSUN model. . . . .	58
5.2	Event-viewer output of typical muon event. PMT saturation is evident towards the end of the muon ‘tail’ in the TPC. . . . .	59
5.3	Histograms of the largest OD pulse areas in $\sim$ 12.5 million background events from WS2022 before applying inter-detector timing cuts. Pulse shape has been used to differentiate between pulses produced by a muon and pulses produced by noise phenomena observed in the detector. The peak at around 450 phd results from neutron captures on the nuclei of hydrogen atoms and the subsequent emission of a single 2.22 MeV gamma ray. The plots show the impact of the 2000 phd cut and pulse shape cut (a) before and (b) after inter-detector timing coincidences are applied. . . . .	60
5.4	Inter-detector timing plots, these distributions were used in defining the timing selection following the skim of the WS2022 and WS2024 datasets looking at events with a pulse greater than 2000 phd in the Outer Detector. The figures depict (a) the time difference between the largest pulse in the Outer Detector and the largest pulse in the Skin; (b) the time difference between the largest pulse in the Outer Detector and the start of the muon tail in the TPC; and (c) the time difference between the largest pulse in the Skin and the start of the muon tail in the TPC. . . . .	62
5.5	(a) Histograms comparing the spectrum of deposited energy in the TPC from BACCARAT muons with the spectrum of deposited energy in the TPC from WS2022 and WS2024 HG (LG) data (converted from TPC total pulse area). (b) The ratios of HG (LG) WS2022 and WS2024 data to BACCARAT simulations as a function of the energy threshold in the TPC. . . . .	63
5.6	Energy deposition spectra of muon events from BACCARAT simulations with and without a muon particle ID (PID) cut. The cut selects events that had a muon depositing energy in the TPC directly. . . . .	63
5.7	Deposited energy from BACCARAT simulations versus the number of detected photons from NEST simulations. The minimum muon-like event found in data is overlaid at 574 phd and the spline fit is extrapolated down to this value. . . . .	64
5.8	Energy deposited by BACCARAT simulated muons in the OD and the energy of events in data converted from the total pulse area in the OD. . . . .	65
5.9	Energy depositions from events in the OD and TPC are shown, with the total pulse area from WS2022 and WS2024 data converted to energy. In (a), only OD and inter-detector timing cuts are applied, while in (b), the 10 MeV cut is also included. Similarly, BACCARAT simulations are plotted with the 8 MeV OD energy threshold and coincidence cut in (c), and with the additional 10 MeV cut included in (d). . . . .	66

5.10 The muon flux dependence on average rock density within the muon model. The horizontal line and shaded section mark, respectively, the measured flux value and the combined statistical and systematic errors,  $(5.119 \pm 0.094) \times 10^{-9} \text{ cm}^{-2}\text{s}^{-1}$ . 70

# List of Tables

2.1	Chemical components in 1L of GdLS, adapted from Ref.[13]. . . . .	14
2.2	A list of calibration source used by LZ for TPC, Skin and OD calibrations along with the purpose and method of deployment. The energy (keV) refers to particle energies relevant for the calibration of LZ and is not a complete list of decay energies. The energies quoted in the parentheses correspond to those of the particle species from the previous column. Adapted from Ref.[19, 17]. . . . .	19
4.1	ALPACA-Core SR3 cuts used on AmLi calibration data for determining the efficiency. Each cut is from SR3-cuts-v3. . . . .	48
4.2	ALPACA-Core SR3 cuts used on DD calibration data for determining the efficiency. Each cut is from SR3-cuts-v3. . . . .	50
4.3	ALPACA-Core SR3 cuts used on AmLi and DD simulations for determining the efficiency. Each cut is from SR3-cuts-v3. . . . .	50
4.4	ALPACA-Core SR3 cuts used on Detector-NR simulations for determining the efficiency. Each cut is from SR3-cuts-v3. . . . .	52
4.5	Summary of veto efficiencies. The Detector-NR Data value assumes that option 2 is used. . . . .	55
4.6	Summary of veto efficiencies and inefficiencies as determined from each approach. . . . .	55
5.1	Summary if relevant durations for the WIMP search runs. For this analysis, DAQ livetime was used in the rate calculation work. . . . .	59
5.2	Muon rates from simulations and WS2022 data. The data has the OD cuts and timing selections applied. The simulations have a 3-fold detector coincidence criteria and the 8 MeV OD energy cut applied. The TPC energy thresholds represent the total energy deposited by a muon event in the TPC. . . . .	67
5.3	Muon rates from simulations and WS2024 data. See the Table 5.2 caption for descriptions of the applied cuts and energy thresholds. . . . .	67
5.4	Muon rates from simulations, WS2022 and WS2024 data. See the Table 5.2 caption for descriptions of the applied cuts and energy thresholds. . . . .	68

# **1 Introduction**

**1.1 Evidence for Dark Matter**

**1.2 Candidates for Dark Matter**

**1.3 Direct Detection of Dark Matter**

## 2 The LUX-ZEPLIN Dark Matter Experiment

The LZ experiment is currently the leading dark matter direct detection experiment in the search for WIMPs [1]. The detector is located on the 4,850 ft level (4,300 m w.e) of the Sanford Underground Research Facility (SURF) in the Homestake Mine (Lead, SD) [2]. At the core of the experiment is a dual-phase Time Projection Chamber (TPC) which is sensitive to low-energy nuclear recoils (NR), the signal which is produced through WIMPs interacting with liquid noble gases. One of the main backgrounds in a WIMP search are neutrons as they also interact through nuclear recoils and thus LZ employs an active veto system to remove them. Theoretically WIMPs will only interact with the xenon target however neutrons would interact in both the TPC and veto detectors. The TPC is housed within a vacuum insulated cryostat with a layer of liquid xenon (the Skin) which acts as high voltage stand-off, this region is also instrumented with PMTs and is part of the active veto system. The liquid xenon (LXe) Skin is used to veto mostly gamma ray interactions within the TPC volume, whilst also being sensitive to neutrons. The cryostat is surrounded near hermetically by ten acrylic vessels filled with Gadolinium-loaded liquid scintillator (GdLS). The GdLS is observed by 120 PMTs and stands within 238t of DI water which provides shielding to the detector. A schematic of the detector is shown in Figure 2.1.

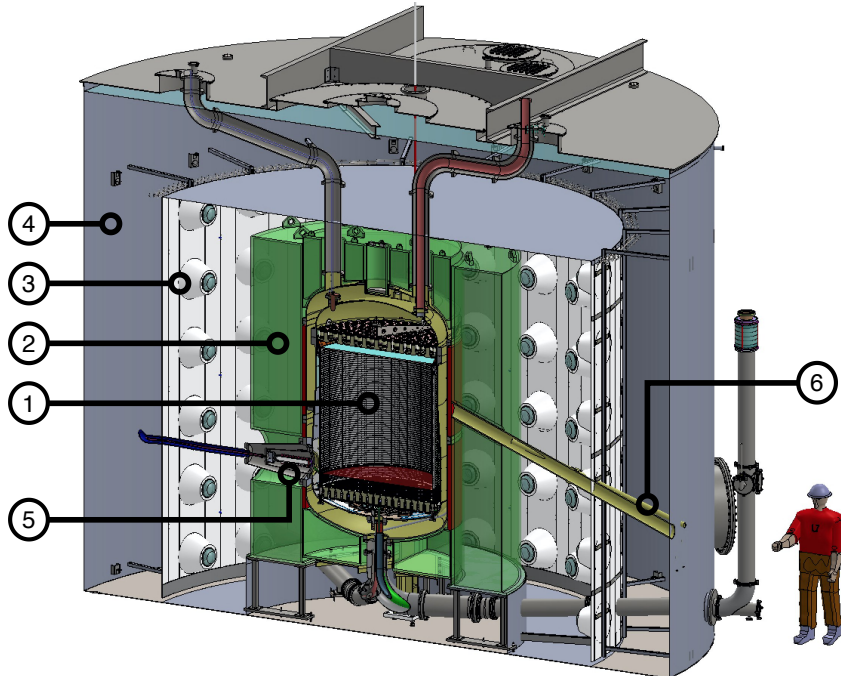


Figure 2.1: Schematic of the LZ detector showcasing the major subsystems. At the center is the liquid xenon TPC (1), monitored by two arrays of PMTs and serviced by various cable and fluid conduits (upper and lower). The TPC is contained in a double-walled vacuum insulated titanium cryostat and surrounded on all sides by a GdLS Outer Detector (2). The cathode high voltage connection is made horizontally at the lower left (5). The GdLS is observed by a suite of 8" PMTs (3) standing in the water (4) which provides shielding for the detector. The pitched conduit on the right (6) allows for neutron calibration sources to illuminate the detector [2].

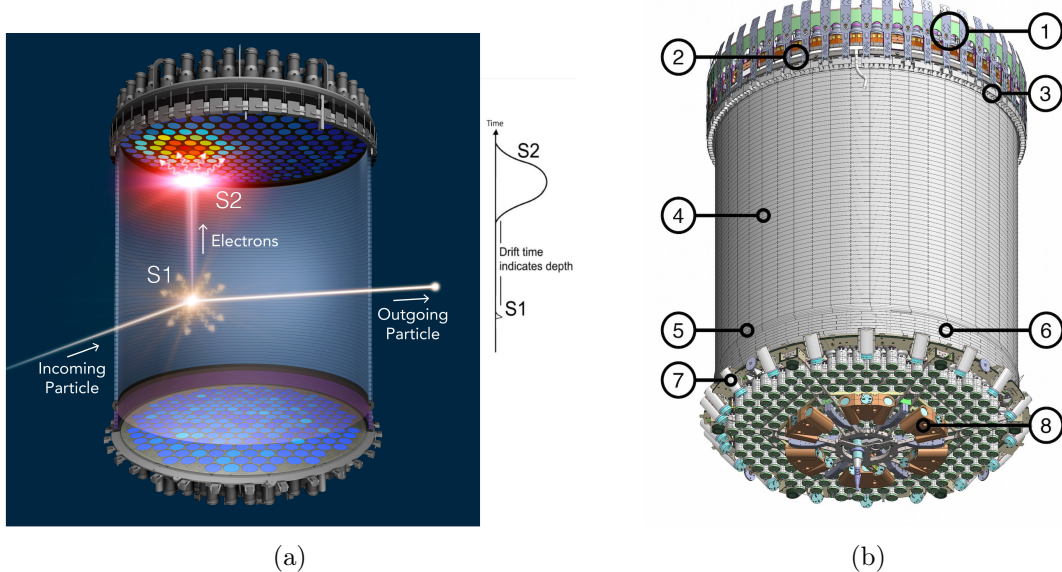


Figure 2.2: Dual phase liquid noble TPC operating principle and components. **2.2a:** Each particle interaction with the LXe atoms produces two signals: an initial prompt scintillation (S1) and a second, delayed one from ionisation (S2) [4]. The combination of these two signals allows for precise 3D position reconstruction and discrimination between nuclear and electron recoils. **2.2b:** CAD drawing of the TPC & Skin components: 1-Top PMT array; 2-Gate-anode and weir region (liquid level); 3-Side skin PMTs (1-inch); 4-Field cage; 5-Cathode ring; 6-Reverse field region; 7-Lower side skin PMTs (2-inch); 8-Dome skin PMTs (2-inch) [2]. **should I ref figures or use left/right?**

## 2.1 Liquid Xenon Time Projection Chamber

The LZ TPC holds 7 t (5.6 t fiducial) of LXe above its cathode, there is an additional thin layer (8 mm thick) of gaseous xenon (GXe) at the top of the liquid. The volume measures approximately 1.5 m in height and diameter and the walls of the TPC are made from PTFE to improve light collection efficiency [2]. The TPC, Skin and Xe payload are housed within the Inner Cryostat Vessel (ICV) and the Outer Cryostat Vessel (OCV) provides a vacuum jacket for insulation. Both cryostat vessels are made from low radioactivity titanium [3]. When a particle scatters off a LXe atom a prompt scintillation signal (S1) is produced alongside free electrons, via ionisation of the LXe atom. Through the application of an electric field, the free electrons drift to the LXe surface and are extracted in the GXe layer. As the electrons accelerate through the GXe layer, a proportional amount of scintillation light (S2) is produced. Light produced from these particle interactions is observed by a top and bottom array of 3-inch Hamamatsu R11410–22 PMTs, 494 in total. Using both the S1 and S2 signals, position reconstruction techniques can be used to determine the  $xyz$ -position of the particle interaction. The time difference between the S1 and S2 signals combined with the drift velocity is used to determine the  $z$ -position of the interaction whilst the hit pattern of the S2 signal in the top PMT array provides  $xy$ -position. The operating principle of a TPC can be seen in Figure 2.2a.

### 2.1.1 Particle-Xenon interactions within a TPC

As a particle traverses the LXe volume it can interact with either the atomic nucleus, producing a nuclear recoil (NR), or with the surrounding electron cloud, producing an electronic recoil (ER). Both processes result in the pair of signals discussed in Section 2.1. The S1 signal is produced via the following mechanism. The excited Xe atom,  $Xe^*$ , combines with a nearby ground state

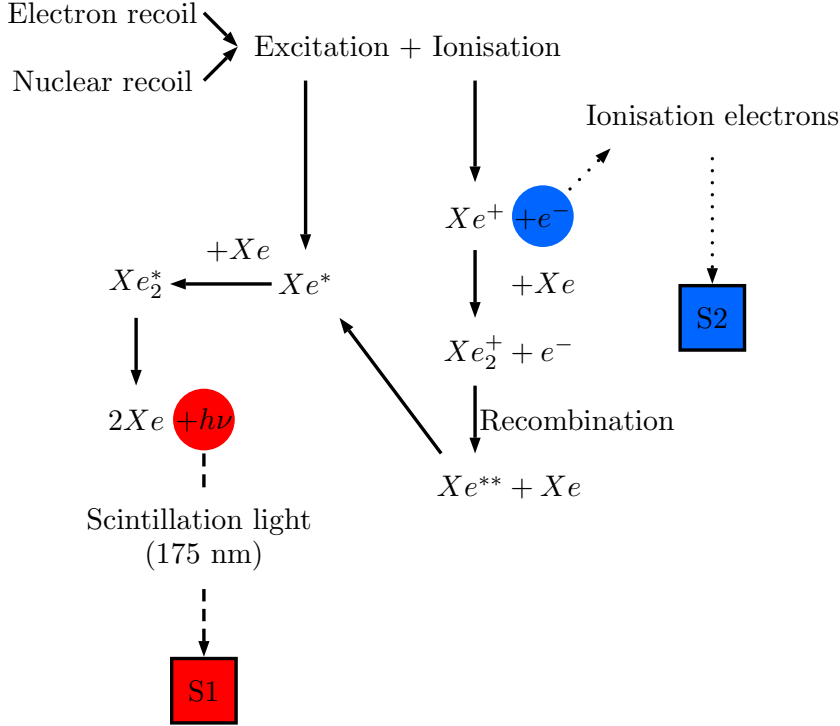


Figure 2.3: A schematic of the signal production and collection in a dual phase xenon time projection chamber.

$Xe$  atom to form an excimer state,  $Xe_2^{*\nu}$ , which is both an electronically and vibrationally excited molecule. Through collisions with other  $Xe$  atoms, energy in the vibrational modes of the excimer is lost. The excited pair de-excites further as the electronic excitation energy is released as a pair of vacuum-ultraviolet (VUV), at a mean wavelength of 178 nm [5]. The  $Xe$  atom also undergoes ionisation due to the displacement of the nucleus during the collision releasing electrons. A positively charged  $Xe^+$  ion combines with a neutral  $Xe$  atom to form a positively charged dimer  $Xe_2^+$ . Most of the electrons that are emitted in the ionisation are drifted away from the collision site by the applied electric field. However some of the ionised electrons produced in the cascade recombine with the molecule prior to it splitting to form a highly excited  $Xe$  atom. A final series of relaxation occurs in a similar manner to the excitation luminescence excimer. A schematic which describes the process of producing the S1 and S2 signal can be seen in Figure 2.3.

To understand what particle has passed through the LXe it is important to determine the energy deposited in interaction with the  $Xe$  atom. This can be described using the following equation:

$$E = \frac{W}{L} (n_{ex} + n_i) \quad (2.1)$$

Where  $W$  is the average energy required to produce either one scintillation photon or ionisation electron, which has been measured to be  $13.7 \pm 0.4$  eV [6, 7].  $L$  is referred to as the "Lindhard factor" or "quenching" accounting for the reduction of produced light and charge as energy is lost at heat. For electron recoils  $L$  is taken as unity, this implies that the heat-loss is constant with energy allowing it to be absorbed into the value of  $W$  [8]. The Lindhard factor for nuclear recoils is observed to be a function of deposited energy as the interaction energy is not linearly related to the observed total quanta [9].  $n_{ex}$  and  $n_i$  represent the number of excited atoms and ionised atoms respectively and are proportional to pulse area of the S1 and S2 pulses observed in the TPC respectively. The constants of proportionality are  $g_1$  and  $g_2$  and represent the S1 light collection efficiency and the electron extraction efficiency of the detector respectively. Thus

Equation 2.2 can be modified to describe the energy deposition using:

$$E = \frac{W}{L} \left( \frac{S1}{g_1} + \frac{S2}{g_2} \right) \quad (2.2)$$

### 2.1.2 NR and ER Discrimination

The ratio of energy distribution between light and charge differs between NRs and ERs. This can be directly observed through the S1 and S2 pulse areas produced from the interactions, particularly the ratio,  $\log_{10}(S2)/S1$ . This method demonstrates 95 % discrimination against ER with a 50 % NR acceptance [10]. This is key in the search for WIMPs where we would expect to observe an NR when a WIMP passes through the TPC. However, the dominant backgrounds such as  $\beta$ -decays from Rn daughter isotopes and  $^{85}\text{Kr}$  and  $\gamma$  radiation from detector components all produce ER events in the LXe. Both ER and NR events form distinctive band structure  $\log_{10}(S2)/S1$  space, as shown in Figure 2.4, where the width of the bands is due to electron-ion recombination at the interaction site whilst the overall separation is due to the ratio of ionisation to excitation in the interaction [7].

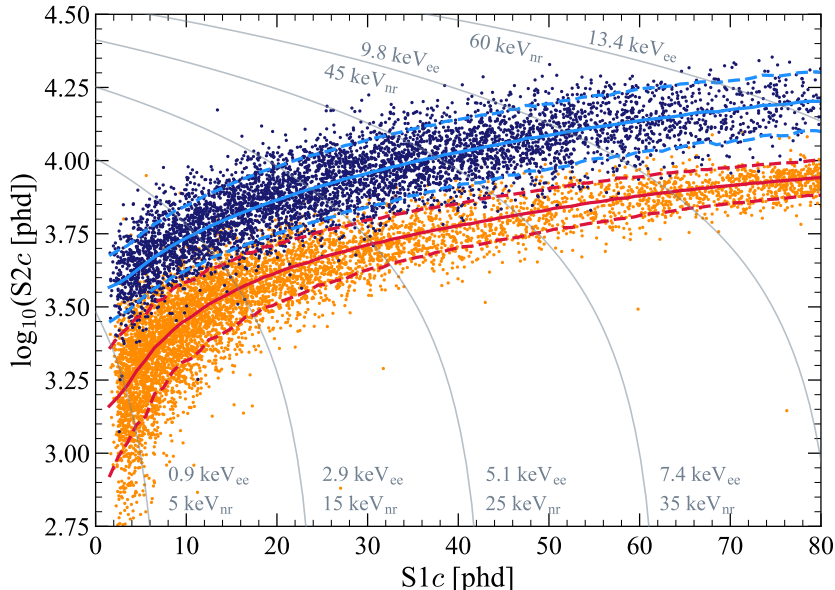


Figure 2.4: Discrimination between ER and NR can be seen in LZ calibration events in  $\log_{10}S2_c - S1_c$  for the tritium source (dark blue points, 5343 events) and the DD neutron source (orange points, 6324 events). Solid blue (red) lines indicate the median of the ER (NR) simulated distributions, and the dotted lines indicate the 10 % and 90 % quantiles. Thin gray lines show contours of constant electron-equivalent energy ( $\text{keV}_{\text{ee}}$ ) and nuclear recoil energy ( $\text{keV}_{\text{nr}}$ ) [11].

## 2.2 Xenon Skin

The TPC is surrounded by a layer of LXe, the region contains around 2 t of LXe between the field cage and the inner cryostat vessel [2]. The primary motivation for including this layer of LXe was to provide dielectric insulation between the two elements. Unlike Xenon-nT, LZ's main competitor, this region is instrumented for optical readout acting as a scintillation-only veto detector for gamma ray interactions in the TPC [12]. The region is nominally known as the "Skin" and can be split into two regions: Barrel and Dome. The Barrel contains 93 1-inch Hamamatsu R5820 PMTs at the top of the Barrel looking down and 38 2-inch Hamamatsu

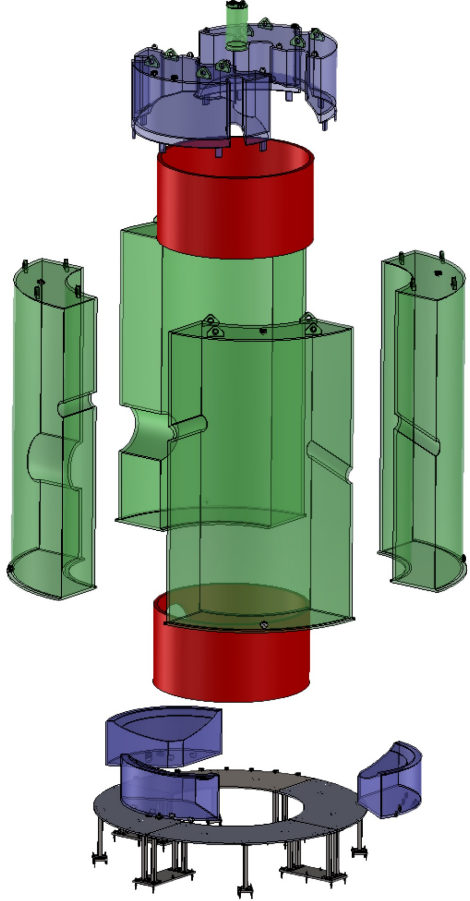


Figure 2.5: The Outer Detector vessels in an exploded view. The four large side vessels (SATs) are shown in green, the five small vessels (two top (TATs) and three bottom (BATs)) are shown in blue. The stainless steel base can be seen in grey and the foam water displacers in red. There is an additional small vessel shown in green at the top which is removed for photoneutron calibration source deployment [2].

R8778 PMTs; 20 at the bottom of the Barrel looking up, and 18 in the Dome region below the TPC [2]. The layout of the Skin PMTs with respect to the TPC can be seen in Figure 2.2b.

### 2.3 Outer Detector

It has been shown in previous sections that dual phase TPC has the capability to distinguish between ER and NR interactions in the LXe, however it does not have the capability to understand what particle caused the recoil. Neutrons are the primary source of NRs as they can easily scatter off the Xe nuclei and mimic a signal similar to a WIMP. Neutrons will however scatter multiple times in the TPC or nearby whereas WIMPs would not due to differences in their respective interaction cross sections. LZ has taken advantage of this principle and surrounded the TPC in a neutron detector to increase its discrimination power on NR backgrounds. This detector is nominally known as the Outer Detector. The outer cryostat housing the TPC is surrounded near hermetically by ten acrylic vessels filled with Gadolinium loaded liquid scintillator (GdLS). The GdLS is observed by 120 PMTs and stands within 238t of DI water which provides shielding to the detector. An exploded layout of these vessels can be seen in Figure 2.5.

Component	Molecular Formula	Mass [g/L]	Mass Fraction
LAB	C <sub>17.14</sub> H <sub>28.28</sub>	853.55	99.25
PPO	C <sub>15</sub> H <sub>11</sub> NO	3.00	0.35
bis-MSB	C <sub>24</sub> H <sub>22</sub>	0.01	0.0011
TMHA	C <sub>9</sub> H <sub>17</sub> O <sub>2</sub> <sup>-</sup>	2.58	0.003
Gd	Gd	0.86	0.1
GdLS	C <sub>17.072</sub> H <sub>28.128</sub> O <sub>0.0126</sub> N <sub>0.0037</sub> Gd <sub>0.0015</sub>	860.00	100

Table 2.1: Chemical components in 1L of GdLS, adapted from Ref.[13].

### 2.3.1 Liquid Scintillator

The primary detection medium for the OD is the GdLS, chosen for its excellent efficiency for neutrons and gammas that reach the OD [4]. The composition of the GdLS mixture is shown in Table 2.1. The base of the LS mixture is Linear-alkylbenzene (LAB), which acts as a solvent for the other components of the mixture. In addition to the LAB, the fluor 2,5-diphenyloxazole (PPO), and the wavelength shifter 1,4-bis(2-methylstyryl(benzene)) (Bis-MSB) are considered as the LS. As particles pass through the LS, the LAB component is excited as the particles deposit energy along the tracks. Through a series of chemical reactions, the excited LAB transmits energy to the fluor. As the excited fluor de-excites, it emits light with wavelengths up to 380 nm. Due to the short absorption lengths of the LS below 380 nm (approximately 1 m), Bis-MSB is included as a wavelength shifter. The Bis-MSB absorbs the photons produced by the fluor and emits photons with wavelengths between 410 nm - 425 nm with absorption lengths over 10 m. Bis-MSB is a crucial component of the mixture as wavelengths of the emitted photons overlap with the PMT sensitivity spectrum and absorption lengths satisfy the detector geometry. The mixture is additionally loaded with Gd with a mass fraction of 0.1 %. Gd has a very high ( $n, \gamma$ ) cross-section so improves both the efficiency and intensity of the neutron capture signal [4]. Due to the effectiveness of the Gd, only a small mass fraction is needed to dominate over neutron capture on protons in the LS. To dissolve the Gd in solution with the LS it is bound to a chelating agent, 3,5,5-trimethylhexanoic acid (TMHA) in a 3:1 ratio [4, 13].

### Neutron Capture in the OD

As previously mentioned, Gadolinium has the largest capture cross-section for thermal neutrons of any known stable elements: 49 kb [14]. This is due to contributions of two isotopes <sup>155</sup>Gd (61 kb) and especially <sup>157</sup>Gd (254 kb) [14]. After a thermal neutron captures on <sup>157</sup>Gd, the <sup>158</sup>Gd\* compound nucleus remains in a 7837 keV excited state, a subsequent de-excitation occurs via a cascade of on average 4-5  $\gamma$ -ray emissions [14]. The de-excitation is illustrated in Figure 2.6. The continuum component of the  $\gamma$ -ray spectrum see in Figure 2.7 is depicted in Figure 2.6 where the multi-step de-excitations of <sup>158</sup>Gd\* can occur between unresolvable levels in quasicontinuum (dashed lines), within discrete levels (solid lines). This results in a random distribution of both the number and energy of the emitted  $\gamma$ -rays.

In addition to neutron capture of Gd, hydrogen also produces a neutron capture signal. Hydrogen has thermal neutron capture cross section of 0.33 b which appears meagre in comparison with Gd, however due to the abundance of hydrogen in the LS, acrylic, and water, a significant number of neutron captures are observed. Following the capture of a thermal neutron, the excited deuterium atom decays to its ground state and emits a single 2.2 MeV  $\gamma$ -ray [4]. The prominent peak resulting from the hydrogen capture can be in the OD energy spectrum, Figure 2.7.

By doping LS with Gd, the efficiency for detecting at least one of the capture gammas is very high compared to having stand alone LS. Another advantage of Gd-doping is reduction in the time delay for neutron capture from 220 $\mu$ s to 28 $\mu$ s intern reducing the length of the window needed for vetoing by a factor of 7 [4]. Detailed simulations by the LZ Collaboration initially

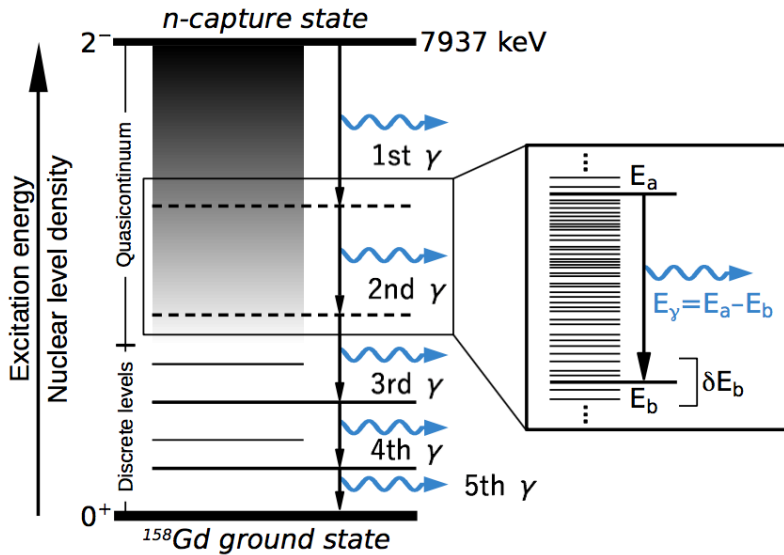


Figure 2.6: Illustration of the multi-step  $\gamma$ -ray emission of an excited  $^{158}\text{Gd}^*$  following the thermal  $^{157}\text{Gd}(n, \gamma)$  reaction. The de-excitation to the ground state can occur via many intermediate levels. Adapted from Ref.[14].

expected to use a veto window of  $125\mu\text{s}$ , however it was found that neutrons also captured in the acrylic up to 10% of the time [4]. Further studies by the author also found that neutrons captured in the water which had partially saturated foam displacer between the acrylic tanks and OCV. This effect further extended the required veto window to  $600\mu\text{s}$ . This study is discussed further in Chapter 4.

### 2.3.2 PMT system

Interactions in the GdLS and water are monitored by 120 Hamamatsu 8-inch R5912 photomultiplier tubes (PMTs) arranged as shown in Figure 2.8. This model of PMT has been used successfully prior to their use in LZ at Daya Bay whose detector design is echoed in the LZ OD design [15]. The R5912 PMTs were chosen because of the following reasons:

1. The spectral response ranges from 300 nm to 650 nm, with a peak wavelength at 420 nm. This encompasses the range of the scintillation light from the LAB mix between 390 nm to 440 nm [13]. The comparison can be made comparing the plots in Figure 2.9.
2. The quantum efficiency covers the relevant range, with an average expected value of  $\sim 25\%$  at 430 nm, as shown in Figure 2.9b.
3. The radioactivity levels of the PMTs and support structure is a fairly weak constraint due to the 84 cm of water separating them from any active volume. In the scintillator itself, the simulated event rate from the PMT radioactivity is  $< 4$  Hz [4].

Prior to the installation of the PMTs at SURF, rigorous testing to fully characterise the response of tubes was carried out by groups from Brandeis University and the IBS Center for Underground Physics. Further details of the quality assurance testing is documented in Ref.[17].

### 2.3.3 Outer Detector Optical Calibration System

LZ uses an optical calibration system to monitor: the PMT gain/single photoelectron (SPhE) size; afterpulsing rates; and the optical properties of the acrylic and scintillator. Light produced

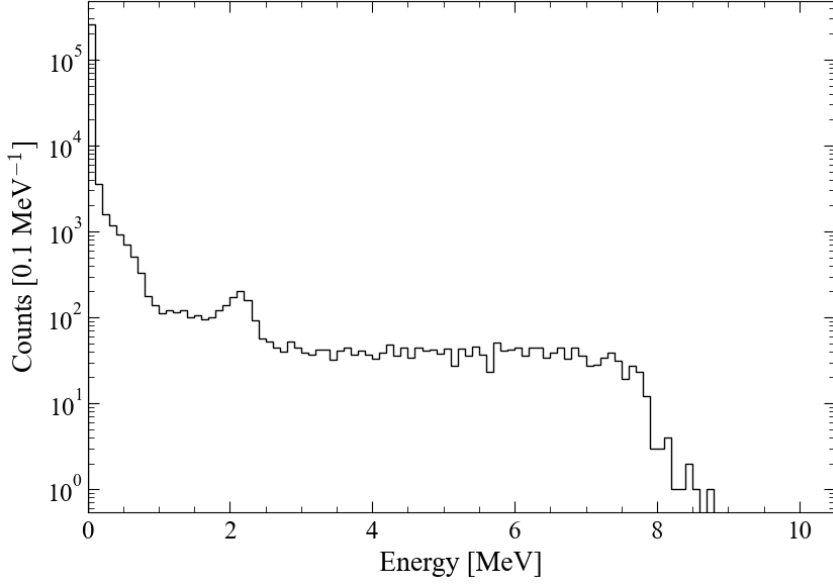


Figure 2.7: AmLi energy spectrum measured with LZ Outer Detector with coincident single scatter signals in the TPC, here simple data quality cuts have been applied. The distinctive hydrogen capture peak can be seen at 2.2 MeV, whilst the continuous  $\gamma$ -ray spectrum from the Gd Capture has the expected end point at  $\sim$ 8 MeV.

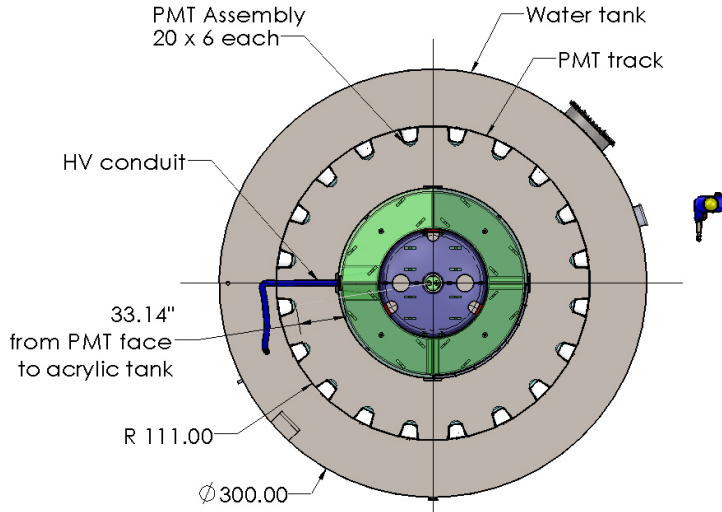
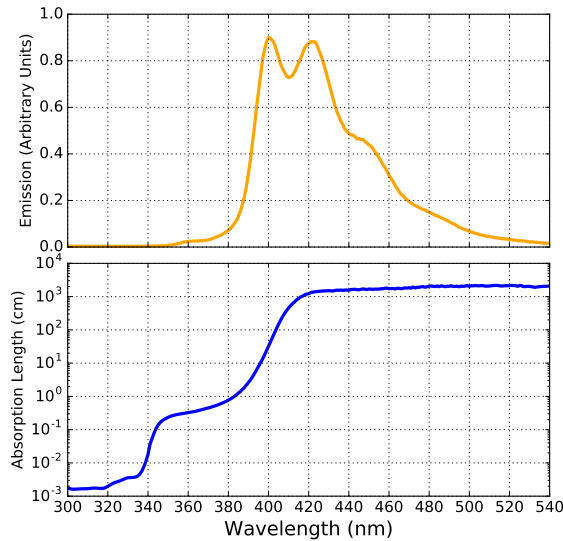
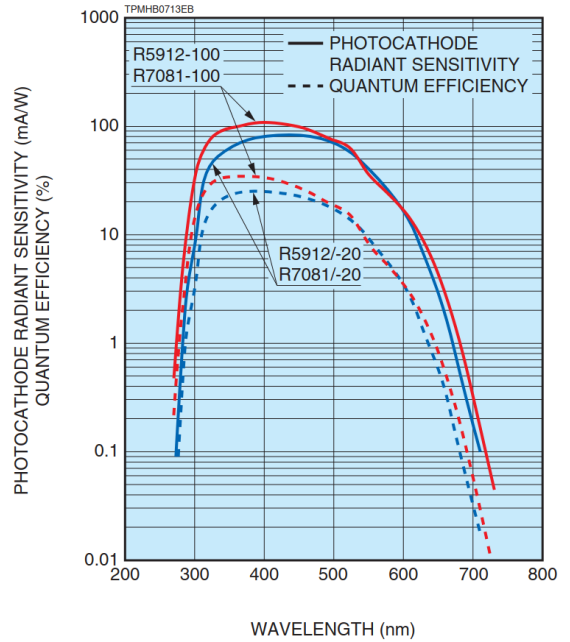


Figure 2.8: Plan view of the OD PMT support system. The 20 PMT ladders are mounted to a circular track attached to the walls of the water tank [4].

by the LED-driven system is injected into the OD at 35 different locations. Thirty injection points are evenly distributed throughout the PMT array (10 azimuthal positions at 3 heights as shown in Figure 2.10). Four of the injection points are each positioned in centre of the side acrylic tanks facing upwards to monitor the optical properties of the GdLS. One final injection point is positioned in the outer rim of a side acrylic tank also facing upwards and is used to monitoring the optical properties of the acrylic. Duplex fibres are used to inject light pulses produced by LEDs to the different locations. For the thirty injection points situated within the PMT, 435 nm LEDs are used to match the peak wavelength and quantum efficiency of OD PMTs. Only one core in the fibre is used, the additional core is a backup in the event of any damage to the first core. 435 nm and 450 nm were doing for the injection points facing into the LS to monitor optical degradation of the scintillator. Below 420 nm the absorption length of GdLS decreases significantly as shown in Figure 2.9a, if the scintillator degrades this



(a) Wavelength dependence of two optical properties of the GdLS. **Top:** Emission spectrum of scintillation light. **Bottom:** The absorption length of GdLS [13].



(b) Wave length dependence of the quantum efficiency of the Hamamatsu 8-inch R5912 photomultiplier tube. Adapted from Ref.[16]

Figure 2.9: A comparison of the wavelength dependence of key optical parameters for both the GdLS and PMTs.

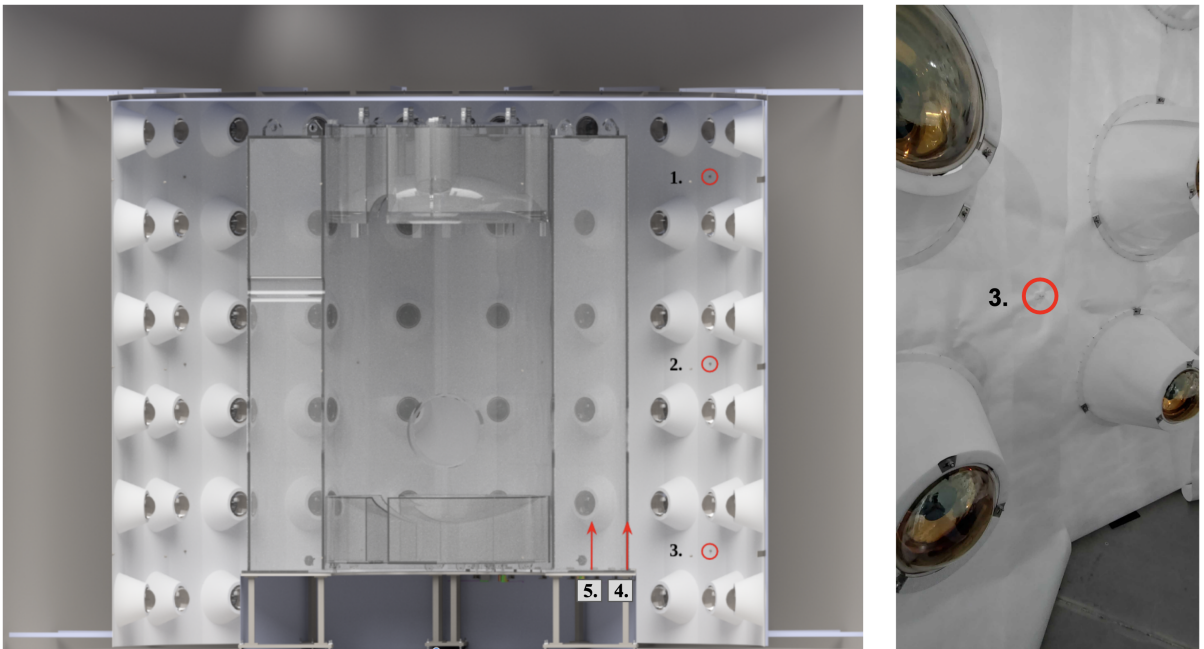


Figure 2.10: **Left:** A cross-section of a CAD drawing of the OD. The three heights of the 10 azimuthal positions of the optical fibre injection points are labelled 1-3. Two injection positions under the side acrylic tanks which point upwards are labelled 4 and 5. **Right:** A photograph of the OD PMT array showing the point of an injection point relatively to the surrounding PMTs.

region shifts to higher wavelengths. A similar approach is taken for monitoring the optical properties of the acrylic using 390 nm and 435 nm LEDs. The transmission of light through

the acrylic varies with wavelength, as shown in Figure 2.11. Monitoring the optical properties of the acrylic and scintillator during science runs is key to ensure consistent light collection during science runs. The electronics system which controls the LEDs consists of five Optical

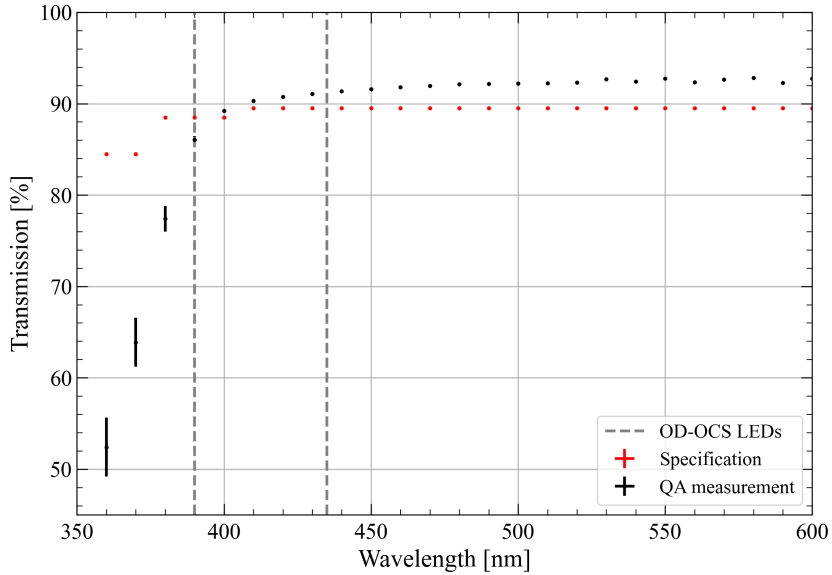


Figure 2.11: Quality assurance measurement data taken during the commissioning of the acrylic tanks. The QA measurement data is the average transmission of light at a particular wavelength across 46 points. Vertical lines indicate the 390 nm and 435 nm LEDs with respect to the transmission of light.

Calibration Cards (OCC). Each OCC consists of an FPGA controlled motherboard which houses eight LED pulser boards and two four-channel photodiode boards. Light pulses from the LEDs are divided by a three-way optical coupler: to the injection points in the OD; to the photodiode readout for onboard monitoring; to a monitoring PMT. The layout of the system can be seen in Figure 2.12. The intensity of light is monitored using the onboard photodiode and rack mounted monitoring PMT, which is the same 8-inch Hamamatsu R5912 PMT as used in the OD PMT array [18]. The stability of the light produced by the LEDs is monitored through the comparison of light produced by an in-situ YAP:Ce pulser which produces light pulses corresponding to 5000 photoelectrons [18, 20]. The intensity of light produced by both the LED and source is then compared for consistency across science runs. The commissioning of this subsystem is covered further in Chapter 3. The OCS is controlled through LZ’s central Slow Control System, allowing a user to define a pulse size/intensity using a graphical user interface [21]. During the authors Masters degree at the University of Liverpool a member of the group who developed the OCS and extensively tested the system. The OCS met all design requirements set by LZ [18]. Further details of the OCS and the QA tests prior to installation can be found at Ref.[21, 18].

## 2.4 Calibration Systems and Sources

To understand the LZ detector response and its performance, regular calibrations are performed using a variety of methods and sources. Such calibration procedures are used to characterise: the energy scale; energy threshold; micro physics of particle interactions; as well as the position and time dependence of the detector responses [19]. A summary of the sources, their purpose and their deployment methods is shown in Table 2.2. Injected sources consist of gaseous radioisotopes which are injected into the xenon circulation system and in turn into the TPC volume itself. The injection of sources directly into the TPC volume is beneficial for a few reasons. Firstly, as source is injected and allow to mix with the LXe, this allows calibration with spatial uniformity.

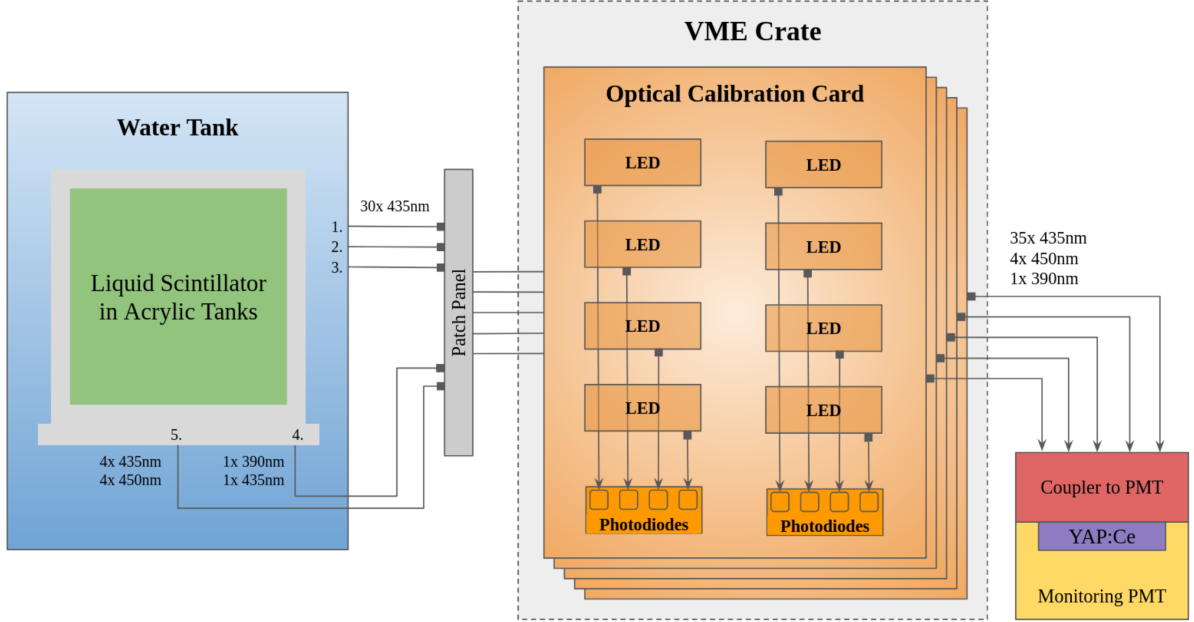


Figure 2.12: A schematic of the OD OCS. An example of one Optical Calibration Card (OCC) is shown with its eight LED pulser boards and two photodiode boards. A total of five OCCs make up the OCS and are powered by a VME crate. Lines with arrows show the paths light takes down various fibres to different positions in the system. Labels 1-3 represent the three heights within the PMT array, while Label 4-5 denote the injection points to monitor the GdLS/acrylic, as shown in Figure 2.10. Adapted from Ref.[18, 19]. **NEED TO CHANGE THE COLOURS IN THIS SCHEMATIC!**

Isotope	Interacting Particle	Energy [keV]	Purpose	Deployment
$^{83m}\text{Kr}$	$\beta, \gamma$	32.1/9.4	TPC(x,y,z)	Injected
$^{131m}\text{Xe}$	$\gamma, \text{x-ray}$	163.9	TPC(x,y,z), Skin	Injected
$^{220}\text{Rn}$	$\alpha, \beta, \gamma$	Various [22]	Skin, ER Band	Injected
$^3\text{H}$	$\beta$	0 – 18.6	ER Band	Injected
$^{14}\text{C}$	$\beta$	0 – 156.4	ER Band	Injected
$^{241}\text{AmLi}$	$(\alpha, n)$	(5638, 0 – 1500)	NR Band, Veto Efficiency	CSD
$^{241}\text{AmBe}$	$(\alpha, n)$	(5638, 0 – $11 \times 10^3$ )	NR Band, Veto Efficiency	CSD
$^{57}\text{Co}$	$\gamma$	122	Skin Energy Scale	CSD
$^{228}\text{Th}$	$\gamma$	2615	OD Energy Scale	CSD
$^{22}\text{Na}$	$\gamma$	511, 1275	Inter-detector Timing	CSD
$^{52}\text{Mn}$	$\gamma$	835	Skin Energy Scale	CSD
$^{88}\text{YBe}$	$(\gamma, n)$	(1836, 152)	NR Response	External
$^{88}\text{YMg}$	$n$	1836	NR Response	External
DD	$n$	2460	Light and Charge Yields	External
$^{241}\text{Am}$	$\alpha$	5638	ODOCS Calibration	External

Table 2.2: A list of calibration source used by LZ for TPC, Skin and OD calibrations along with the purpose and method of deployment. The energy (keV) refers to particle energies relevant for the calibration of LZ and is not a complete list of decay energies. The energies quoted in the parentheses correspond to those of the particle species from the previous column. Adapted from Ref.[19, 17].

Secondly, the LXe target is self-shielding so an external low energy source would require a

large amount of exposure time to achieve comparable statistics to the injected source. Lastly, monitoring how the injected isotopes mix within the TPC allows LZ to further understand the mixing and flow patterns of background radioisotopes [19]. The injected radioisotopes either decay away due to their short-lived nature ( $^{83m}\text{Kr}$ ,  $^{131m}\text{Xe}$  and  $^{220}\text{Rn}$ ) whereas the live-lived source, tritiated methane ( $\text{CH}_4$ , is removed by the hot zirconium getter [2].

Beyond the injected sources, there are external sources which can be separated into two subcategories by their deployment, either using the Calibration Source Deployment system or stand alone deployment method. The CSD lowers neutron and gamma rod sources in three tubes located in the vacuum space between the ICV and OCV [2]. Each tube is connected to an independent deployment system which allows sources to be precisely positioned at different depths in the detector. Depending on the depth of deployment, the radioactive source can generate signals in various regions of the OD, TPC, and Skin. The use of various sources at various heights allows for calibration of the detectors' energy scale and the spatial dependence of the energy scale. Inter-detector timing measurements between the three detectors is also carried out using the CSD sources. Understanding time offsets between the detectors is crucial for functioning veto system which is dependent on time based section to remove background events.

Beside the CSD sources, a deuterium-deuterium (DD) neutron generator is used to produce neutrons for TPC calibrations and to cross check Veto tagging efficiency (discussed in Chapter 4). The generator produces 2.45 MeV neutrons which are directed through calibration conduits that pass through the OD acrylic tanks to the OCV. A detailed description of neutron generation and the system is provided in Ref.[19]. To understand low energy detection efficiency of the TPC  $^{88}\text{YBe}$  and  $^{88}\text{YMg}$  photo-neutron sources are used. Both sources are deployed externally through a removing a small acrylic vessel in the OD and replacing it with source assembly. This small vessel is shown in green above the blue top tanks in Figure 2.5. The final source listed in Table 2.2 is sealed  $^{241}\text{Am}$  within a YAP:Ce crystal and is used within the ODOCS, as described in subsection 2.3.3.

## 2.5 Data Acquisition System

Signals produced in the PMTs across the experiment are processed by the data acquisition system. LZ employs a custom FPGA-based Architecture for Data Acquisition and Real time monitoring (FADR) to perform the digitisation and identify events of interest for offline analysis [23, 24]. Signals first pass through shaping amplifiers which increases signal-noise ratio. At the amplifier stage, the signals from the TPC and OD are split into dual gain outputs to maximize the available dynamic range and extend the range of energies than can be probed by the experiment. The Skin detector has only a single gain output. Following amplification, the analogue signals are digitized with a sample rate of 100 MHz (10 ns samples) using custom built 32-channel digital signal processing boards [24]. Due to the sheer volume of data that comes from the PMTs Pulse Only Digitisation (POD) methods are employed to reduce the raw waveform volume by a factor of 50 [4]. The threshold used in this filter is tuned on SPhE data and is set to provide a detection efficiency of  $> 99\%$  [23]. Results from the POD waveform analysis are passed to the data sparsifiers and grouped by the Data Sparsifier Master (DSM) where a decision is made whether an event has been observed. The DSM informs the DAQ Master and time window is selected for the event and the data is extracted from the digitizers and stored by one of the Data Collectors. A simplified schematic of the LZ DAQ system is shown in 2.13, depicting one channel of digital electronics. Event builders take the data which has been temporarily stored on the Data Collectors, organized the data by channel, and assembles full event structures for offline analysis. **Should I include something on the triggers? FADR Paper P15 [23]** An in-depth description of FADR can be found at Ref. [23].

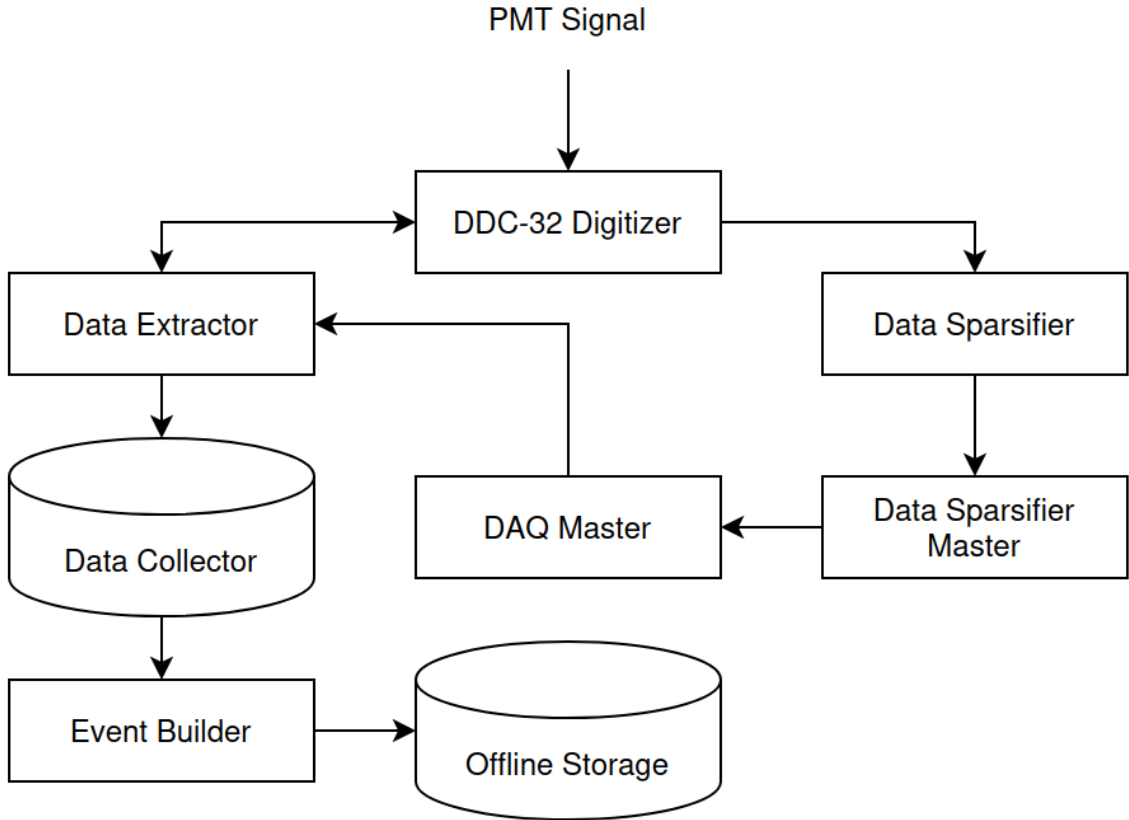


Figure 2.13: A simplified schematic depicting how PMT signals are processed using the LZ DAQ system. Adapted from Ref.[23].

## 2.6 Simulation Techniques

Simulations of the LZ experiment play a key role understanding the detector and its response. They present several purposes, for example: the calculation of background rates in LZ; the prediction of sensitivity of the experiment to rare event searches through Profile Likelihood Ratio analysis (PLR); the testing of event reconstruction infrastructure; determining efficiencies of data selection methods. An overview of the LZ simulation framework is shown in Figure 2.14. For all simulations, LZ uses BACCARAT<sup>1</sup>[25] package to simulate particle interactions in the detector and this package is built upon the GEANT4 simulation toolkit [26]. Using GEANT4 along with CAD-Drawing, the LZ experiment is built as a detector geometry. In simulation, a series of inputs can be used to generate particles which are propagated through the detector geometry, with any additional particles being generated from interactions with detector materials. GEANT4 is used to track the particles and identifies the interaction points. From there, two separate chains exist for interpreting this information, Figure 2.14.

The “Fast” chain, seen on the right of Figure 2.14, records energy deposits in the detector and passes them to LZLAMA for processing. LZLAMA consists of two primary packages, the Noble Element Simulation Technique (NEST) to process interactions in the xenon space and DICEBOX to process interactions with the OD. NEST provides the expected conversion of energy to scintillation photons and ionization electrons based on empirical models developed using experiment measurements [27]. The DICEBOX toolkit is employed to handle interactions between neutrons and their capture on Gd as GEANT4 has difficulty conserving Q-value and multiplicity of the gamma emissions from the neutron capture. Energy deposits in other volumes are handled by GEANT4. LZLAMA outputs a ROOT file which has the same reduced-quantity

<sup>1</sup>Basically A Component-Centric Analogue Response to AnyThing

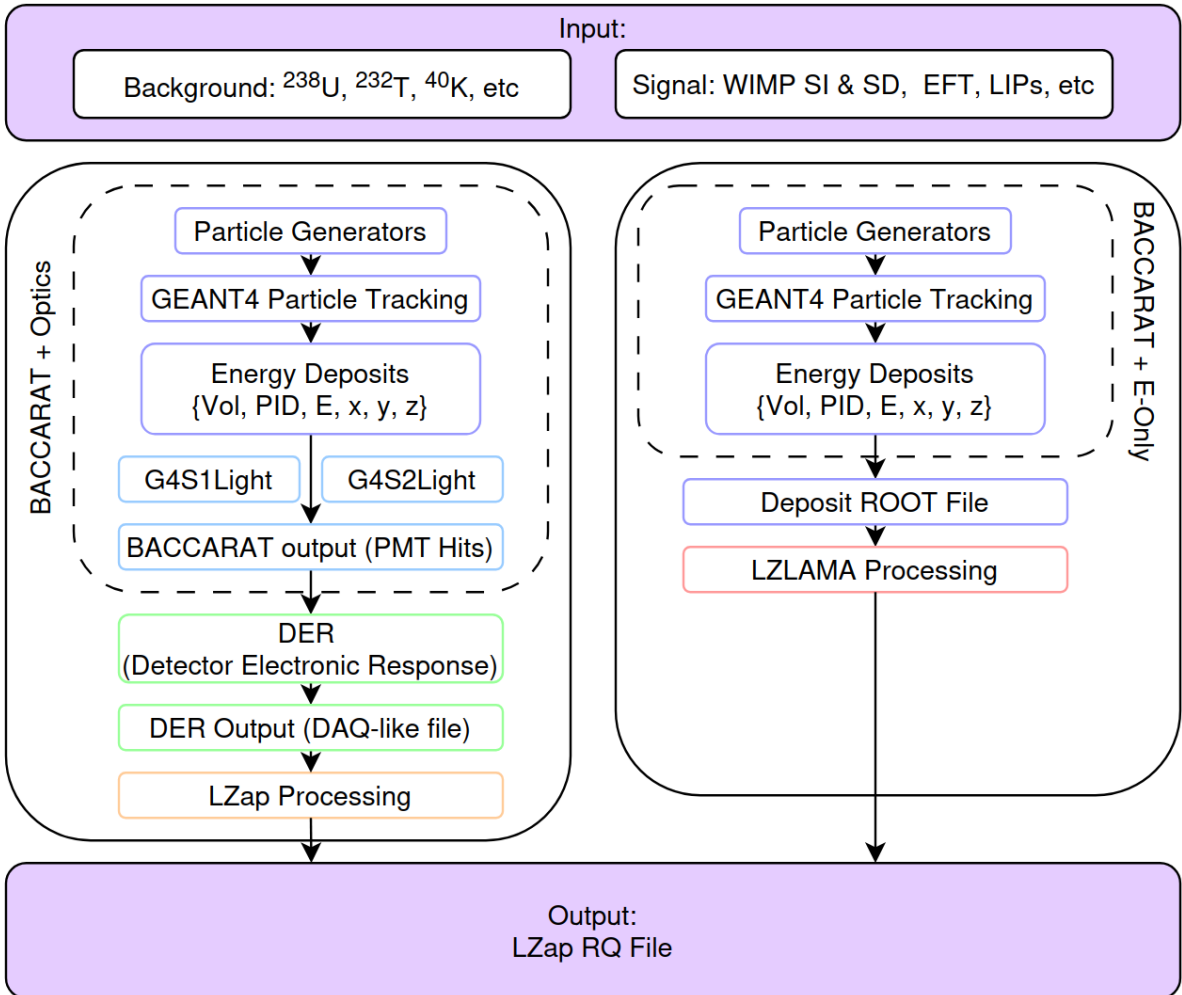
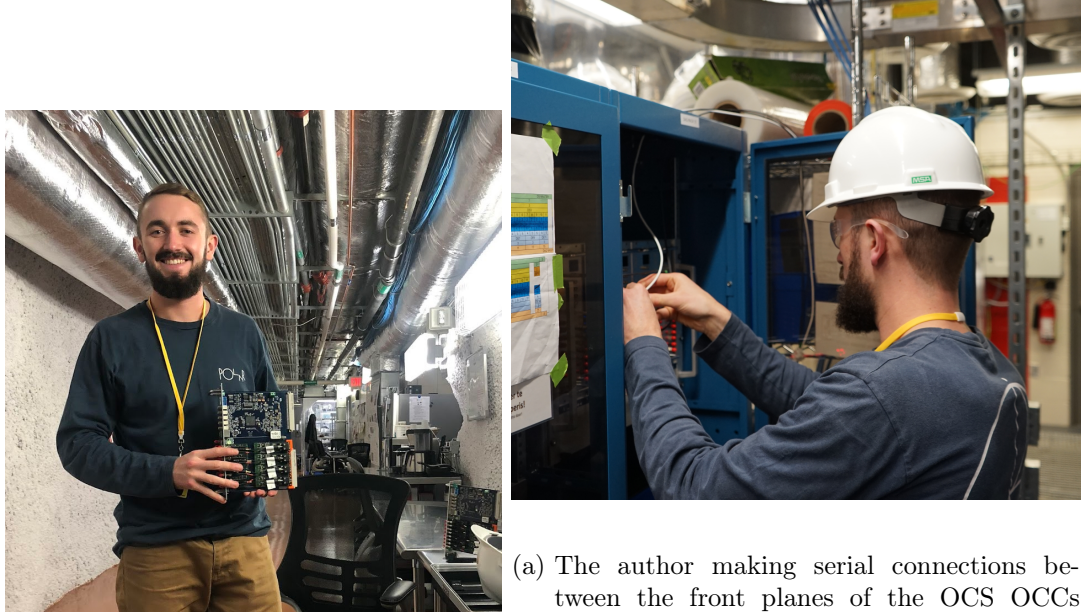


Figure 2.14: Simulation framework for the LZ experiment. “Full” and “Fast” simulation chains are shown. Both chains begin with BACCARAT and end with an output LZap RQ file.

(RQ) format as data processed using LZ’s custom processing tool, LZap [25], which performs pulse and event reconstruction.

The second, “Full” chain, enables full simulation of optical processes throughout the entire detector including VUV photons and ionisation electrons that are produced in the xenon and scintillation light generated in the OD. Another custom LZ software package, Detector Electronic Response (DER), is used to translate PMT hits in the BACCARAT output into waveforms. The DER simulates the analogue front-end electronics of LZ to produce waveforms, written in an identical format to the true LZ DAQ, Section 2.5. A number of physical processes are incorporated into the DER to create realistic waveforms including: a PMT response model, gain, quantum efficiency, double photoelectron probability, dynode effects, dark rate, and afterpulsing. This chain is more computationally intensive but it allows for a more realistic, event-by-event analysis. The output from the DER is processed by LZap to produce RQ-structured files to be analysed much like real data. A complete review of the LZ Simulation framework can be found at Ref.[25].



(a) The author making serial connections between the front planes of the OCS OCCs within the electronics racks.

Figure 2.15

## 2.7 Assembly and Operation of the LZ Detector

During the past six years whilst the author has collaborated on the LZ Experiment, a significant portion of that time has been spent on-site at SURF working on the assembly, commissioning and operation of the LZ Detector. These efforts began with the installation of the OCS electronics and an in-situ-calibration of the LED system, this work is detailed extensively in Ref.[21].

# 3 Outer Detector Commissioning and Monitoring

## 3.1 OD PMT Calibration

As discussed in 2.3, the primary purpose for the LZ Outer Detector is to detect neutron interactions which have coincident signals within the TPC. The source of most of the neutron background is from the ( $\alpha$ , n) process in material surrounding the edges of the xenon. A neutron will enter the TPC and then scatter out. The neutron can traverse the intervening material and then thermalize and capture on either the Gadolinium or the Hydrogen in the scintillator mixture or recoil off the protons in the scintillator. When the neutron recoils off the proton, energy depositions of  $\sim 100$  keV are produced [2]. The pulses of light detected in the PMTs for such low energy interactions are  $\sim 15$  photons in size and require the PMTs to be calibrated to a single photon sensitivity. Understanding the response of the PMTs is key to measuring single photon sensitivity and in turn reconstructing the gain of the PMTs. A model of photomultiplier response is presented in Ref.[28] which will be described below.

### 3.1.1 Single Photo-electron Response Model

The PMT is considered to be an instrument which consists of two independent parts:

- A photo-cathode where photons are converted into electrons
- An amplified which amplifies the initial charge (dynode system)

The model assumes that the number of photons incident on the PMT and subsequently the photo-cathode is a Poisson distributed variable. Only a fraction of the photons are converted to photo-electrons, this is the quantum efficiency of the PMT and is a random binary process ( $\sim 25\%$  for the OD PMTs). The photo-electrons are then guided towards the first dynode by an electric field in which  $\mathcal{O}(100\%)$  photo-electrons complete this process. The convolution of the Poisson and binary process results in a Poisson distribution:

$$P(n; \mu) = \frac{\mu^n e^{-\mu}}{n!}, \quad (3.1)$$

where  $\mu$  is the mean number of photo-electrons collected at first dynode,  $P(n; \mu)$  is the probability that  $n$  photo-electrons are observed for a mean  $\mu$ . The photo-electron is then amplified by the dynode system, which for the OD PMTs is a series of 10 dynodes. The amplification of the dynode system is determined by the voltage distribution across the dynode and it is tuned on a PMT-by-PMT basis to achieve a gain of  $\mathcal{O}(10^6)$ . The cascade of photo-electrons produced from the amplification is collected at the anode of the PMT and a voltage is measured as a pulse. The area of the pulse corresponds to number of electrons incident on the anode and is Gaussian distribution:

$$G_n(x) = \frac{1}{\sigma_1 \sqrt{2n\pi}} \exp\left(-\frac{(x - nQ_1)^2}{2n\sigma_1^2}\right), \quad (3.2)$$

where  $x$  is the variable charge,  $Q_1$  is the mean value of the charge outputted from the amplification at the dynode,  $\sigma_1$  is the standard deviation of the charge amplification. The ideal response of an ideal PMT,  $S_{ideal}$ , can be described simply by convoluting Equation 3.1 and Equation 3.2

together:

$$\begin{aligned} S_{ideal}(x) &= P(n; \mu) \otimes G_n(x) \\ &= \sum_{n=0}^{\infty} \frac{\mu^n e^{-\mu}}{n!} \frac{1}{\sigma_1 \sqrt{2n\pi}} \exp\left(-\frac{(x - nQ_1)^2}{2n\sigma_1^2}\right), \end{aligned} \quad (3.3)$$

the model is summed from 0 photons to an arbitrary upper limit [28].

### 3.1.2 Single Photo-electron Calibration

To calibrate the OD Single Photo-electron (SPhE) response, light is injected into the OD using the ODOCS. The optimal intensity of light to induce a SPhE response was chosen during the commissioning of the OD following the PMT installation in 2021. Details of the optimisation can be found in Ref.[29].

Due to the complex geometry of the OD, the central row fibres were chosen as the injection points, position 2 in Figure 2.10 (central row). Light injected from the central row fibres pass through the SATs and reflects back off of the Tyvek® layer which covers the OCV. Light injected from position 1 has the ability to pass direct through the TATs. Light injected from position 3 would be reflected within the BATs due to Tyvek® layers which was placed between the three acrylic tanks to cover foam which was needed to displace water. This later design decision was to increase light collection. Irregular gaps between BATs are present due to differences in moulding during construction of the BATs.

The OCS is configured so that 1000 photons are emitted from the end of the fibre. Due to attenuation of light in the fibre, 2000 photons must be emitted by the LEDs to account for a factor of two attenuation. For each injection of light, one of the 10 central row fibre emits 200,000 pulses at a 700 Hz injection rate. The rate of pulses injected was determined to not overload the LZ DAQ.

For ease of repeated measurement, an analysis module for the OD SPhE was developed to be used in conjunction with the LZ Physics REadiness Monitor (PREM) [4]. The analysis module contains a selection to identify the OCS pulse and differentiate it from the background light seen in the OD. It can be seen in Figure 3.1 that the OCS pulses are distributed around a peak at 560 ns after the trigger (which corresponds to 0 ns in Figure 3.1). A selection of pulses with occurred between 500 ns and 700 ns after the DAQ was triggered by the OCS was chosen as an appropriate set of bounds for the timing selection to identify the OCS pulse. A PMT Coincidence requirement was also imposed to improve the purity of the selection as pulses with a coincidence greater than 1 PMT would likely not include any afterpulses which could mimic an OCS pulse.

To measure the OD PMT's SPhE response Equation 3.3 was used to fit the channel pulse area distributions. A two-stage fitting procedure was employed to account for the monthly variation in SPhE size across all 120 OD PMTs. The first stage of the procedure, only the single SPhE peak is fitted. Initially during commissioning, the starting value for  $-\mu$  was determined by estimating the proportion of events in which no photon would be measured by the PMT. The mean and standard deviation (StD) of the histogram was used as starting values for components of the initial fit. The normalisation was taken to be the area beneath the curve between mean/4 and  $6 \times$ mean. The range in which to apply the fit was determined using the peak and defined from mean  $\pm$  (StD/mean). In the second stage of the fitting procedure, the parameters from the initial fit were used as starting parameters to a fit of the multiple SPhE distribution. The range in which to apply the second stage fit was from mean - StD to mean + 3 StD. For each run only one fibre is used to inject light resulting in a small percentage of bad fits across the 120 PMTs depending on the particular fibre being used relative to the PMT of interest. To filter out such bad fits, only fits with  $\chi^2/\text{ndf} < 3$  were recorded for further analysis.

An example histogram and fit can be seen in Figure 3.2. It can be seen that the OD PMTs

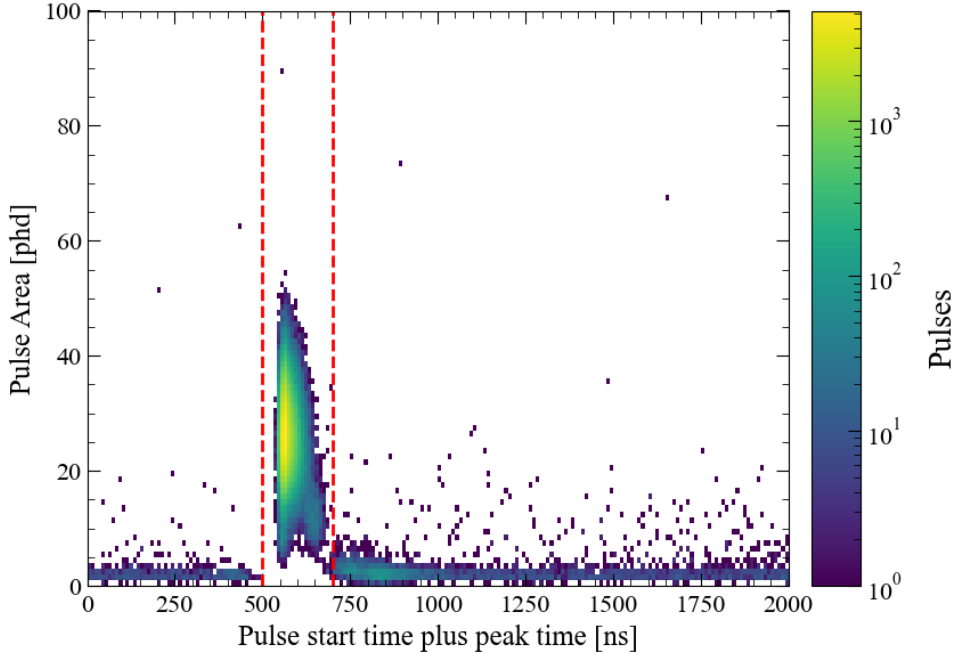


Figure 3.1: The response of the OD PMTs to 200k injections of 2000 photons during a monthly SPhE measurement. The pulse area is plotted against the start time of the pulse relative to the trigger plus the peak time relative to the start of the pulse. The OCS pulses are distributed around a peak of 560 ns. The two vertical dashed red lines indicate the inclusive timing selection criteria.

exhibit the expected response to SPhE as discussed in subsection 3.1.1

An example PMT calibration is outlined below for PMT 800. The mean Gaussian response is  $(0.9919 \pm 0.0043)$  phd and  $(14.99 \pm 0.06)$  pC. The SPhE calibration constant used to process the raw data is reconstructed by dividing the SPhE response measured in mVns by the SPhE response measured in phd, which in this case for PMT 800 is 753.9 mVns. These three values together are stored in the PREM database. In a secondary analysis stage, the measured SPhE area and calibration constant are combined to get the correct SPhE constant in mVns which in this example is 748.5 mVns. The average is taken of the corrected SPhE constant for all 10 measurements corresponding to the 10 central row OCS fibre injections. The new SPhE constant is then transferred to the LZ Conditions database along with the data and time period for which this constant is valid for. As LZ then continues to collect data, the raw pulse area measured in mVns is converted to phd by dividing the raw area by the constant. Examples of the variation in measured SPhE in both phd and mVns across all 120 PMTs is shown in Figure 3.3 and Figure 3.4.

## 3.2 Reconstructed Gain

So far it has been shown that understanding how the signal from a PMT relates to the amount of light incident on the face of the PMT is key to measuring the energy deposited by particles traversing the detector. The amplification of the photoelectrons produced through the dynode series is known as the PMT’s ‘Gain’. The SPhE Calibration Constant can be converted to understand the gain of the PMT by dividing by the following terms,  $e \times 44 \times 50 \times 10^{12}$ , where  $e$  is the charge of an electron,  $44 V_d$  is the total voltage division factor across all 10 dynodes in the PMT [16],  $50 \Omega$  is the termination impedance to eliminate signal reflections in the cable [23],  $10^{12}$  accounts for the change with the unit prefixes on voltage and time. Using the example case from the previous section, PMT 800 had an average measured SPhE area of 748.5 mVns

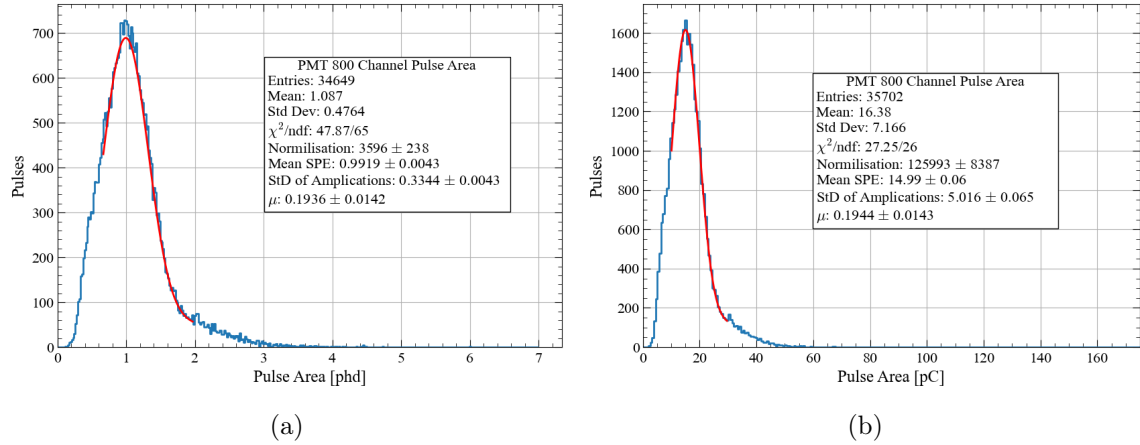


Figure 3.2: Pulse area distributions of PMT 800 from 200k OCS injections of 2000 photons during OD SPhE measurement. **Left:** Reconstructed pulse area measured in photons detected. **Right:** Pulse area taken from the area measured in the raw waveform in mVns, and converted to pC by dividing by the  $50\ \Omega$  termination at the amplifier. The fit applied in red is Equation 3.3 and the constants can be seen in the respective statistics boxes on each plot.

based on 10 OCS measurements on February 12<sup>th</sup> 2025 which results in a reconstructed gain of  $2.12 \times 10^6$ .

During the commissioning of the Outer Detector PMT system, a target gain of  $1 \times 10^7$  initially established based on the operating gain recommended by Hamamatsu Photonics [4, 16]. During the OD PMT QA the gain was reduced to  $2 \times 10^6$  due to high rates of sub-SPhE noise. Dark rates measurements made during the QA stage exhibited significantly higher rates than the expected 1 kHz dark rate measured in off-site testing. This issue was problematic as spikes up 20 kHz were observed in some cases resulting in the LZ DAQ to crash. Final voltages corresponding to  $2.1 \times 10^6$  were determined in October 2021 so that all PMTs achieved the target gain of  $2 \times 10^6$  with < 10 % difference across 119 PMTs. One exception was PMT 811, whose voltage was further reduced in January 2022 resulting in a gain of  $1 \times 10^6$  to reduce the rate of sub-SPhE pulses. An example scatter plot of gain versus PMT ID is shown in Figure 3.5

### 3.2.1 Monitoring PMT Response Over Time

Whilst operating the PMTs it is important to monitoring their response as the SPhE Area size and gain can drift over time [30, 31]. Using the data collected during the monthly OD SPhE measurements, the distribution of gain and SPhE size was tracked throughout the WS2022 and WS2024 science runs (until the time of writing) with gain versus PMT ID scatter plots as shown in Figure 3.6 and Figure 3.7. To monitor the observed < 1% change in gain month-by-month, the relative change with respect to the start of each science run was measured. During the WS2022 science run, a mean relative change of PMT gain was measured to  $(0.81 \pm 0.47)\%$ . At the time of writing, a mean relative change of PMT gain of  $(1.37 \pm 0.25)\%$  was measured for the WS2024 science run. Whilst the average gain change across all PMTs is relatively small, it can be seen in Figure 3.7 that individual PMTs drift at different rates. Due to the short run length of WS2022 it was not necessary to adjust the PMTs voltages to gain match across the PMT array during the science run, however there was a gain matching campaign in May 2022 following the science run. Prior to the start of the WS2024 science run, the OD PMTs were gain matched again to  $2.1 \times 10^6$ . After 15 months of operation it was necessary to perform another gain match of the OD PMTs as PMT 859 had a relative change in gain > 10% with other PMTs also approaching the 10% limit set by LZ.

**3.2.2 Gain Curves**

**3.3 Trigger Efficiency**

**3.4 Optical Calibration System Development**

**3.4.1 UV LED commissioning**

**3.4.2 Monitoring PMT**

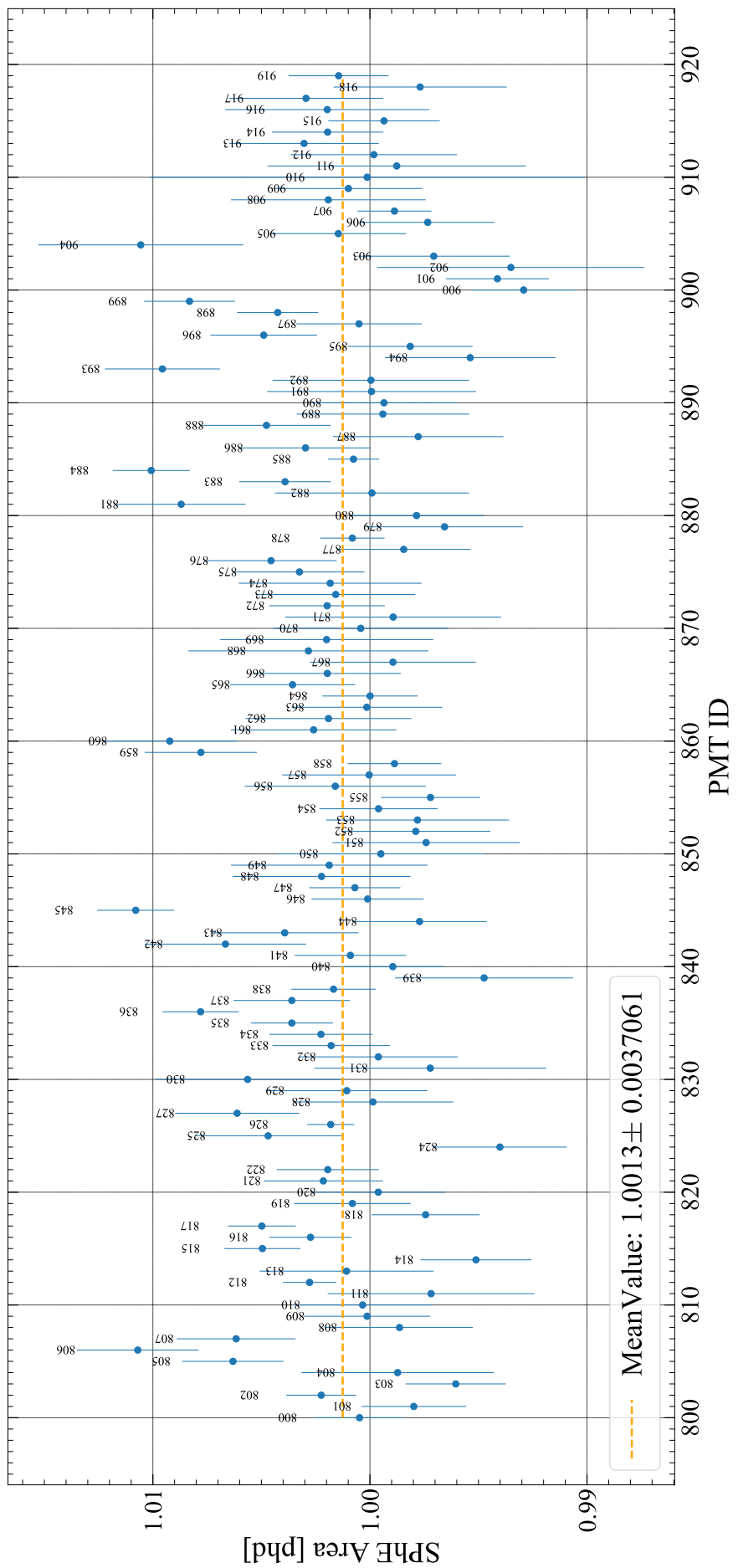


Figure 3.3: A scatter plot of the OD SPhE Area size measured in phd versus PMT ID for each OD PMT from a measurement taken on July 10th 2024.

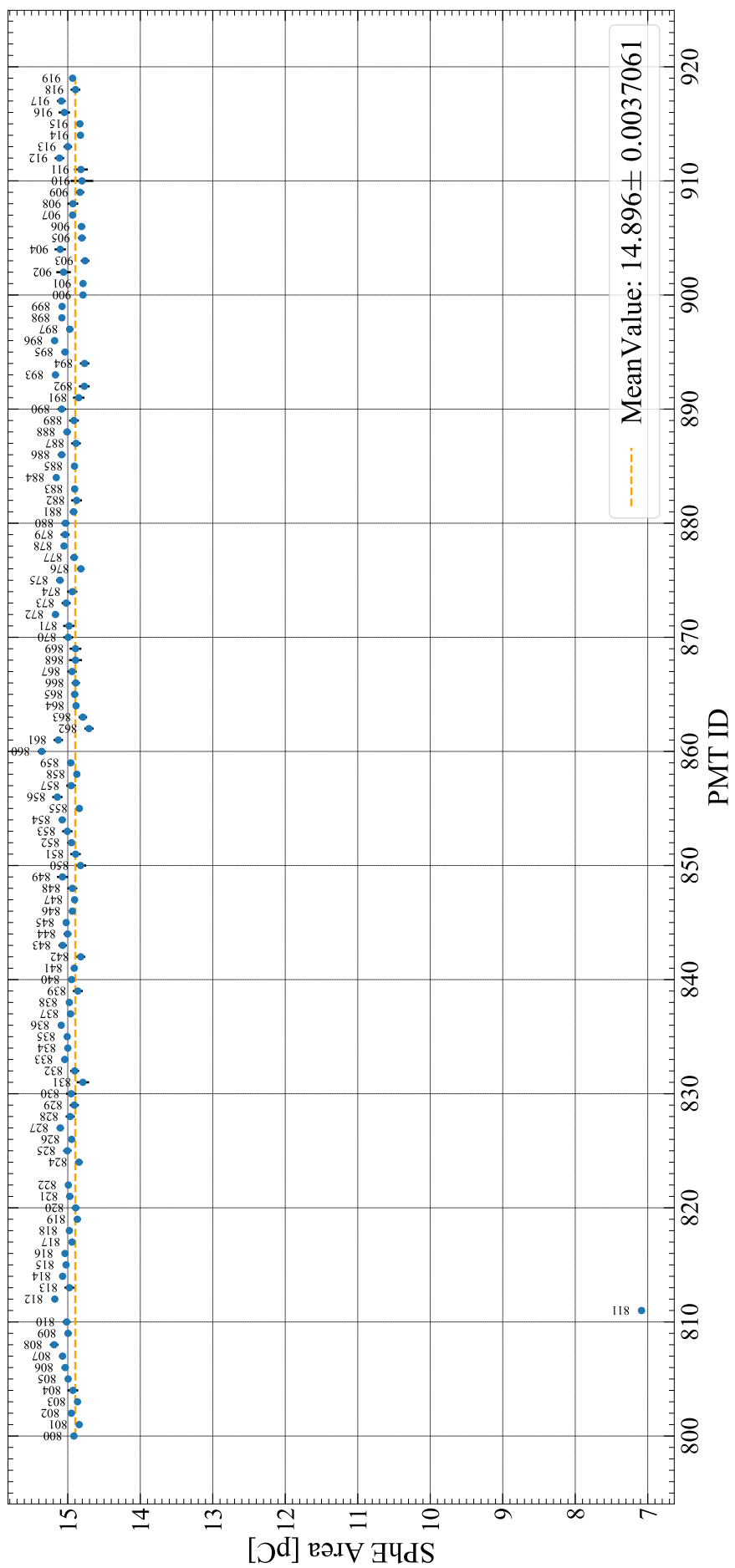
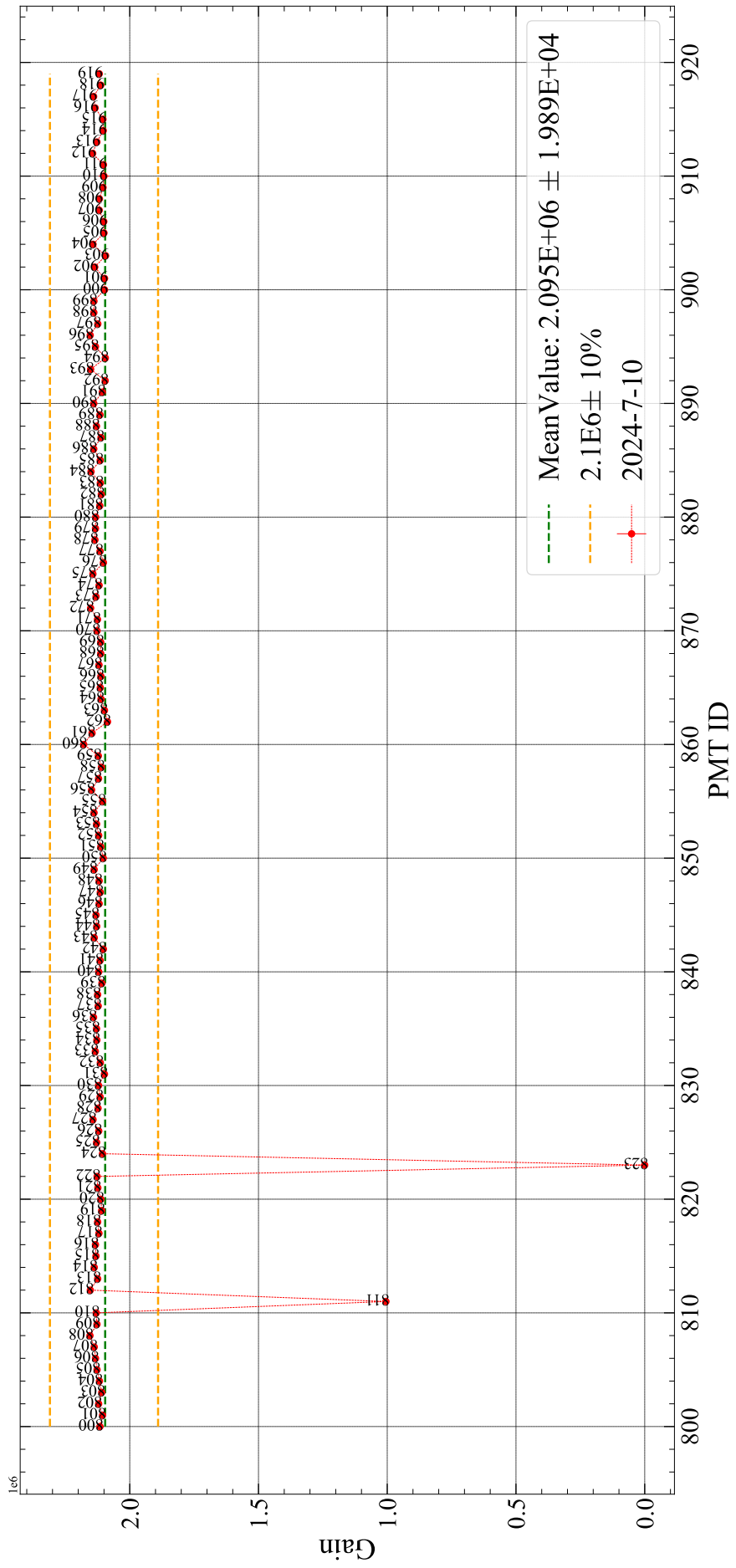


Figure 3.4: A scatter plot of the OD SPheE Area size measured in mVns versus PMT ID for each OD PMT from a measurement taken on July 10th 2024.



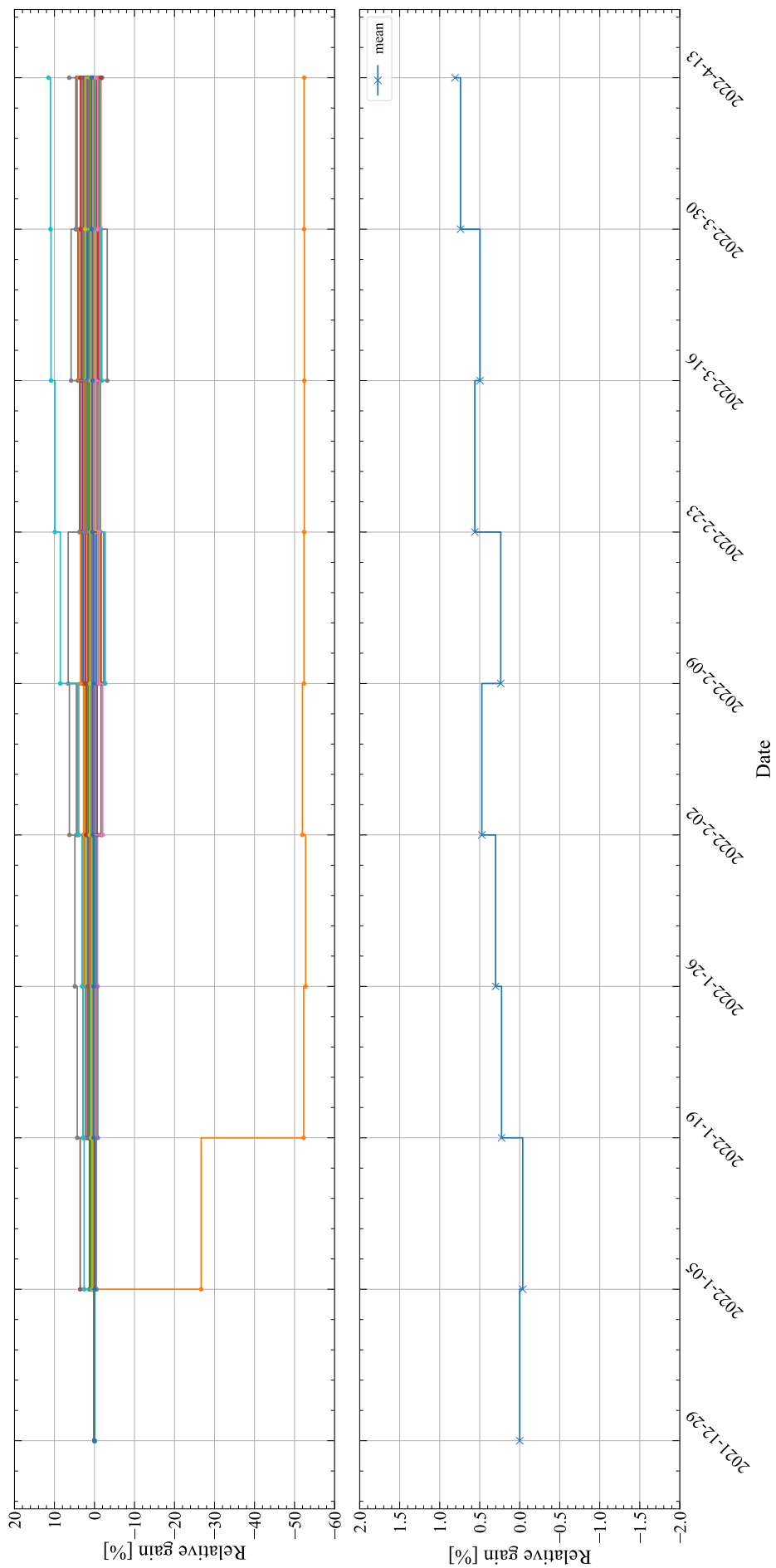
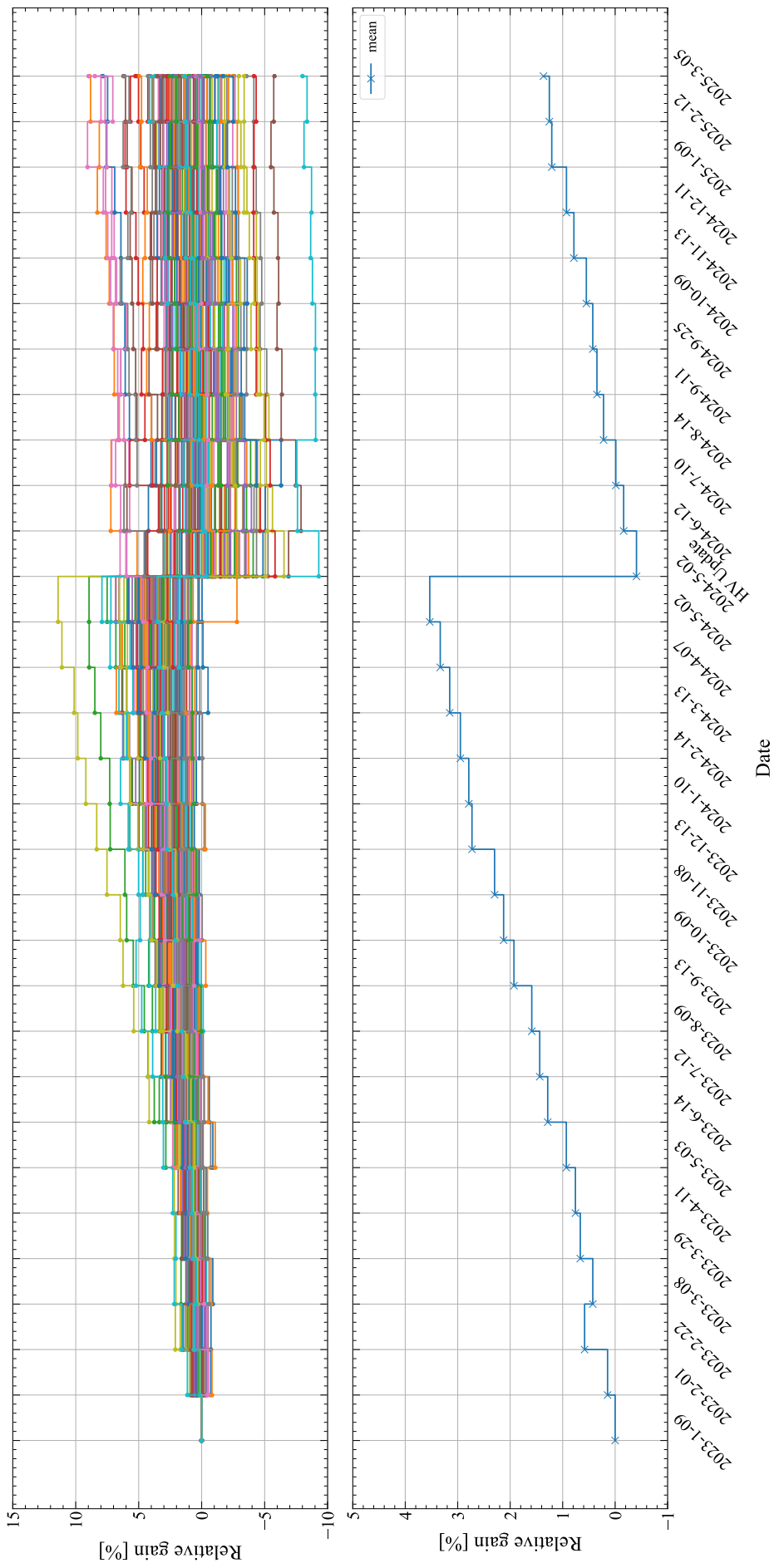


Figure 3.6: **Top:** A scatter plot of the relative change in OD PMT Gain over WS2022 science run. The reduced gain of PMT 811 can be seen in orange. **Bottom:** A scatter plot of the average relative change in OD PMT Gain across all OD PMTs over WS2022 science run.



**Figure 3.7: Top:** A scatter plot of the relative change in OD PMT Gain since the start of the WS2024 science run (until the time of writing).  
**Bottom:** A scatter plot of the average relative change in OD PMT Gain across all OD PMTs since the start of the WS2024 science run (until the time of writing).

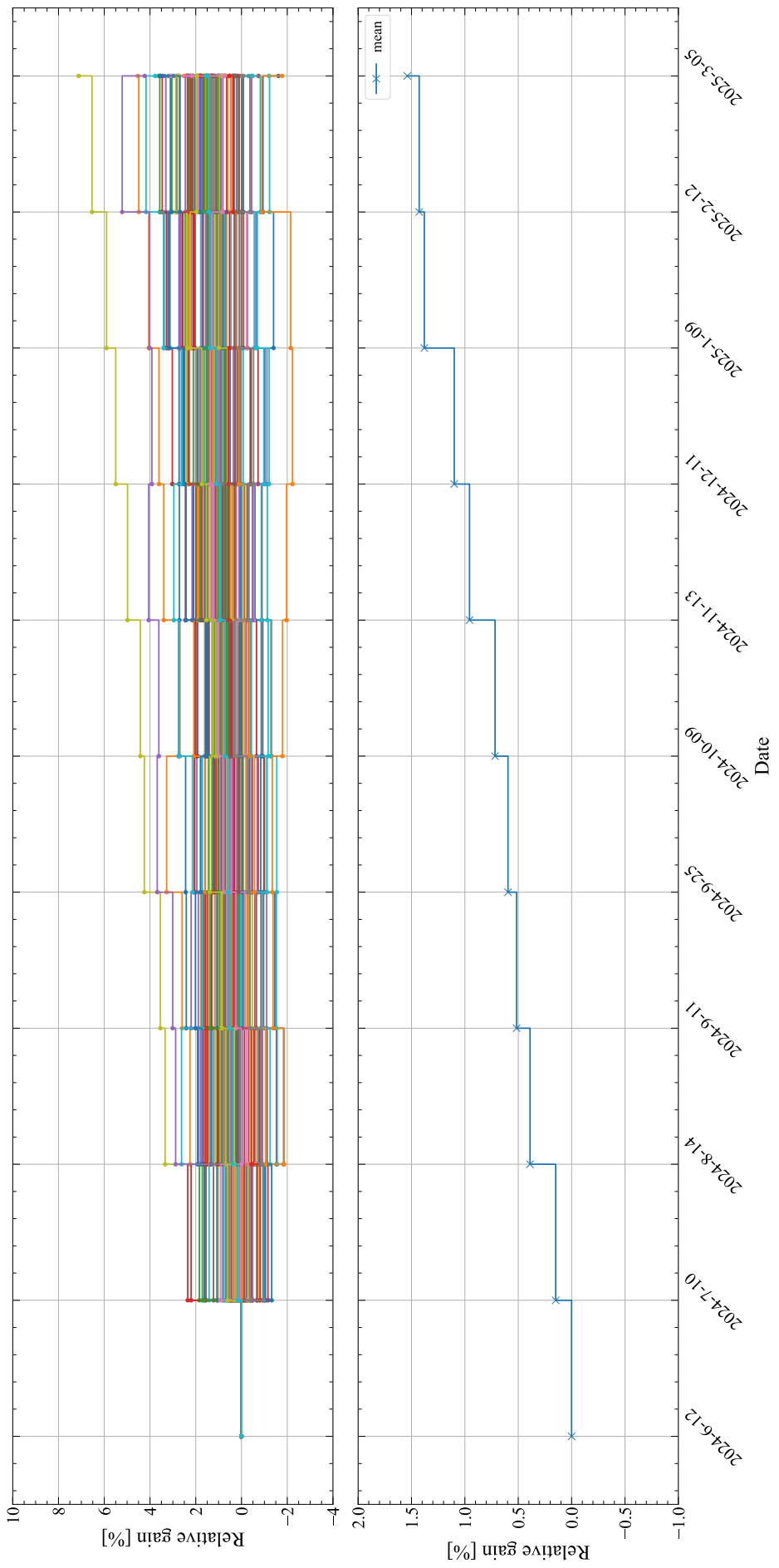


Figure 3.8: **Top:** A scatter plot of the relative change in OD PMT Gain since the gain matching campaign in May 2024 (until the time of writing).  
**Bottom:** A scatter plot of the average relative change in OD PMT Gain across all OD PMTs since the gain matching campaign in May 2024 (until the time of writing).

# 4 Veto Efficiency Studies

A WIMP scatter should only deposit a small amount of energy (few keV) within the LXe volume of the experiment without any simultaneous energy deposit in the surrounding materials. Neutrons produced through radioactive decays within detector materials would mimic a WIMP interaction when they scatter off Xe atoms.

## 4.1 Simulation Matching

### 4.1.1 Tuning OD

#### Geometry Edits

Prior to WS2024 result, there were a number of major differences between simulations and data in the Outer Detector. As such, an effort was made to correct this. The changes made were;

1. A gap was added between the acrylic tanks to account for the gap seen during installation.
2. Water was added to the foam volume which is between the OCV and acrylic tanks; each
3. The acrylic tanks were moved further away from the OCV; this matches what adding the gaps was supposed to solve.

The percentage of water in the foam, and the outward movement of the acrylic tanks were looped over. The water percentage of the foam was increased in 1% steps, and the acrylic tanks were moved by 10mm steps. The 'best' value was found to be 30mm and 6%. Additional details on the discrepancies between simulations and data are shown in the subsequent subsections.

#### Capture Time

Following the geometry changes discussed above, the neutron capture timing using AmLi was studied. Prior to the geometry changes, there was a distinct discrepancy between data and simulation when considering neutron capture timing following single scatters within the TPC. Initial skims of both data and simulation were made using ALPACA, selecting all events which were classified as single scatters by LZAP. OD pulse information was also skimmed considering 100 keV (24 phd), 200 keV (49 phd) and 1 MeV (251 phd) OD thresholds. The simulation was modified in two different ways, moving the SATs out radially and adding water to the foam. All possible configurations were visually examined to determine which variation of simulation matched the data. An example of the comparison plot can be seen in Figure 4.2, the "baseline simulation" was the initially configuration of the geometry prior to this study. All plots were examined side by side in a large scale canvas configuration seen in Figure 4.3. It was found that from this study that 30 mm to 50 mm movement of the SATs alongside 5% to 7% increase in the percentage of water in the foam provides the best agreement between data and simulation at a 200 keV threshold.

## 4.2 Veto Selection Optimisation

In this section, details on how the Skin and OD cuts used in SR3 were created are defined. The Skin and OD veto cuts used in SR3 were based on those developed for SR1, described in [32]. This boils down to four cuts;

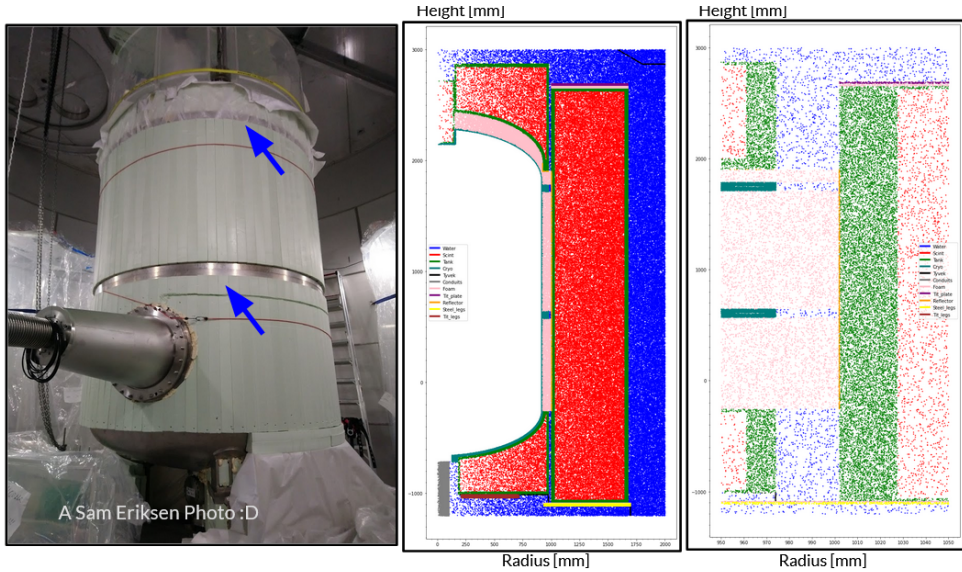


Figure 4.1: Geometry in the simulation used for SR3.

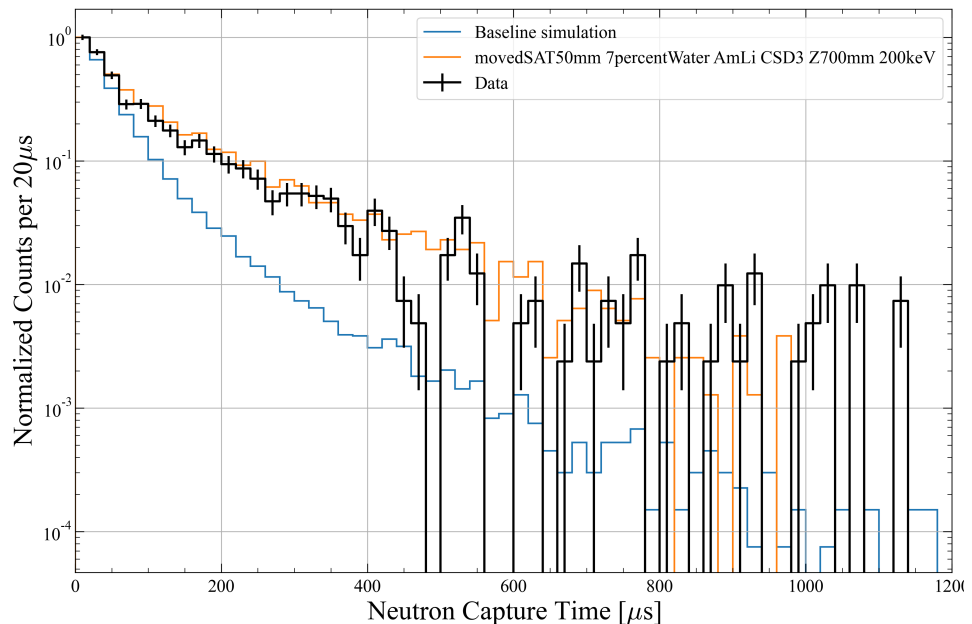


Figure 4.2: An example of the plot used to compare neutron capture timing in data with the baseline simulation and the modified simulation.



Figure 4.3: Large scale canvas of all possible simulation configurations. Each plot is similar in style to Figure 4.2. Here AmLi at 700mm in CSD3 has been shown as an example.

- Skin-prompt: For tagging  $\gamma$ -rays in the Skin detector,
- OD-prompt: For tagging  $\gamma$ -rays and neutron proton recoils in the OD detector,
- Skin-delayed: For tagging  $\gamma$ -rays from post-neutron capture de-excitation,
- OD-delayed: For tagging  $\gamma$ -rays from post-neutron capture de-excitation.

Using SR1 (and pre-SR2) as a baseline, three studies were performed to adapt these cuts for SR3;

1. Determine the detector stability, to establish if the energy scale for the detectors has changed; using this the SR1 cuts can simply be scaled for SR3, and acts as a starting point.
2. Implement a position correction to the OD.
3. Perform cut optimisation based on the above studies.

The cuts used for the vetoes were selected at the same time as AmLi neutron tagging efficiency calculation, and were set to maximise the tagging efficiency whilst reducing deadtime<sup>1</sup>. As such, this section should be considered simultaneously with subsection 4.3.2

On a skim of the AmLi calibrations which pass the SR3 core-cuts described in Table 4.1, the efficiency (described in Equation 4.2) was calculated with the pulse area, and coincidence thresholds of the Skin and OD varying in integer steps. This then produces a heatmap of the coincidence vs. threshold vs. efficiency of each cut, examples of these are shown in Figure 4.5-4.8. For the delayed cuts, the veto time window was also varied, and heatmaps of threshold vs. time window vs. efficiency were produced for a fixed coincidence. Heatmaps with dead time rather than efficiency were also produced. The dead time is discussed in greater detail in the next section.

The windows for the prompt cuts were selected by looking at the DD and AmLi calibrations (the run numbers and the LZAP version are listed in Section 4.3) and by measuring the time difference between the TPC single-scatter and OD and Skin pulses. For AmLi, this is shown in Figure 4.4.

Compiling the heat maps of efficiency and deadtime for a variety of veto windows, a choice of thresholds were chosen to maximise efficiency whilst minimising dead time. An example plot we used to determine this is shown in Figure 4.9. For SR3, we took the approach of trying to maintain the efficiency of SR1 veto of  $\sim 90\%$ , and to reduce the livetime impact. From the heatmaps, we determined that we could achieve an efficiency that at least matched the SR1 efficiency, but with a much lower deadtime. The final cuts are shown in Figure 4.10.

### 4.2.1 Deadtime Stability

The deadtime for each of the veto cuts was checked that it is stable over SR3. This was done by breaking up the SR3-WS file list, in this case, **SR3-WSv7-LZAP-5.8.0**, into month-by-month chunks. On each month, the rate of pulses in the Skin and OD from the second half of Random Trigger data was used; and the rate above threshold - where the threshold is the veto cut - is recorded. The stability of this over SR3 is shown in Figure 4.11.

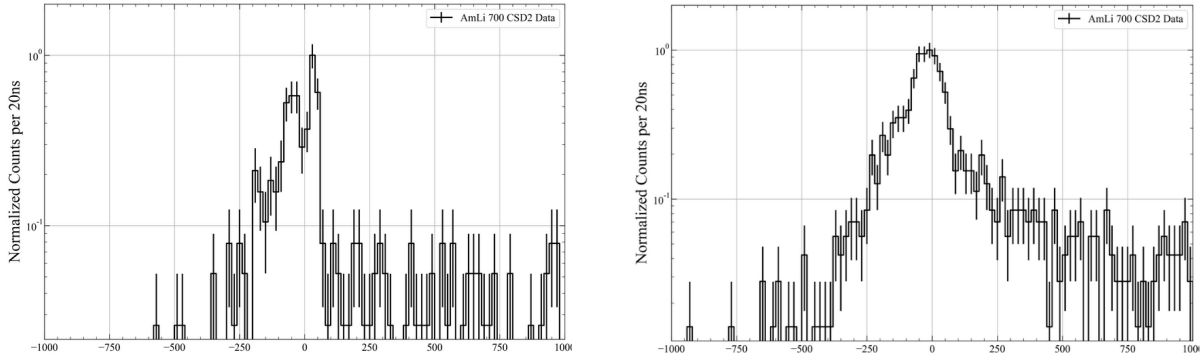
The deadtime is then calculated as;

$$\text{Dead Time [%]} = 1 - e^{-\lambda(x)} \quad (4.1)$$

where  $\lambda$  is the background rate and  $x$ , the veto threshold.

---

<sup>1</sup>in future, a PLR study should be done to determine at what point this is optimised



- (a) Time difference (in ns) between TPC single-scatter and Skin pulses. To reduce the noise in the plot, a pulse requirement of greater than 2 phd and greater than 2 coincidence has been applied to the Skin pulses
- (b) Time difference (in ns) between TPC single-scatter and OD pulses. To reduce the noise in the plot, a pulse requirement of greater than 5 phd and greater than 22 coincidence has been applied to the OD pulses

Figure 4.4: Time difference between TPC single-scatter and Veto pulses. This is used to determine the prompt veto windows.

The conclusion that the dead-time is stable over SR3 was also checked by looking at the ODHealth PREM module, shown in Figure 4.12. The PREM module shows the rate of OD pulses above 200 keV (as defined by the SR1-200 keV not from the SR3 energy calibration), with no significant fluctuation during SR3.

## 4.3 Neutron Veto Efficiency

In this section, the efficiency of tagging background neutrons using the Skin and OD detectors is calculated. This is performed by calculating the efficiency on AmLi and DD calibration data. This is then compared to AmLi and DD simulations. The difference between these simulations and data are then used to calculate an offset. The efficiency is then calculated for detector NR simulations and the offset applied (either a subtraction or a scaling, discussed later). This gives the neutron tagging efficiency for background neutrons.

### 4.3.1 Efficiency Calculation

The efficiency is defined as;

$$\epsilon[\%] = \frac{\text{N. Events passing Analysis Cuts} + \text{Veto Cuts}}{\text{N. Events passing Analysis Cuts}} \times 100 \quad (4.2)$$

and the inefficiency is defined as  $100 - \epsilon$ .

### 4.3.2 Neutrons From Calibration Sources

#### AmLi

The AmLi calibration runs are from the May-2023 calibration period before SR3, with run control operation name **Aml-B**. The runs used are; 13004–13026. All files were processed with LZap–5.8.0.

On these events, the selection of cuts were applied. The majority of which are ‘standard’ SR3 cuts which are listed in Table 4.1. In addition to the cuts listed in Table 4.1, two other categorises of cuts were applied;

1. CSD tube: This is a circular cut on the reconstructed position of the SS in the TPC so that events from just one CSD tube are selected at a time. To make the comparison between

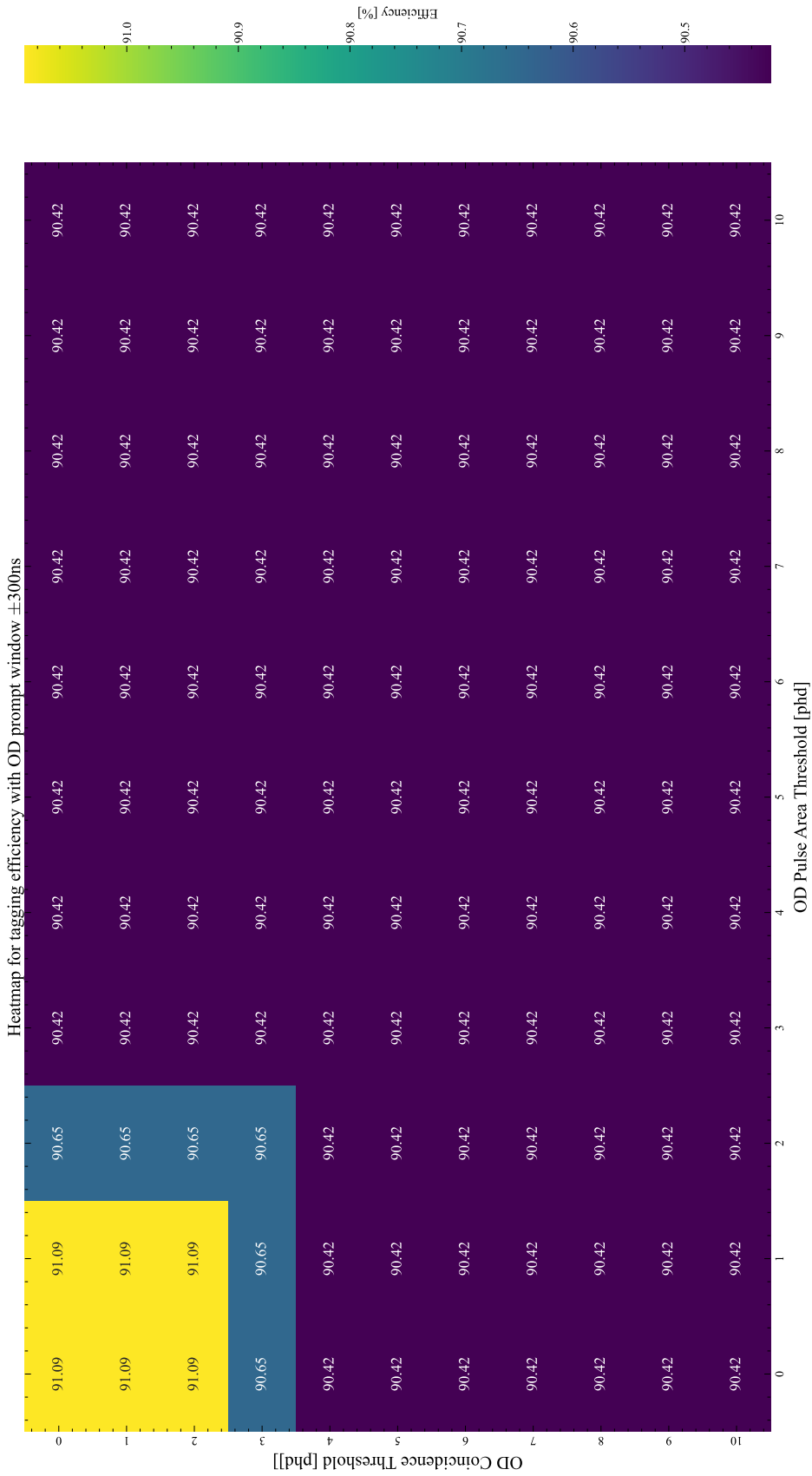


Figure 4.5: OD Prompt heatmap. The z-axis shows the efficiency associated with a given pulse requirement. The veto time window considered is  $[-300, 300]\text{ms}$ .

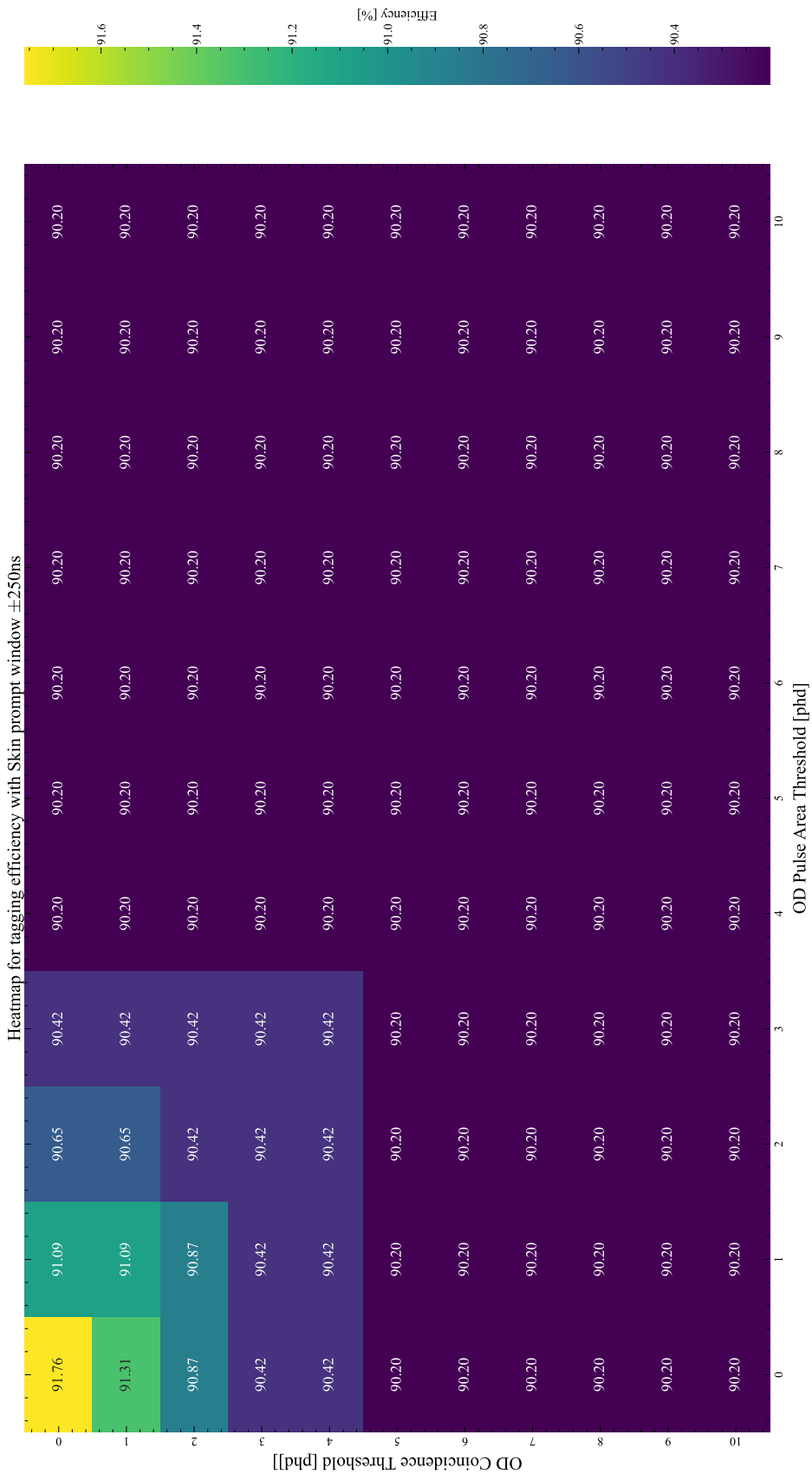


Figure 4.6: Skin Prompt heatmap. In each bin, either the pulse coincidence or the pulse threshold has been varied. The z-axis shows the efficiency associated with a given pulse requirement. The veto time window considered is [-250, 250]ns.

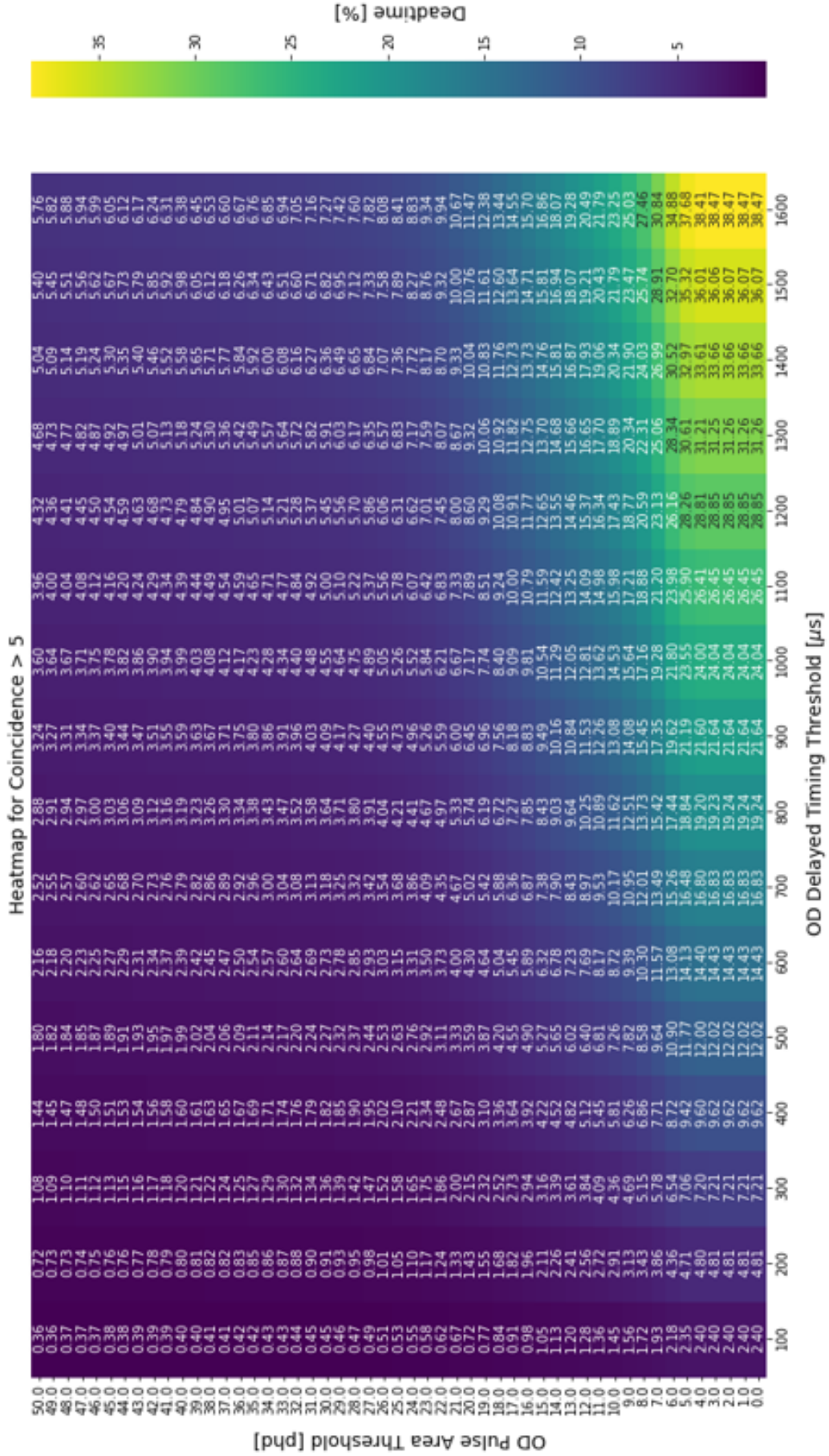


Figure 4.7: OD Delayed heatmap. In each bin, either the veto window or the pulse threshold has been varied. The z-axis shows the deadline associated with a given veto window and pulse threshold. In addition to the pulse area threshold, the pulse must have a coincidence greater than 5.

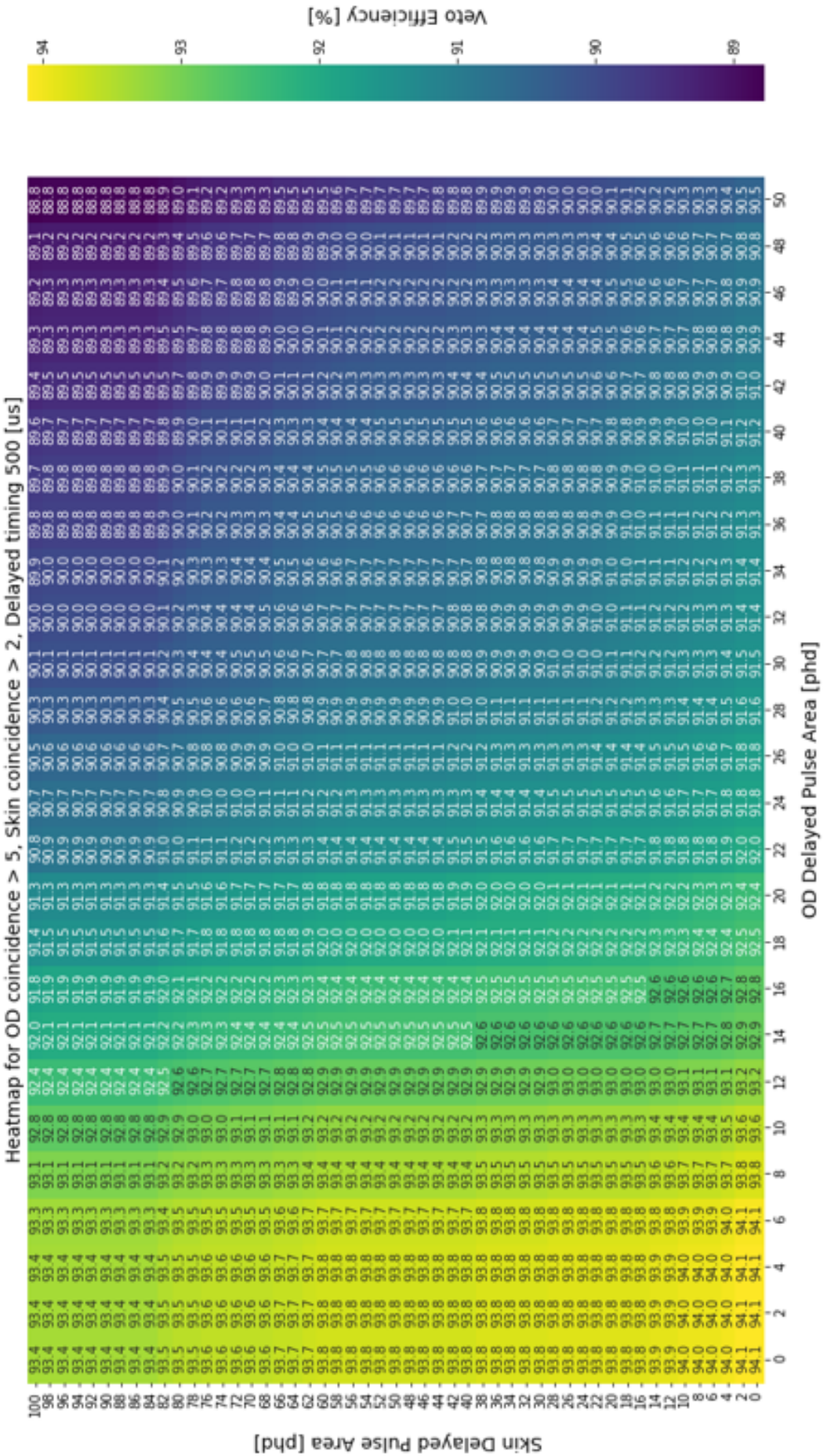


Figure 4.8: Delayed vetoes heatmap. In each bin, the OD pulse threshold or the Skin pulse threshold has been varied. The z-axis shows the veto efficiency associated with a given pulse thresholds. In addition to the pulse area threshold, the OD pulse must have a coincidence greater than 5, and the Skin pulse greater than 2. The veto window in this case is 500 $\mu$ s.

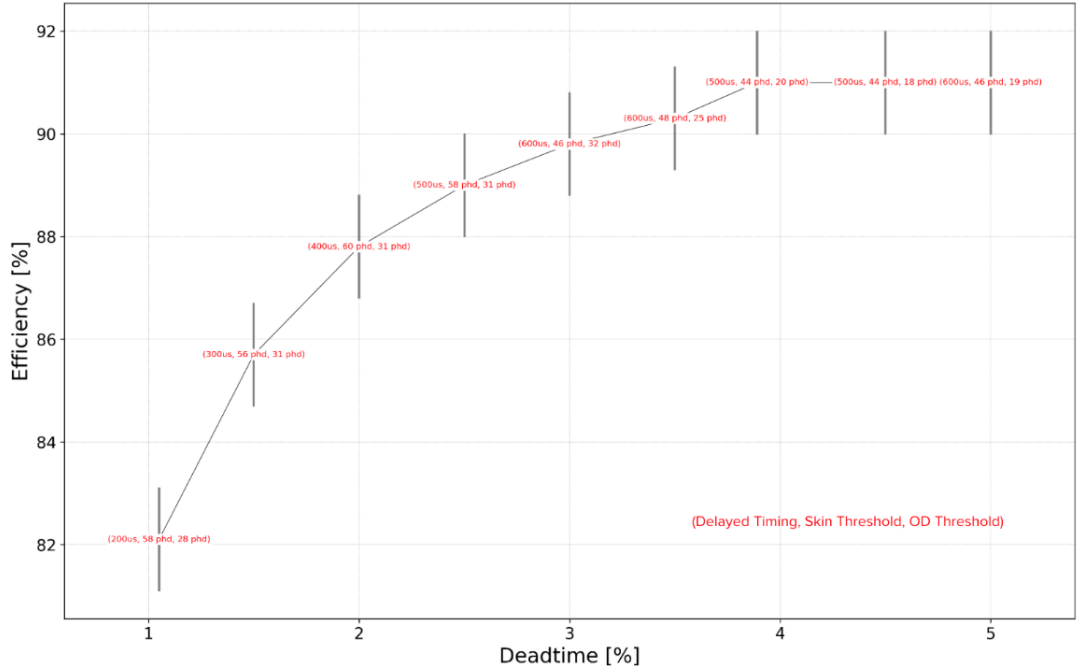


Figure 4.9: Deadtime-vs-efficiency highlighting a number of considered cuts. At each point, the numbers in brackets are; the delayed veto window length after the TPC single-scatter, the Skin threshold pulse area, and the OD threshold pulse area.

Skin Prompt		OD Prompt			
SR3	SR1	SR3	SR1		
Window:	[−250, 250] ns	[500, 500] ns	Window:	[−300, 300] ns	[300, 300] ns
Coincidence:	> 2	> 2	Coincidence:	> 5	> 5
Pulse Area:	> 2.5	> 2.5	Pulse Area:	> 4.5	> 0

Skin Delayed		OD Delayed			
SR3	SR1	SR3	SR1		
Window:	[250ns, 600us]	[500ns, 1200us]	Window:	[300ns, 600us]	[300ns, 1200us]
Coincidence:	> 2	> 55	Coincidence:	> 5	> 5
Pulse Area:	> 46	> 50	Pulse Area:	> 32.0	> 37.5

Figure 4.10: Cuts determined to be optimal for SR3. The SR3 thresholds have a position correction in Z. The SR1 cuts are also included.

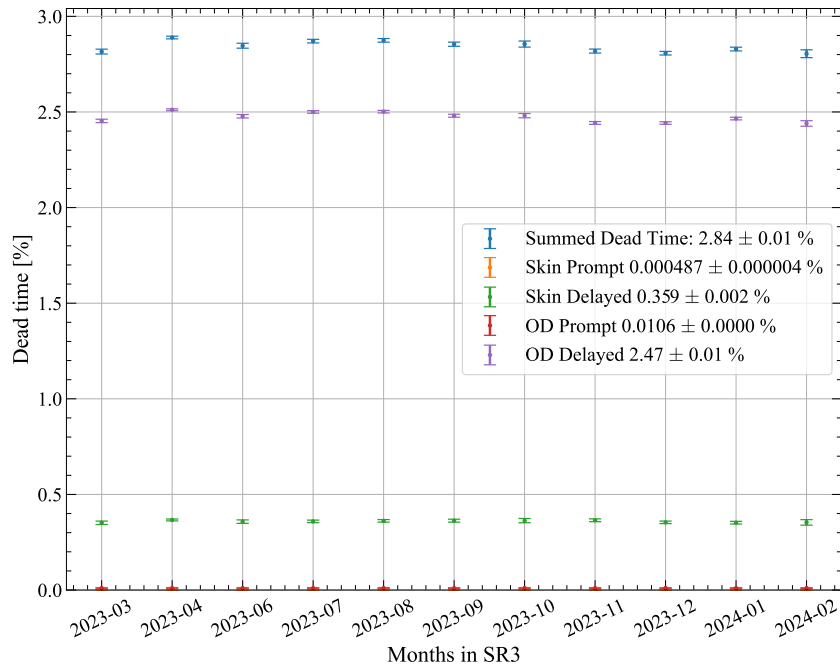


Figure 4.11: Deadtime from the Skin and OD veto cuts during each month of SR3. The error shown in purely statistical.

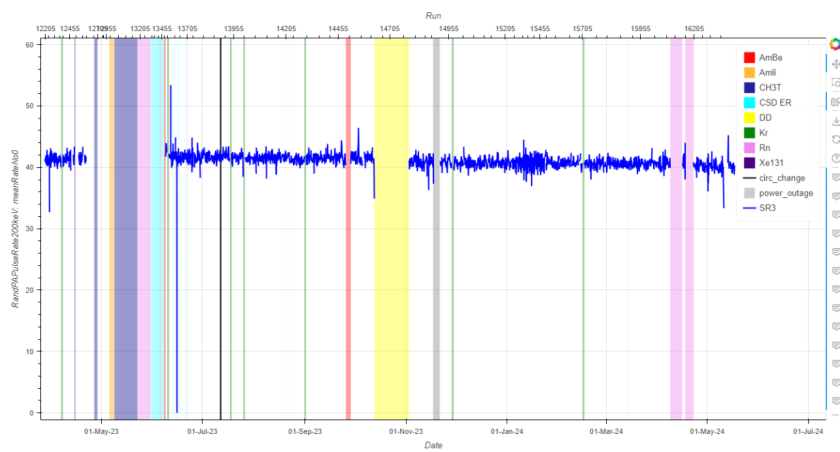


Figure 4.12: Rate of OD pulses above 200keV as defined by SR1 not SR3.

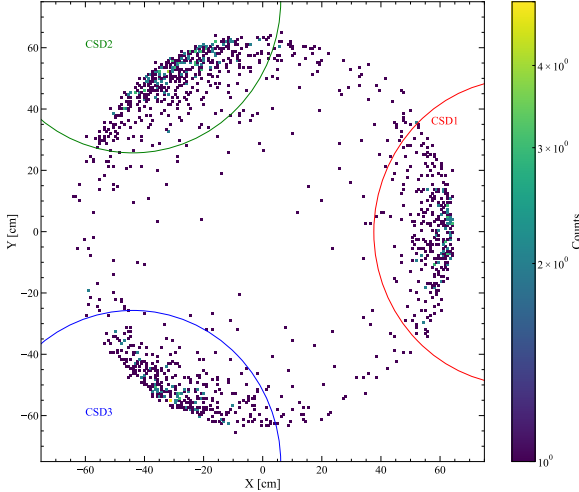


Figure 4.13: X-Y distribution of events in the TPC for AmLi sources positioned at 700mm. Each of the circular cuts are overlaid onto the plot.

data and simulation this cut is required because in simulation only one source in one tube was simulated as opposed to deploying a source in each CSD tube simultaneously. This is useful for examining the fluctuation in neutron tagging efficiency with  $(x, y, z)$ . When the efficiency is averaged across different heights and CSD tube, the average can then be replicated in both data and simulation. The cut uses the following logic;

```
def CSDSelection(x: float, y: float, which_csd: int=1):
    cent_csd_x = [87.6, -43.9, -43.9]
    cent_csd_y = [-0.13, 75.7, -75.7]
    x_el = pow((x-cent_csd_x[which_csd]), 2)
    y_el = pow((y-cent_csd_y[which_csd]), 2)
    r2_el = x_el + y_el
    return r2_el < 50**2
```

How this looks in  $(x, y)$  is shown in Figure 4.13. A concern of this cut is that events towards the centre of the TPC are excluded. However, the position averaged efficiency when the CSD cut and not is  $(88.21 \pm 1.03)\%$  and  $(88.25 \pm 1.22)\%$  respectively. Across the  $600\mu\text{s}$  window, there is no greater than 2% difference between when the cut is and isn't applied. This comparison can be seen in Figure 4.14.

2. NR-band: This is a 1-, 3-, or  $5-\sigma$  cut around the NR band median. The purpose of this cut is to improve the purity of the selection. In this note, the  $1-\sigma$  is used. The band can be found on NERSC at [/global/cfs/cdirs/lz/physics/NEST\\_Bands/SR3/20240313/Calibration](https://global.cfs.cdifs.lz/physics/NEST_Bands/SR3/20240313/Calibration), if the band has been, it can be recreated with the Woods parameters listed below;

The Woods Function Fit Parameters for the Band Mean are: [-6.7099328752961]  
The Woods Function Fit Parameters for the  $-1$  Sigma Line are: [-7.995805026]  
The Woods Function Fit Parameters for the  $+1$  Sigma Line are: [-5.428217339]

The three different NR bands for the three calibration sources can be seen in Figure 4.15.

### AmLi Accidental Correction

When determining the veto tagging efficiency a correction must be applied to the measured efficiency to account for the accidental coincidences from AmLi gammas (and neutrons) with single scatter nuclear recoils in the TPC which can artificially enhance the measured tagging

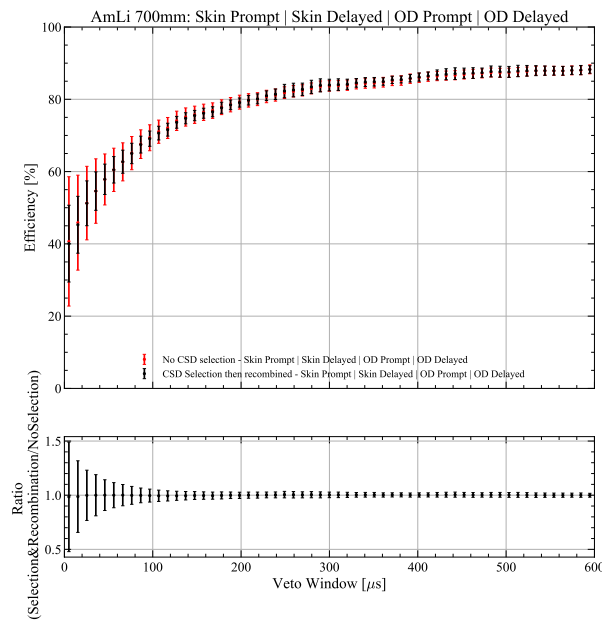


Figure 4.14: The veto efficiency (from all analysis cuts) at using AmLi at 700mm. The ratio plot shows the less than 2% difference between method 1 and method 2.

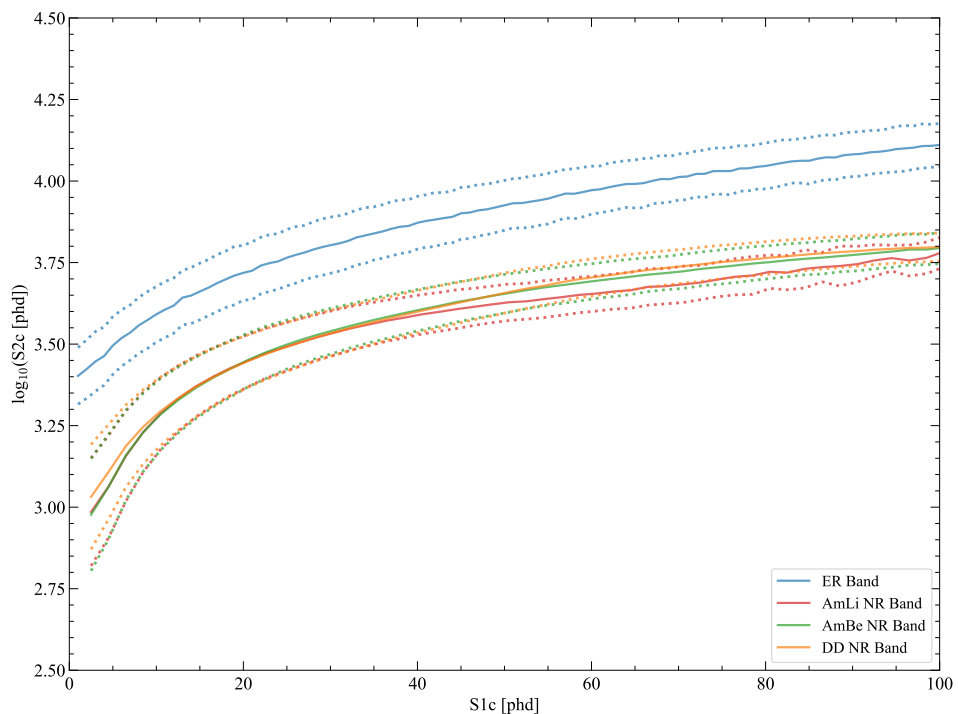


Figure 4.15: The three different NR bands used for the NR-band cut for the respective sources, AmLi, DD and AmBe.

Livetime cuts	Physics cuts	S1 cuts	S2 cuts
Burst noise cut	Single scatter	S2 width vs drift time	S1 prominence cut
Muon holdoff	S1 and S2 threshold	Narrow S2	Stinger event cut
Sustained rate cut	Fiducial Volume	S2 rise time	S1 TBA vs drift time
High S1 rate exclusion		S2 early peak	S1 HSC cut
Bad buffer cuts		S2 XY quality	S1 shape
Excess Area cut		S2 TBA (above-anode gas)	S1 photon timing

Table 4.1: ALPACA-Core SR3 cuts used on AmLi calibration data for determining the efficiency.  
Each cut is from SR3-cuts-v3.

efficiency. First, veto inefficiency must be defined. Every time a single scatter nuclear recoil is observed in the TPC, a veto window is opened, this can be recorded using a counter,  $N$  every time this happens. If there is no pulse observed in the Skin or the OD that satisfies the veto requirements, this event is not vetoed and recorded using a counter,  $M$ . Resulting in a total inefficiency,  $M/N$ , and a total efficiency,  $1 - M/N$ . The effect of the accidentals be a result of the following process. If a neutron enters the TPC, scatters and is not detected by the vetos, the counter  $M$  should be iterated but there is an accidental coincidence of a gamma or a neutron from the AmLi sources with the TPC scatter so the count is not iterated. The probability of this happening can be written as  $1 - P_a(0)$ , where  $P_a(0)$  is the probability of seeing zero accidental pulses in the Skin and OD coincidence windows. Using probability and the counters, the true inefficiency is described below,

$$\begin{aligned} M_{\text{observed}} &= M_{\text{true}} - M_{\text{true}}(1 - P_a(0)) \\ M_{\text{observed}} &= M_{\text{true}}P_a(0) \rightarrow M_{\text{true}} = M_{\text{observed}}/P_a(0) \\ \text{Ineff}_{\text{true}} &= M_{\text{true}}/N \text{ and } \text{Ineff}_{\text{observed}} = M_{\text{observed}}/N \\ \Rightarrow \text{Ineff}_{\text{true}} &= \text{Ineff}_{\text{observed}}/P_a(0) \end{aligned}$$

Due to the logic of the inefficiency calculation is that the  $M$  counter iterates in an AND condition such that all coincidence windows in all detector have to be empty. This leads to a final inefficiency of,

$$\text{Ineff}_{\text{true}} = \text{Ineff}_{\text{obs}}/(1 - P_a(> 0)_{\text{any window}}) \quad (4.3)$$

$P_a(> 0)_{\text{any window}}$  can be determined directly using the post-trigger window of randomly triggered events (GPS events) and count any pulses in **any** of the veto detectors. The accidental correction is correlated with the length of the veto window, scans over the entire delayed veto window in  $10\mu\text{s}$  steps, the change in the correction factor over time can be seen in Figure 4.16. The impact of the accidental correction when applied to the efficiency can be seen in Figure 4.18.

## DD Direct

The DD calibration runs are from the October-2023 calibration period during SR3, with run control operation name **DD Plasma**. The runs used are; 14631–14654. All files were processed with LZap–5.8.0.

The analysis for DD follows a logic similar to the AmLi described in subsection 4.3.2. The cuts used for DD are listed in Table 4.2. In addition to these cuts, an NR band cut was also applied. It is important to note that this NR band is different to the one used for AmLi. The three different NR bands for the three calibration sources can be seen in Figure 4.15. The band can be found on NERSC at /global/cfs/cdirs/lz/physics/NEST\_Bands/SR3/20240313/Calibration, if it has been moved, it can be recreated with the Woods parameters listed below;

The Woods Function Fit Parameters for the Band Mean are: [−19.937161961102728,  
The Woods Function Fit Parameters for the 10% CL Line are: [−17.63553702315951

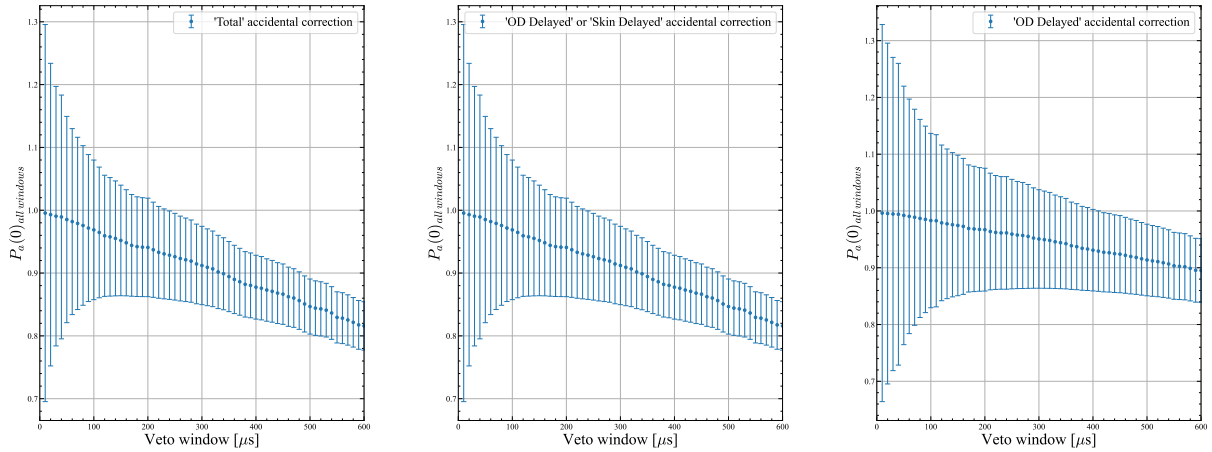


Figure 4.16:  $P_a(> 0)_{\text{all window}}$  AmLi Accidental correction factors for varying veto window size for different windows of interest.

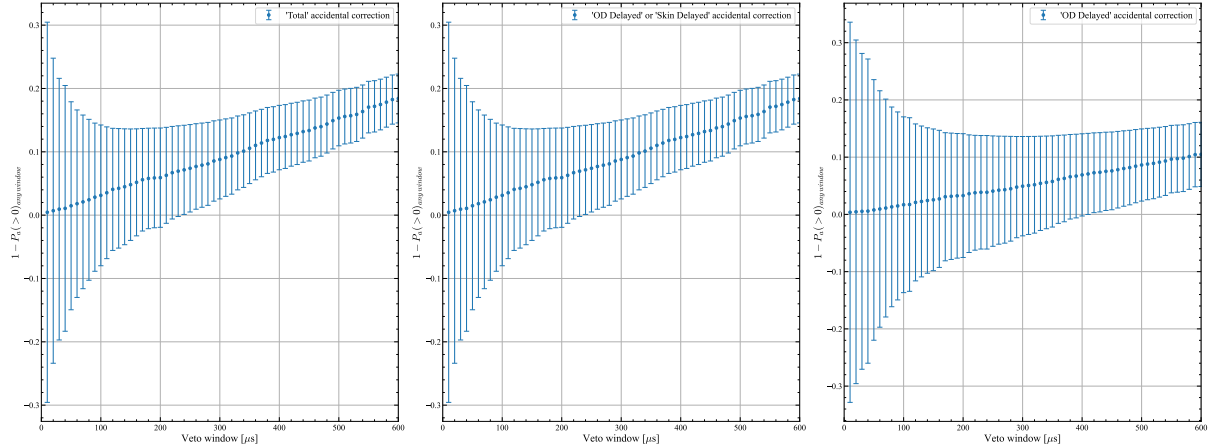


Figure 4.17:  $1 - P_a(> 0)_{\text{anywindow}}$  AmLi Accidental correction factors for varying veto window size for different windows of interest.

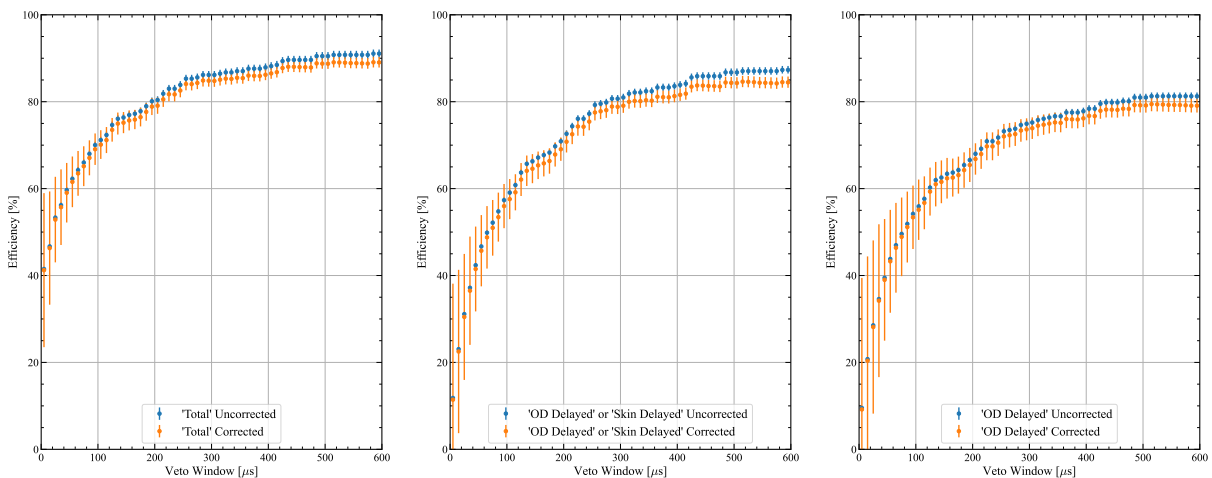


Figure 4.18: The impact of the accidental correction applied to the different veto efficiencies for the given windows of interest. AmLi data at a height of 700 mm in CSD1 has been used here as an example.

Physics cuts	S1 cuts	S2 cuts
Single scatter	S2 width vs drift time	S1 prominence cut
S1 and S2 threshold	Narrow S2	Stinger event cut
Fiducial Volume	S2 rise time	S1 TBA vs drift time
	S2 early peak	S1 HSC cut
	S2 XY quality	S1 shape
	S2 TBA (above-anode gas)	S1 photon timing

Table 4.2: ALPACA-Core SR3 cuts used on DD calibration data for determining the efficiency. Each cut is from SR3-cuts-v3.

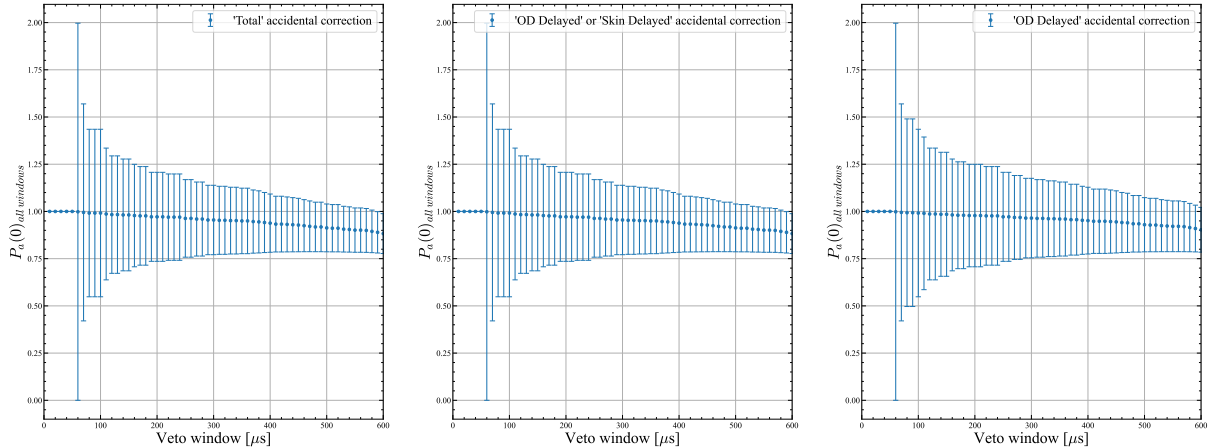


Figure 4.19:  $P_a(> 0)_{\text{all windows}}$  DD Accidental correction factors for varying veto window size for different windows of interest.

The Woods Function Fit Parameters for the 90% CL Line are: [-32.02840007751605]

### DD Accidental Correction

The DD calibration data was also corrected for accidentals. The same method was used which was previously discussed in subsubsection 4.3.2. The correction factors used as a function of veto window can be seen in Figure 4.21. The impact of the accidental corrections on the DD veto efficiency can be seen in Figure 4.19.

#### 4.3.3 Simulated Neutrons From Calibration Source

AmLi and DD were simulated using BACCARAT-6.3.5 and LZLAMA-3.5.3. On each set of simulation, the cuts listed in Table 4.3 were used. No accidental correction was applied to the simulation data as there are no accidental gammas or neutrons present in the simulation. How these compare to the data measurements are shown in Figure 4.22-4.23. More detailed plots on how the calibration simulations compare to calibration data is in Section 4.1.

Physics cuts
Single scatter
S1 and S2 threshold
Fiducial Volume
CSD Selection (AmLi Only)

Table 4.3: ALPACA-Core SR3 cuts used on AmLi and DD simulations for determining the efficiency. Each cut is from SR3-cuts-v3.

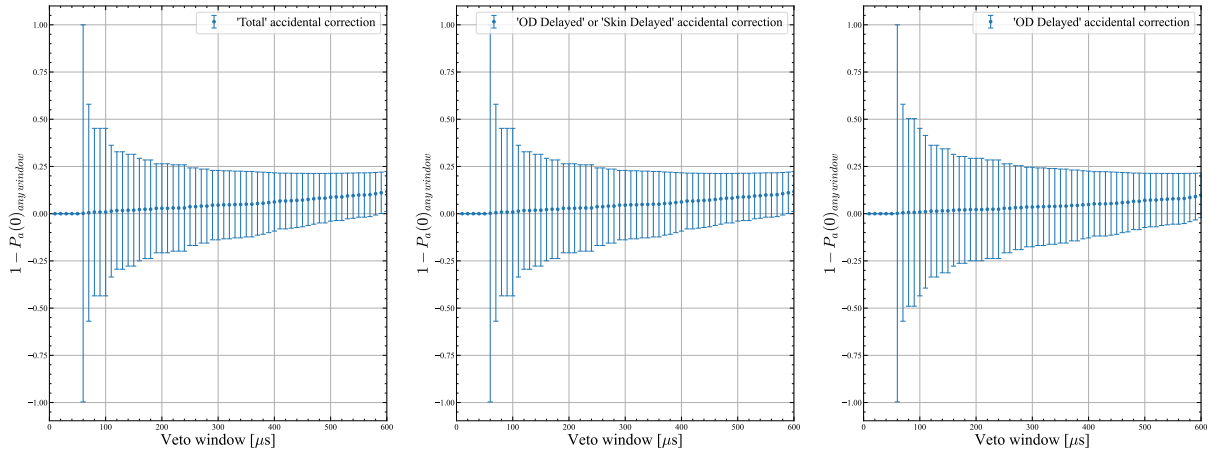


Figure 4.20:  $1 - P_a(> 0)_{\text{any window}}$  DD Accidental correction factors for varying veto window size for different windows of interest.

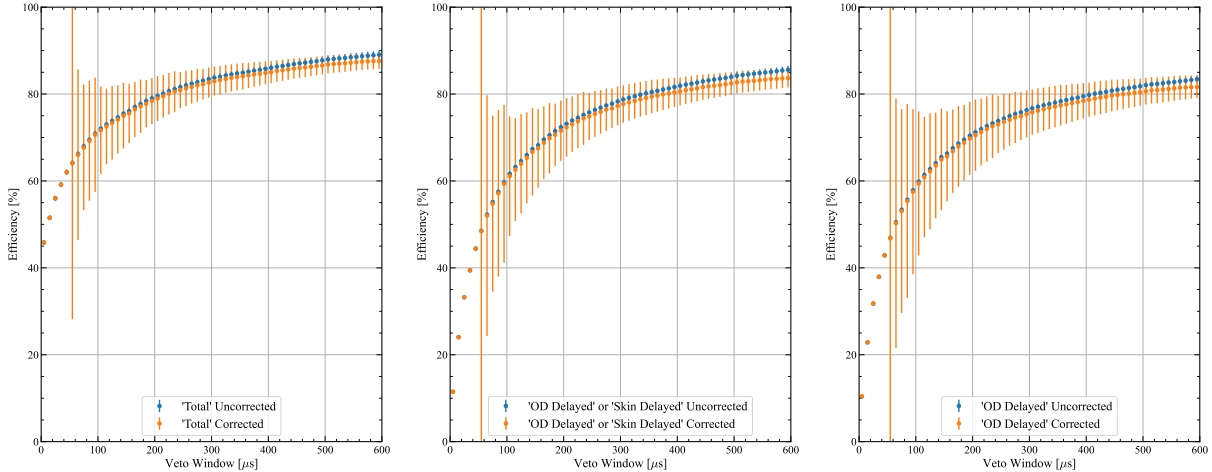


Figure 4.21: The impact of the accidental correction applied to the different veto efficiencies for the given windows of interest.

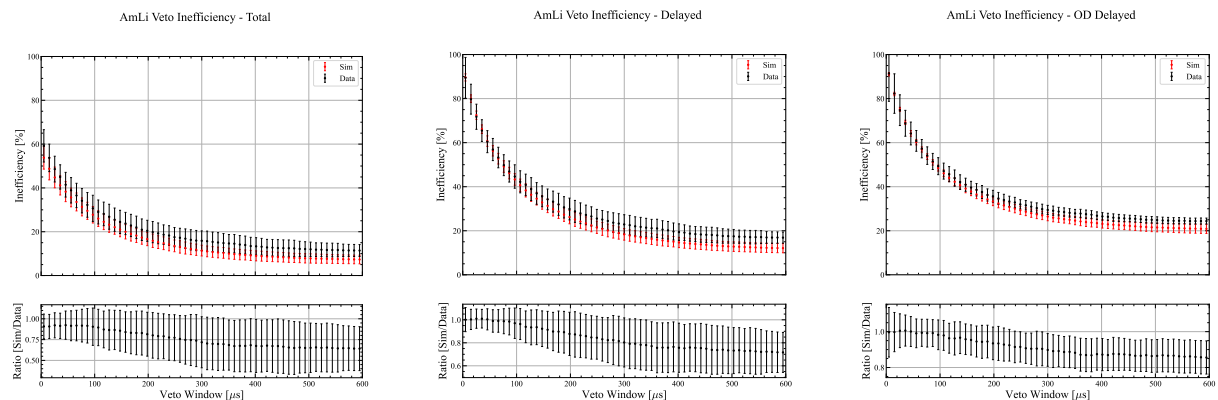


Figure 4.22: Inefficiency plots for AmLi, comparing simulations to data. Left: Total. Middle: Delayed Only. Right: OD Delayed.  
In each case, the average from all CSD positions are used.

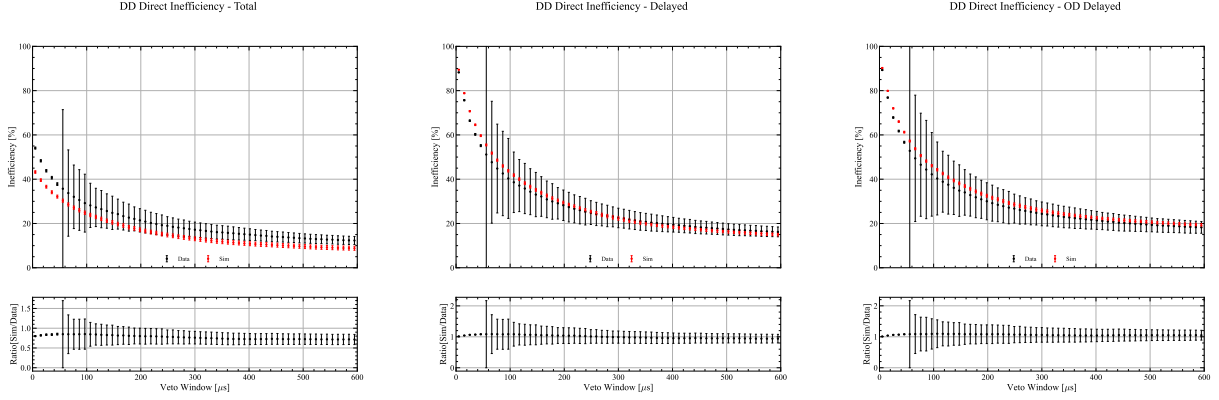


Figure 4.23: Inefficiency plots for DD, comparing simulations to data.  
Left: Total. Middle: Delayed Only. Right: OD Delayed.

Physics cuts  
 Single scatter  
 S1 and S2 threshold  
 Fiducial Volume

Table 4.4: ALPACA-Core SR3 cuts used on Detector-NR simulations for determining the efficiency. Each cut is from SR3-cuts-v3.

#### 4.3.4 Background Neutrons

The detector-NR simulations were simulated as part of the official production of SR3-BG. Each of the 644 components were simulated using BACCARAT-6.3.5 and LZLAMA-3.5.3. On these events, the cuts listed in Table 4.4 were applied. The efficiency of tagging neutrons from USF and ( $\alpha, n$ ) events are shown in Figure 4.24. Also shown is the total efficiency.

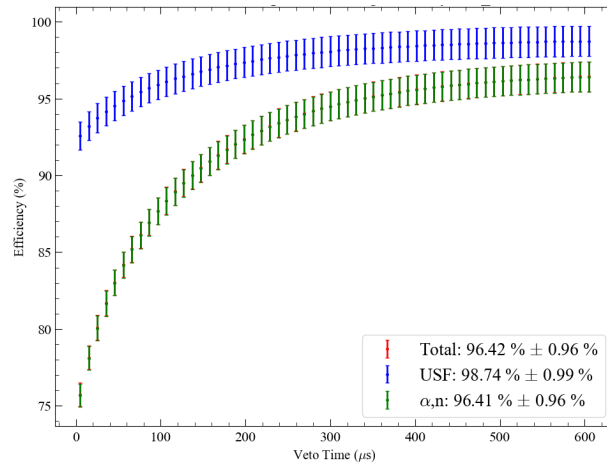


Figure 4.24: Efficiency for tagging a neutron on Detector-NR simulations.

### 4.3.5 Background Neutron Efficiency From Data

Shown in Figure 4.25 is the neutron veto efficiency from each calibration source from data and simulation. Also shown is the efficiency from simulated background neutrons. The Z-position of each point is calculated from the mean(driftTime) of events which pass the selection. For the Detector-NR, the events were split up into Z-sections by the following;

```
def SR3ZThirds_Cut(driftTime_us: float, position='top'):
    if position == 'top':
        return ((driftTime_us < 350.) & (driftTime_us > 71.))
    elif position == 'mid':
        return ((driftTime_us < 700.) & (driftTime_us > 350.))
    elif position == 'bot':
        return ((driftTime_us < 1030.) & (driftTime_us > 700.))
```

This driftTime splitting was performed so that comparing to calibration points was easier, but in evaluating the total efficiency, it is not used.

Shown in Table 4.5 are the veto efficiencies of all calibration sources for both simulations and data. The value we care about is the background neutron efficiency,  $\epsilon_{\text{bg data}}$ , or inefficiency,  $\zeta_{\text{bg data}}$ . There are a number of ways in which this can be calculated, which are described below. The proposed option is no.2, of  $7.8 \pm 4.3\%$ ; or quote as  $8 \pm 4$ . Table 4.6 contains the results of each approach.

**Option 1** : We take the average simulation calibration efficiency, so the mean of AmLi (92.8%) and DD (91.8%), then we have 92.3%. We take the average data calibration efficiency, 88.6% for AmLi and 87.7%, for DD we have 88.2%. The ratio,  $\Delta$ , of the simulation calibrations and the data calibration can then be used as a scaling factor on the simulation background. This process is expressed in Equation 4.7, and gives an efficiency of 92.1%. In this case, the uncertainty is 4.5%, made up from a statistical error from the simulations (0.96%), and 4.3 from the scaling.

$$\epsilon_{\text{cal. data}} = \frac{\epsilon_{\text{data DD}} + \epsilon_{\text{data AmLi}}}{2} \quad (4.4)$$

$$\epsilon_{\text{cal. sims}} = \frac{\epsilon_{\text{sims DD}} + \epsilon_{\text{sims AmLi}}}{2} \quad (4.5)$$

$$\Delta = \frac{\epsilon_{\text{cal. data}}}{\epsilon_{\text{cal. sims}}} \quad (4.6)$$

$$\epsilon_{\text{bg data}} = \Delta \times \epsilon_{\text{bg sims}} \quad (4.7)$$

**Option 2** : We take the average simulation calibration efficiency, so the mean of AmLi (92.8%) and DD (91.8%), then we have 92.3%. We take the average data calibration efficiency, 88.6% for AmLi and 87.7%, for DD we have 88.2%. The difference,  $\Lambda$ , between the simulation calibrations and the data calibrations can then be used as a systematic uncertainty on the simulation backgrounds. This process is expressed in Equation 4.11, and gives an efficiency of 92.2%. In this case, the uncertainty is 4.3%, made up from a statistical error from the simulations (0.96%), and 4.22 from the subtraction.

$$\epsilon_{\text{cal. data}} = \frac{\epsilon_{\text{data DD}} + \epsilon_{\text{data AmLi}}}{2} \quad (4.8)$$

$$\epsilon_{\text{cal. sims}} = \frac{\epsilon_{\text{sims DD}} + \epsilon_{\text{sims AmLi}}}{2} \quad (4.9)$$

$$\Lambda = \epsilon_{\text{cal. sims}} - \epsilon_{\text{cal. data}} \quad (4.10)$$

$$\epsilon_{\text{bg data}} = \epsilon_{\text{bg sims}} - \Lambda \quad (4.11)$$

**Option 3** : We take the average simulation calibration inefficiency, so the mean of AmLi ( $100 - 92.8 = 7.2\%$ ) and DD ( $100 - 91.8 = 8.3\%$ ), then we have  $7.7\%$ . We take the average data calibration inefficiency,  $11.5\%$  for AmLi and  $12.3\%$  for DD, we have  $11.9\%$ . The ratio,  $\Delta$ , of the simulation calibrations and the data calibration can then be used as a scaling factor on the simulation background. This process is expressed in Equation 4.15, and gives an inefficiency of  $5.5$ . In this case, the uncertainty is  $2.8\%$ , made up from a statistical error from the simulations ( $0.96\%$ ), and  $1.8$  from the subtraction.

$$\zeta_{\text{cal. data}} = 100 - \frac{\epsilon_{\text{data DD}} + \epsilon_{\text{data AmLi}}}{2} \quad (4.12)$$

$$\zeta_{\text{cal. sims}} = 100 - \frac{\epsilon_{\text{sims DD}} + \epsilon_{\text{sims AmLi}}}{2} \quad (4.13)$$

$$\Delta = \frac{\zeta_{\text{cal. data}}}{\zeta_{\text{cal. sims}}} \quad (4.14)$$

$$\zeta_{\text{bg data}} = \zeta_{\text{bg sims}} \times \Delta \quad (4.15)$$

Source	Simluation	Data
AmLi (average)	$92.8 \pm 2.0\%$	$88.6 \pm 2.7\%$
DD (Direct)	$91.8 \pm 1.0\%$	$87.7 \pm 1.8\%$
Detector-NR	$96.4 \pm 1.0\%$	$92.2 \pm 4.3$

Table 4.5: Summary of veto efficiencies. The Detector-NR Data value assumes that option 2 is used.

Option	efficiency	inefficiency
No. 1	$92.1 \pm 4.5$	$7.9 \pm 4.5$
No. 2	$92.2 \pm 4.3$	$7.8 \pm 4.3$
No. 3	$94.5 \pm 2.8$	$5.5 \pm 2.8$

Table 4.6: Summary of veto efficiencies and inefficiencies as determined from each approach.

#### 4.4 Veto Efficiency and the WIMP search

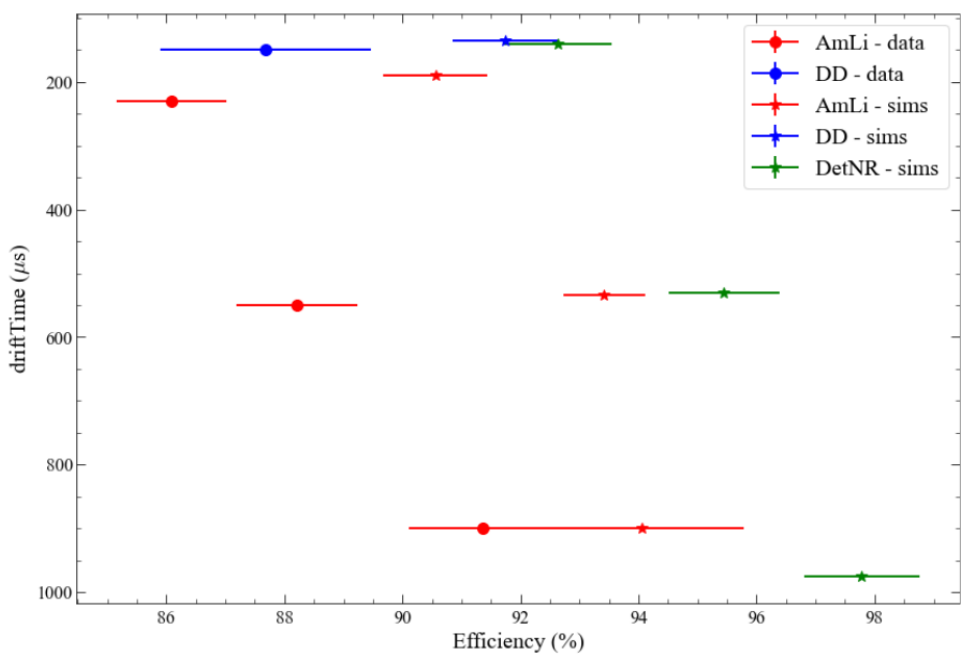


Figure 4.25: Summary of efficiency from all simulations and calibration sources. The CSD sources are averaged at each height. Circle marks are from data. Start marks are from simulations. The driftTime is defined as when mean(driftTime) of events which pass all other cuts.

# 5 Muons

## 5.1 Veto for WIMP Search

### 5.1.1 Motivation

### 5.1.2 Cut Description

## 5.2 Flux Measurement

Our initial muon model described in Ref. [25] has been used to calculate muon fluxes that can be compared with previous measurements. Vertical muon intensity has been calculated as  $5.18 \times 10^{-9} \text{ cm}^{-2} \text{ s}^{-1} \text{ sr}^{-1}$ , in good agreement with the value of  $(5.38 \pm 0.07 \text{ (stat)}) \times 10^{-9} \text{ cm}^{-2} \text{ s}^{-1} \text{ sr}^{-1}$  [33] measured in the same cavern using the veto system of the Davis experiment (corrected to include multiple muon events). Total muon flux through a spherical detector with unit cross-sectional area has been calculated as  $6.16 \times 10^{-9} \text{ cm}^{-2} \text{ s}^{-1}$ , slightly higher than the recent measurements with the veto system of the Majorana Demonstrator located in the nearby cavern  $(5.31 \pm 0.17 \text{ (stat)}) \times 10^{-9} \text{ cm}^{-2} \text{ s}^{-1}$  [34].

The difference between the two measurements and our initial model, although relatively small (within 20%), pointed to a need for new measurements with the LZ experiment to re-normalise the muon model.

The new muon flux measurements estimate the average density of the rock between the surface and the cavern and will be used to inform the muon model for the DUNE experiment[35], which uses the same MUSUN code and the same rock density.

### 5.2.1 Outline of Model

The muon simulations use two Monte-Carlo codes: MUSIC (MUon SImulation Code) and MUSUN (MUon Simulations UNderground)[36, 37], adapted here for the LZ experiment. Initially, muons with different energies on the surface of the Earth were transported through various distances in rock using MUSIC. The rock composition has been taken from Ref. [38, 39]. Measurements of several rock samples have been reported [38, 39] and the average rock parameters have been calculated as  $\langle Z \rangle = 12.09$  and  $\langle A \rangle = 24.17$ . The average density of rock was assumed to be  $2.70 \text{ g/cm}^3$  [39] in the MUSIC simulation. Other measurements [40], including the measurement of the muon flux with the veto system of the Majorana demonstrator, suggest that the density may be larger ( $2.8\text{-}2.9 \text{ g/cm}^3$ [34]).

The resulting energy spectra of survived muons have been convoluted with muon spectra on the surface of the Earth for different zenith angles and slant depths (see [37] for the procedure's description). The distance from the underground laboratory and the Earth's surface for each azimuth and zenith angle has been obtained from the surface map and the position of the laboratory in the global coordinate system [41]. Muon energy spectrum and zenith angle distribution on the surface of the Earth were calculated using the parametrisation first suggested in Ref. [42] modified for the curvature of the Earth to include large zenith angles. Other corrections, such as muon decay and energy loss in the atmosphere, muon production via charmed meson decay, muon intensity dependence on altitude and geomagnetic rigidity cut-off were not included due to their negligible effect on high-energy muons ( $> 1 \text{ TeV}$ ) capable of reaching the SURF location. As a result of muon transport and convolution with the surface fluxes, muon energy spectra and different angles at the detector site have been calculated and stored in a file. The model gives

the total muon flux through a sphere as  $6.16 \times 10^{-9} \text{ cm}^{-2} \text{ s}^{-1}$ , mean muon energy of 283 GeV, mean zenith angle of  $27^\circ$  and the mean slant depth of 4500 m w. e. [43].

The Muon generator MUSUN inside BACCARAT reads muon distributions from this file and samples muons on the horizontal (top) and vertical surfaces of a box that encompasses the laboratory hall. The top horizontal surface of the box is located 7 metres above the cavern boundary. Vertical surfaces of the box are positioned 5 m away from the boundary. The box extends to 3 m below the cavern floor. Moving the box surfaces into the rock, away from the cavern, ensures the development of muon-induced cascades in rock or shotcrete before muons and their secondaries enter the cavern. The primary energy spectrum and the angular distributions of these muons are illustrated in Figure 5.1.

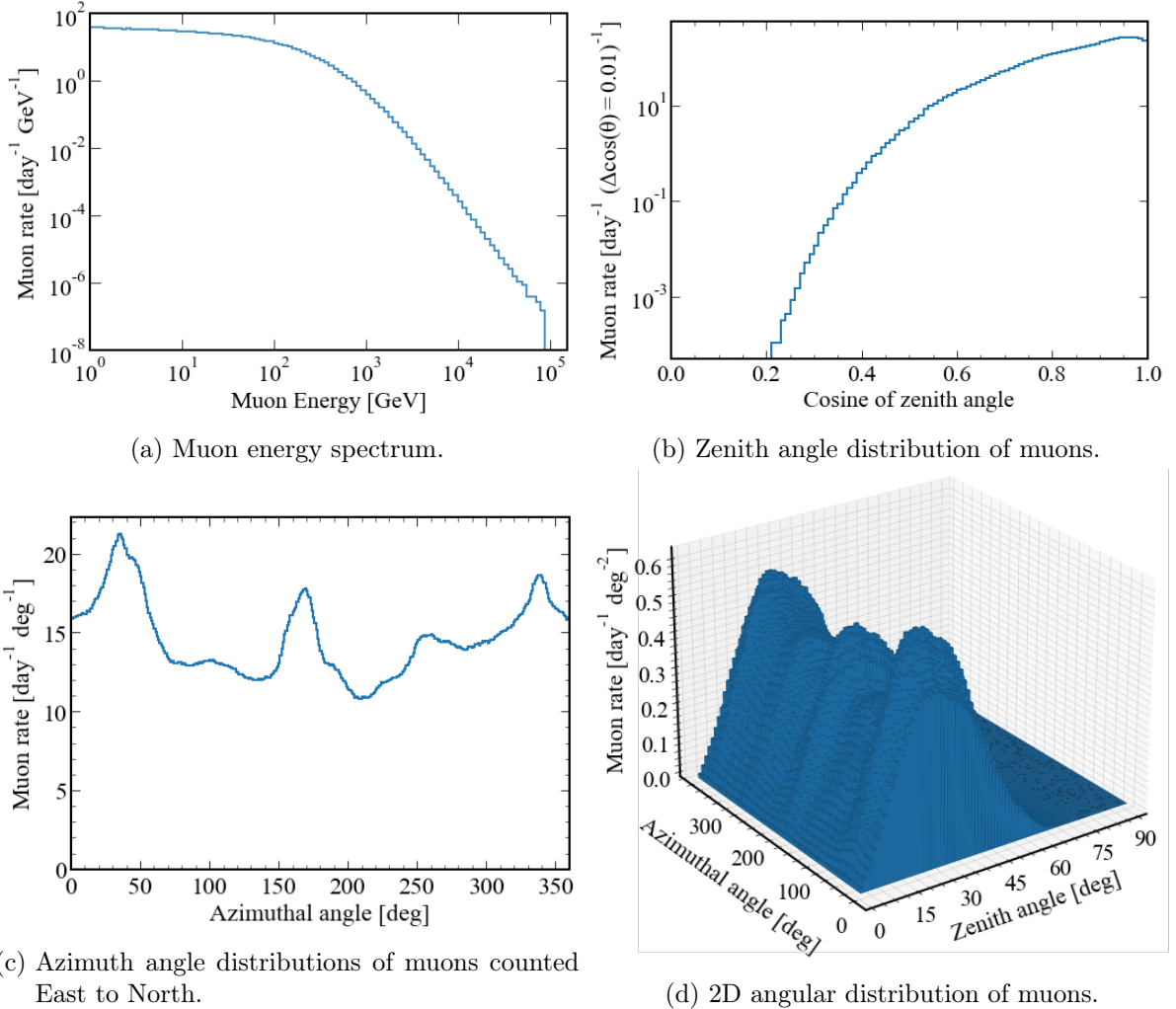


Figure 5.1: Angular distributions and the kinetic energy spectrum of muons at SURF, Davis Campus, as generated by the MUSUN model.

Muons generated by MUSUN have been transported through the rock, laboratory hall and detector geometry using GEANT4 (inside BACCARAT) and their energy depositions in all "sensitive volumes" have been recorded. In this simulation,  $4.82 \times 10^7$  muons have been propagated which corresponds to a live time of 9147 days (0.0609874 muons per second), providing about 30 times higher statistics than for data collected during WIMP search 2022 and WIMP search 2024 (WS2022 & WS2024).

### 5.2.2 Data selection

This study considers the both WS2022 and WS2024 datasets, specifically using the file lists, `SR1-WSv5_LZAP-5.4.6.files.list`, taken from the SR1WS ALPACA module and `SR3-WSv8_LZAP-5.8.0_all.files.list`, taken from the SR3LENR ALPACA module.

Skims of the data sets were performed using the MuonPhys ALPACA module which applied a loose initial selection to reduce the size of the initial dataset for later analysis. This module was also used for determining the live time of the two datasets. The live times are summarised in Table 5.1. For the rate calculation, DAQ live time was chosen as the appropriate live time to use as this analysis is does not consider the same decision logic as used in the physics live time.

Table 5.1: Summary if relevant durations for the WIMP search runs. For this analysis, DAQ livetime was used in the rate calculation work.

Run	Run Time [days]	DAQ Live Time [days]	Physics Live Time [days]
WS2022	99.5	98.8	96.4
WS2024	268.0	267.6	255.4
Total	367.5	366.4	351.8

### Typical Muon Event

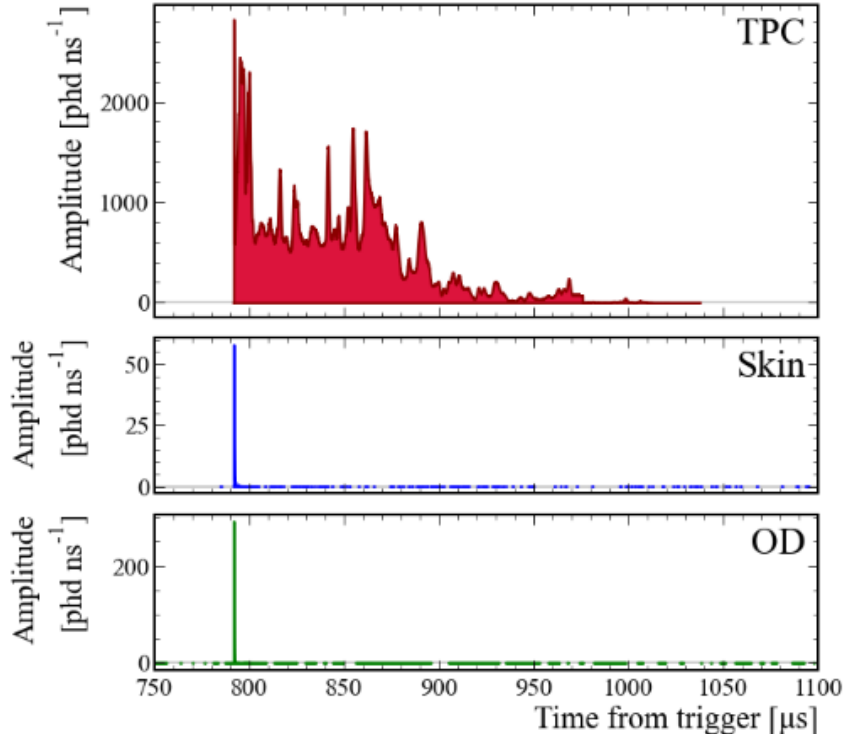


Figure 5.2: Event-viewer output of typical muon event. PMT saturation is evident towards the end of the muon ‘tail’ in the TPC.

### OD Selection

An OD energy threshold was implemented to reduce the probability of random coincidence between the three detectors. The energy deposited in the OD by a muon is the largest, physical signal we will see in the OD. The only other large physical signals we anticipate seeing are neutron captures, the most frequent of which are on gadolinium. Therefore, the OD threshold

was set at the endpoint of the gadolinium neutron capture at  $\sim 8$  MeV which corresponds to 2000 phd. An OD ‘noise cut’, initially developed for the muon veto and ‘hold off’ for the WIMP search, has been used to reduce the impact of burst noise in our flux measurement. During tests of the muon veto, it was found that pulses produced due to the burst noise phenomena could imitate a muon-like signal in the OD. The ratio of pulse area to pulse amplitude enabled the creation of a custom variable called ‘Pulse Shape’. Two distinct distributions can be seen in Figure 5.3a. Events from both distributions were hand scanned using the event-viewer and it was found that pulses with a pulse shape less than 0.003 were noise pulses with the same characteristics as previously observed burst noise.

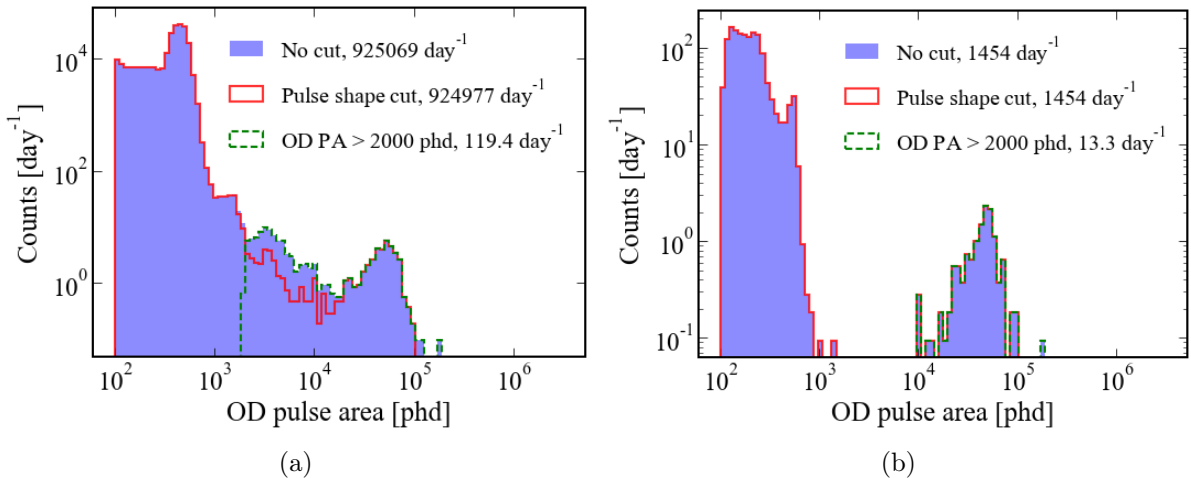


Figure 5.3: Histograms of the largest OD pulse areas in  $\sim 12.5$  million background events from WS2022 before applying inter-detector timing cuts. Pulse shape has been used to differentiate between pulses produced by a muon and pulses produced by noise phenomena observed in the detector. The peak at around 450 phd results from neutron captures on the nuclei of hydrogen atoms and the subsequent emission of a single 2.22 MeV gamma ray. The plots show the impact of the 2000 phd cut and pulse shape cut (a) before and (b) after inter-detector timing coincidences are applied.

## Inter-detector Timing Selection

Cosmic-ray muon events in the LZ experiment can be uniquely identified by their large energy deposits that are coincident in the three detector systems: OD, skin and TPC. As muons move at relativistic speeds, the time difference between pulses in each detector will be small compared to other backgrounds such as neutrons and gamma rays. Broad scans were conducted to make use of the coinciding detector signals to determine the inter-detector timing selection. As shown in Figure 5.4, the time difference distributions between detector volumes allow for distinguishing between muon interactions through all volumes and signals unrelated to muons. Following the scan, three different considerations were made:

1.  $-200 \text{ ns} < \Delta t_{\text{OD-Skin}} < 200 \text{ ns}$
  2.  $-1200 \text{ ns} < \Delta t_{\text{OD-TPC}} < 200 \text{ ns}$
  3.  $-1200 \text{ ns} < \Delta t_{\text{Skin-TPC}} < 200 \text{ ns}$

Here the pulse time,  $t$ , is described using the combination of two RQs, `pulseStartTime_ns+areaFractionTime`. When traversing the TPC, a muon does not produce a singular pulse as observed in the OD and Skin. The muon ionises xenon atoms along the track, and a subsequent series of S1 and S2 pulses are produced. The pulses combine to produce a ‘tail’ as seen in Figure 5.2. The first pulse

in the tail is used in the inter-detector timing selection. Figure 5.3b highlights the effectiveness of the timing cut when used with the Outer Detector selection, reducing the event rate per day from 119.4 to 13.3.

### TPC Energy Selection

The effects of cuts differ between simulations and data due to uncertainty associated with GEANT4 modelling of the muon shower, particularly at lower energies (see Figure 5.5a). As the cuts change, the rates change accordingly, but by different factors for data and simulations. This difference can be observed by examining the ratios of muon flux between the data and the simulations. Therefore, two decisions are required: which gain (high gain, HG, or low gain, LG) should be used for data to normalise the muon model, and what threshold is necessary for energy deposition in the TPC to ensure that the data can be accurately compared with the simulations. To accomplish this, we worked backward from the flux results described in subsection 5.2.5. Comparing HG ratios of data rates to simulated rates with the corresponding LG ratios, as displayed in Figure 5.5b, it is clear that the LG ratios remain steady within statistical errors above 10 MeV. A steady ratio of data and simulation rates was one reason we measured the flux using LG data. A low threshold such as  $< 1$  MeV, would not be useful because these events are not full muon events as seen through handscanning events around this threshold. They tend to be the end of a muon cascade in both data and simulations. Figure 5.6 demonstrates this by showing that most events  $> 10$  MeV are muons, not muon secondaries, as it separates the events with a muon passing through the TPC from those that do not. A higher energy threshold such as  $< 50$  MeV would also not be useful, as Figure 5.5a illustrates, the effect of PMT saturation can be seen above this energy in data.

### Lack of Skin Threshold

This analysis considers a triple coincidence between the OD, Skin and TPC. However, all that is required in the Skin detector is a pulse which is classified as a ‘max pulse’ in LZap and the pulse must have an amplitude greater than 1 phd/ns. Due to the lack of calibration and subsequent energy reconstruction in the skin, it was chosen not to set an energy threshold in the Skin as it would be difficult to make comparisons to the energy-only simulations produced using BACCARAT.

### 5.2.3 NEST - Muon Simulations and Light-Energy Conversion

NEST has been used to reconstruct the energy of muons traversing the TPC. Typically particle interactions are observed through an ‘S1’ pulse and an ‘S2’ pulse and using methods described here [27], the energy deposit can be calculated. When a muon traverses the xenon space, a series of S1 and S2 pulses are produced which can not be separated in data. NEST, however, has a minimum ionising particle (MIP) module in which the linear energy transfer can be set. This is  $2.1 \text{ MeV cm}^2 \text{ g}^{-1}$ [44] for a muon in liquid xenon with an average energy of 283 GeV. Two final inputs to NEST to simulate a muon are the start and end points of the track.

Sampling the start position and direction vector produced by the MUSUN simulations, all 48.2 million muons were projected down towards the LZ detector. If the muon passed through the xenon space, the point at which it entered and exited the TPC was saved and later used as the input into NEST. 67918 muons from BACCARAT passed through the xenon volume and were used towards producing the conversion between energy deposit and light produced due to the interaction. NEST outputs the energy, total S1 light and total S2 light and for the conversion used in this analysis, the S1 and S2 light was summed. Two separate sets of conversion factors were determined through running NEST with the WS2022 LZ detector configuration and WS2024 detector configuration. An example of the comparison can be seen in Figure 5.7. A spline fit was fitted to the NEST data and extrapolated down to the minimum data point at

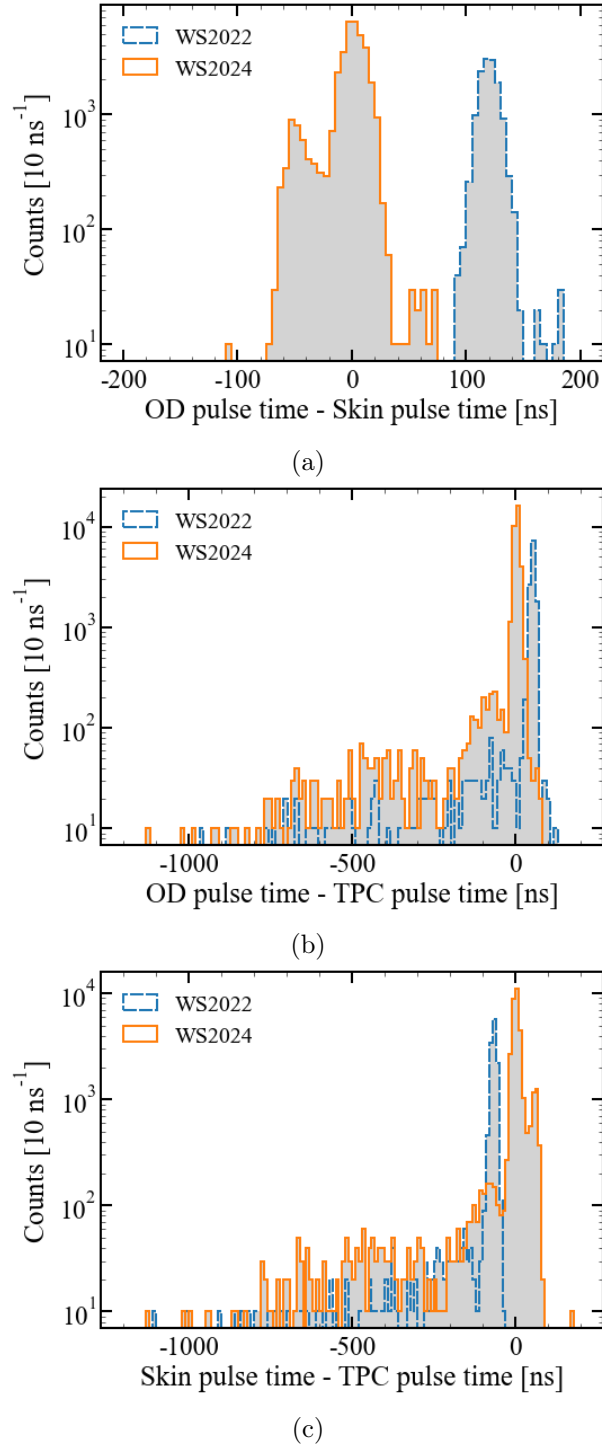


Figure 5.4: Inter-detector timing plots, these distributions were used in defining the timing selection following the skim of the WS2022 and WS2024 datasets looking at events with a pulse greater than 2000 phd in the Outer Detector. The figures depict (a) the time difference between the largest pulse in the Outer Detector and the largest pulse in the Skin; (b) the time difference between the largest pulse in the Outer Detector and the start of the muon tail in the TPC; and (c) the time difference between the largest pulse in the Skin and the start of the muon tail in the TPC.

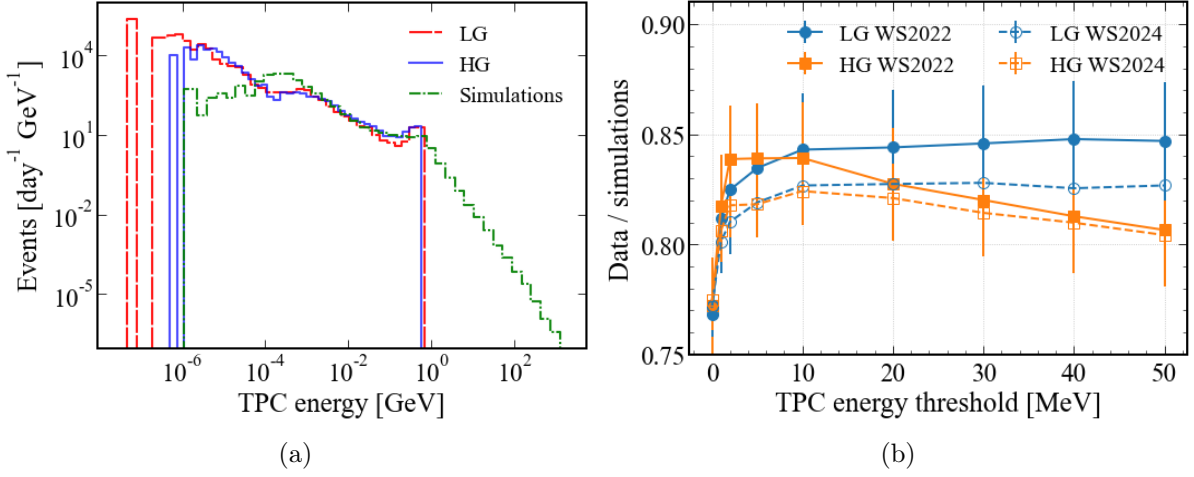


Figure 5.5: (a) Histograms comparing the spectrum of deposited energy in the TPC from BAC-CARAT muons with the spectrum of deposited energy in the TPC from WS2022 and WS2024 HG (LG) data (converted from TPC total pulse area). (b) The ratios of HG (LG) WS2022 and WS2024 data to BACCARAT simulations as a function of the energy threshold in the TPC.

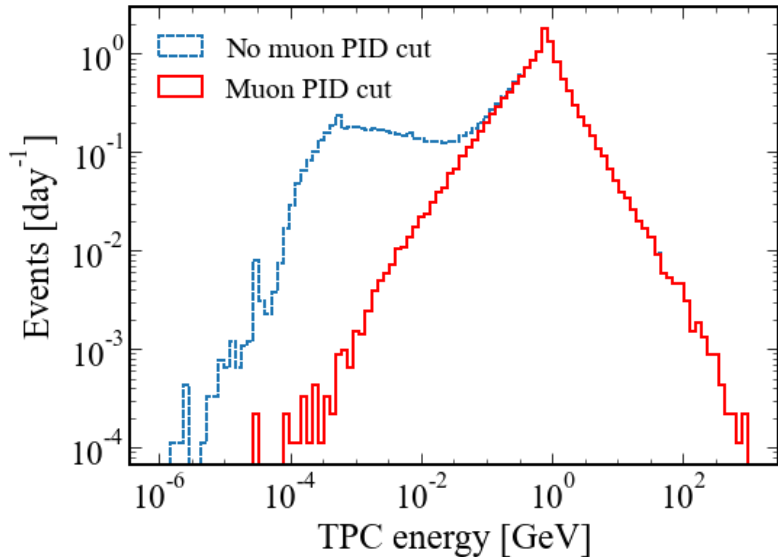


Figure 5.6: Energy deposition spectra of muon events from BACCARAT simulations with and without a muon particle ID (PID) cut. The cut selects events that had a muon depositing energy in the TPC directly.

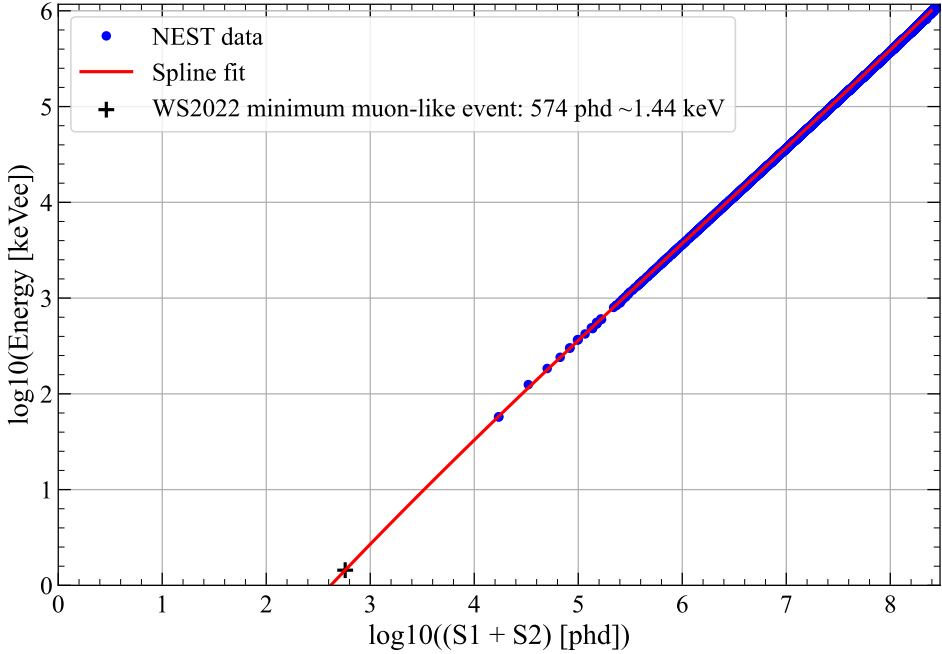


Figure 5.7: Deposited energy from BACCARAT simulations versus the number of detected photons from NEST simulations. The minimum muon-like event found in data is overlaid at 574 phd and the spline fit is extrapolated down to this value.

574 phd that passed our OD energy and inter-detector timing selection. The spline fit was then used to convert the Total Pulse Area observed in a muon event window to energy. To reproduce this conversion using the following parameters in a spline fit, SciPy's `interpolate.BSpline`.

#### WS2022 Parameters

```
t: [0.08294199 0.08294199 0.08294199 0.08294199 4.14709934 8.21125669
8.21125669 8.21125669 8.21125669]
c: [-2.70501286 -1.03606704  1.88505502  4.49568078  5.91208229  0.
0.          0.          0.          ]
k: 3
```

#### WS2024 Parameters

```
t: [0.08294199 0.08294199 0.08294199 0.08294199 4.14709934 8.21125669
8.21125669 8.21125669 8.21125669]
c: [-2.62556966 -0.95670208  1.96474676  4.57569338  5.99200743  0.
0.          0.          0.          ]
k: 3
```

where `t` is the knots, `c` is the spline coefficients and, `k` is the B-Spline degree factor. The spline fit was extrapolated down to 574 phd to obtain a corresponding energy deposition of 1.44 keV. This energy was used as our minimum threshold when determining the TPC threshold.

#### 5.2.4 Comparison Between Data and Simulation

LZLAMA processed the BACCARAT files to convert energy depositions into S1s, S2s and other observed quantities that we could directly compare with the WIMP Search data. However, the decision was made to only use BACCARAT simulations for two reasons: Firstly, LZLAMA is not tuned for highly ionising tracks made by muons through the TPC. The spectrum of the total pulse area in the data was very different from that which LZLAMA produced from BACCARAT, in both the TPC and OD. Conversely, the BACCARAT energy spectra in the TPC and OD

had a very comparable shape to that of the data. Secondly, LZLAMA does not account for secondary particles such as pions and kaons. Initially, LZLAMA halted the processing of a file if it found an unrecognised particle ID in an event, and would move on to the next root file, which caused a great loss in the total number of events. The particle IDs for these error-triggering events were integrated into the LZLAMA source code. As a result, instead of encountering an error, a warning message was generated, quoting the particle ID, and the respective event was skipped over, thus ensuring that the remaining events in the file were not missed. A total of 767 events were missed causing slight bias since this cannot happen in data. In summary, the BACCARAT simulations were found to bear more resemblance to the spectra in data. They were also determined to have less systematic uncertainty than the LZLAMA data for processing muons and their secondary particles. Hence, we shall hereafter focus only on comparing the BACCARAT output to data.

Recording the photon production from muon interactions in the OD, skin and TPC would be too computationally intensive to use NEST as muons are highly ionising, so BACCARAT records only the energy deposited by a muon as it travels through the detector volumes. Consequently, to compare the muon flux of data and simulations, the conversion of pulse area to energy had to be determined. In previous investigations, the relationship between the photons detected by OD PMTs and the energy deposited in the OD was found to be linear at higher energies [45]. On this basis, our conversion factor was estimated by superposing the two spectra and matching the broad peaks of the WS2022 and WS2024 total pulse area spectra with the broad peak of the simulated energy spectrum (in energy units). The conversion factor for both WS2022 and WS2024 is  $6.5 \times 10^{-6}$  GeV/phd. The superposition is depicted in Figure 5.8 where it can be seen how closely the different features of the data spectra (summed) line up with their simulated counterparts.

The cuts introduced in the simulations were designed to mimic those applied to data, namely a coincidence cut where a muon had to pass through each of the OD, skin and TPC within an event; and the 8 MeV energy threshold, previously explained in Section 4.1.

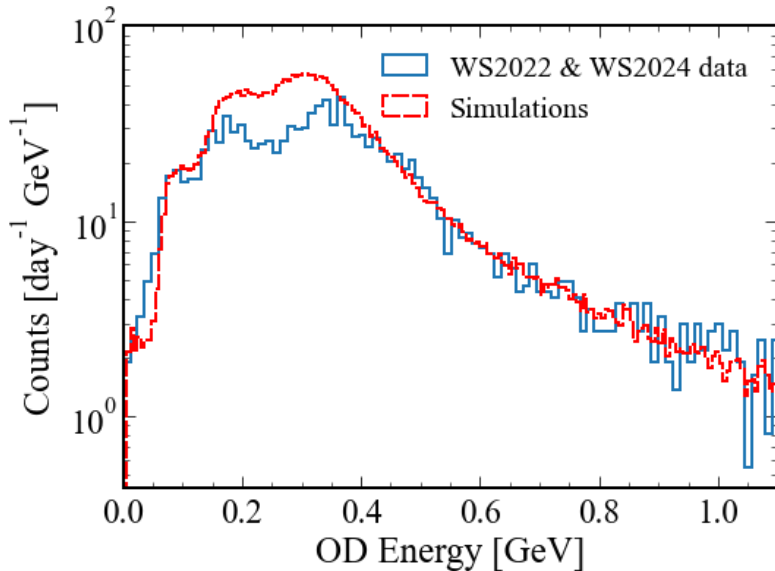


Figure 5.8: Energy deposited by BACCARAT simulated muons in the OD and the energy of events in data converted from the total pulse area in the OD.

After converting both TPC and OD pulse area to energy we were able to directly compare their combined energy maps between simulated results and data. The plots displaying the full energy distributions (after coincidence and OD energy cuts) and similar distributions after the

TPC 10 MeV cut is imposed are in Figure 5.9. Since we cannot distinguish between secondaries of muons and actual muons, we need the cut to ensure that this systematic uncertainty, which is higher at lower energies, is avoided as much as possible. The energy distributions show that the 10 MeV cut removes events with a small amount of energy deposited in the TPC and a large amount of energy deposited in the OD. This is characteristic of muon secondaries or muons that may have skimmed the edge of the TPC.

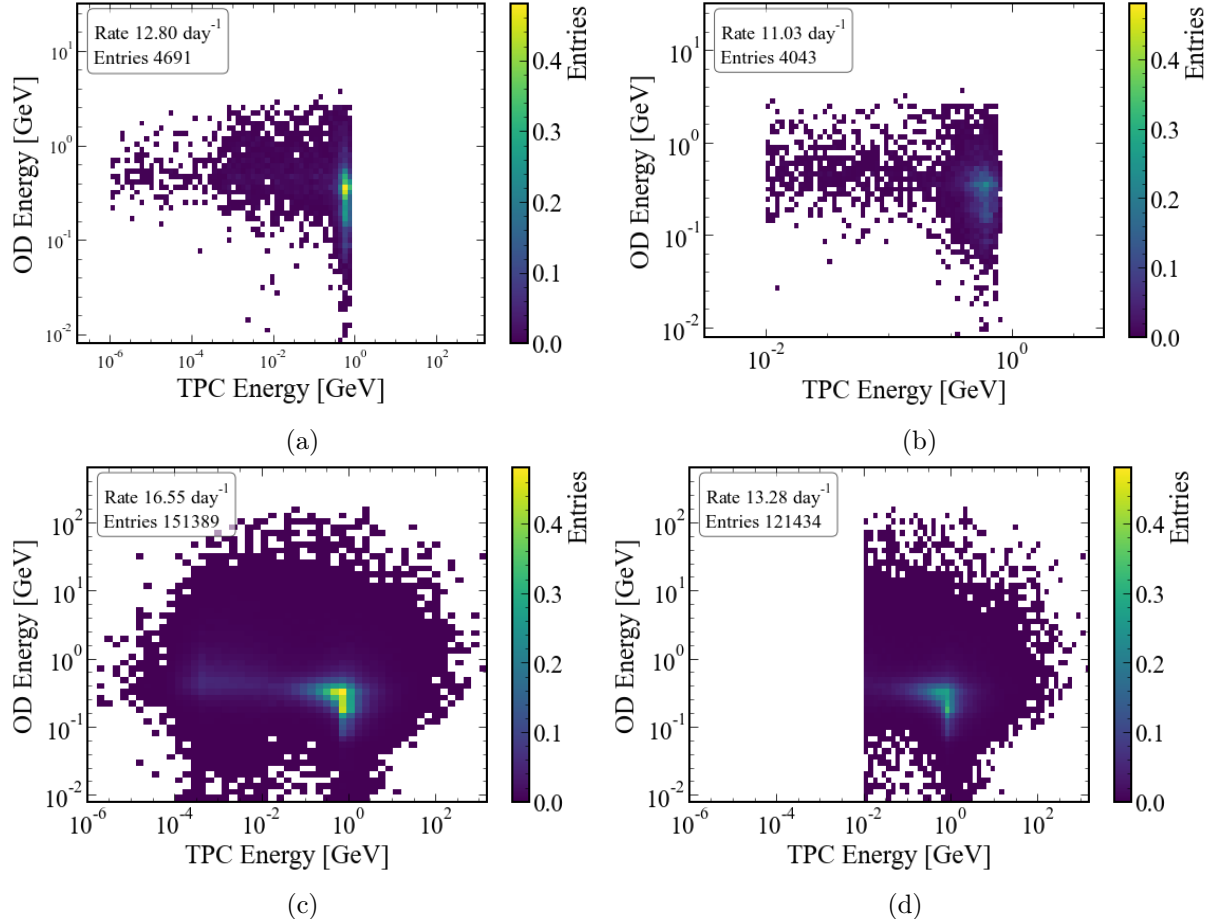


Figure 5.9: Energy depositions from events in the OD and TPC are shown, with the total pulse area from WS2022 and WS2024 data converted to energy. In (a), only OD and inter-detector timing cuts are applied, while in (b), the 10 MeV cut is also included. Similarly, BACCARAT simulations are plotted with the 8 MeV OD energy threshold and coincidence cut in (c), and with the additional 10 MeV cut included in (d).

### 5.2.5 Muon Rate Results

The measured muon rates from simulations, HG and LG data for WS2022 and WS2024 are presented in, respectively, Table 5.2 and Table 5.3 with increasing TPC energy thresholds. By varying the TPC energy threshold (translated from total pulse area via the NEST conversion) the change in the ratio of the simulated muon rate to the muon rate from data can be tracked. Columns 4 and 6 in each table show these ratios for LG and HG data respectively, and they are also displayed in Figure 5.5b. The final column in each table lists the differences between these HG and LG ratios for every threshold. As described in Section 4.3, the steadiness of the LG ratio compared to the HG ratio above 10 MeV was the major factor in our decision to implement a 10 MeV threshold and use LG data for reconstructing the muon flux (see Section 9).

Table 5.2: Muon rates from simulations and WS2022 data. The data has the OD cuts and timing selections applied. The simulations have a 3-fold detector coincidence criteria and the 8 MeV OD energy cut applied. The TPC energy thresholds represent the total energy deposited by a muon event in the TPC.

TPC threshold	Simulation rate [day <sup>-1</sup> ]	Data LG rate [day <sup>-1</sup> ]	Data/sims LG ratio	Data HG rate [day <sup>-1</sup> ]	Data/sims HG ratio	L
TPC > 1.44 keV	$16.550 \pm 0.043$	$12.709 \pm 0.359$	$0.768 \pm 0.022$	$12.780 \pm 0.360$	$0.772 \pm 0.022$	-0.0
TPC > 1 MeV	$15.055 \pm 0.041$	$12.224 \pm 0.352$	$0.812 \pm 0.023$	$12.305 \pm 0.353$	$0.817 \pm 0.024$	-0.0
TPC > 2 MeV	$14.477 \pm 0.040$	$11.940 \pm 0.348$	$0.825 \pm 0.024$	$12.143 \pm 0.351$	$0.839 \pm 0.024$	-0.0
TPC > 5 MeV	$13.760 \pm 0.039$	$11.485 \pm 0.341$	$0.835 \pm 0.025$	$11.546 \pm 0.342$	$0.839 \pm 0.025$	-0.0
TPC > 10 MeV	$13.275 \pm 0.038$	$11.191 \pm 0.337$	$0.843 \pm 0.025$	$11.141 \pm 0.336$	$0.839 \pm 0.025$	0.0
TPC > 20 MeV	$12.840 \pm 0.037$	$10.837 \pm 0.331$	$0.844 \pm 0.026$	$10.625 \pm 0.328$	$0.827 \pm 0.026$	0.0
TPC > 30 MeV	$12.597 \pm 0.037$	$10.655 \pm 0.328$	$0.846 \pm 0.026$	$10.331 \pm 0.323$	$0.820 \pm 0.026$	0.0
TPC > 40 MeV	$12.413 \pm 0.037$	$10.524 \pm 0.326$	$0.848 \pm 0.026$	$10.088 \pm 0.320$	$0.813 \pm 0.026$	0.0
TPC > 50 MeV	$12.258 \pm 0.037$	$10.382 \pm 0.324$	$0.847 \pm 0.027$	$9.886 \pm 0.316$	$0.807 \pm 0.026$	0.0

Table 5.3: Muon rates from simulations and WS2024 data. See the Table 5.2 caption for descriptions of the applied cuts and energy thresholds.

TPC threshold	Simulation rate [day <sup>-1</sup> ]	Data LG rate [day <sup>-1</sup> ]	Data/sims LG ratio	Data HG rate [day <sup>-1</sup> ]	Data/sims HG ratio	L
TPC > 1.44 keV	$16.550 \pm 0.043$	$12.769 \pm 0.218$	$0.772 \pm 0.013$	$12.821 \pm 0.219$	$0.775 \pm 0.013$	-0.0
TPC > 1 MeV	$15.055 \pm 0.041$	$12.063 \pm 0.212$	$0.801 \pm 0.014$	$12.137 \pm 0.213$	$0.806 \pm 0.014$	-0.0
TPC > 2 MeV	$14.477 \pm 0.040$	$11.730 \pm 0.209$	$0.810 \pm 0.015$	$11.838 \pm 0.210$	$0.818 \pm 0.015$	-0.0
TPC > 5 MeV	$13.760 \pm 0.039$	$11.270 \pm 0.205$	$0.819 \pm 0.015$	$11.259 \pm 0.205$	$0.818 \pm 0.015$	0.0
TPC > 10 MeV	$13.275 \pm 0.038$	$10.975 \pm 0.203$	$0.827 \pm 0.015$	$10.941 \pm 0.202$	$0.824 \pm 0.015$	0.0
TPC > 20 MeV	$12.840 \pm 0.037$	$10.624 \pm 0.199$	$0.827 \pm 0.016$	$10.542 \pm 0.198$	$0.821 \pm 0.016$	0.0
TPC > 30 MeV	$12.597 \pm 0.037$	$10.430 \pm 0.197$	$0.828 \pm 0.016$	$10.258 \pm 0.196$	$0.814 \pm 0.016$	0.0
TPC > 40 MeV	$12.413 \pm 0.037$	$10.246 \pm 0.196$	$0.825 \pm 0.016$	$10.052 \pm 0.194$	$0.810 \pm 0.016$	0.0
TPC > 50 MeV	$12.258 \pm 0.037$	$10.134 \pm 0.195$	$0.827 \pm 0.016$	$9.858 \pm 0.192$	$0.804 \pm 0.016$	0.0

Table 5.4: Muon rates from simulations, WS2022 and WS2024 data. See the Table 5.2 caption for descriptions of the applied cuts and energy thresholds.

TPC threshold	Simulation rate [day <sup>-1</sup> ]	Data LG rate [day <sup>-1</sup> ]	Data/sims LG ratio
TPC > 1.44 keV	$16.550 \pm 0.043$	$12.753 \pm 0.187$	$0.771 \pm 0.011$
TPC > 1 MeV	$15.055 \pm 0.041$	$12.106 \pm 0.182$	$0.804 \pm 0.012$
TPC > 2 MeV	$14.477 \pm 0.040$	$11.787 \pm 0.179$	$0.814 \pm 0.013$
TPC > 5 MeV	$13.760 \pm 0.039$	$11.328 \pm 0.176$	$0.823 \pm 0.013$
TPC > 10 MeV	$13.275 \pm 0.038$	$11.033 \pm 0.174$	$0.831 \pm 0.013$
TPC > 20 MeV	$12.840 \pm 0.037$	$10.681 \pm 0.171$	$0.832 \pm 0.014$
TPC > 30 MeV	$12.597 \pm 0.037$	$10.490 \pm 0.169$	$0.833 \pm 0.014$
TPC > 40 MeV	$12.413 \pm 0.037$	$10.321 \pm 0.168$	$0.832 \pm 0.014$
TPC > 50 MeV	$12.258 \pm 0.037$	$10.201 \pm 0.167$	$0.832 \pm 0.014$

### 5.2.6 Reconstruction of the Muon Flux

Reconstruction of the muon flux from the measured muon rate has been done simply by scaling the simulated muon flux by the same ratio as that for the measured-to-simulated rate:

$$F_m = F_s \times \frac{R_m}{R_s}, \quad (5.1)$$

where  $F_m$  and  $F_s$  are the measured (reconstructed from the measured rate) and simulated muon fluxes through a surface of a sphere (unit detection efficiency at all angles), respectively, and  $R_m$  and  $R_s$  are the measured and simulated muon rates through the detector.

This simple scaling is based on the common inputs to the simulation of the muon flux and muon rate, namely, muon energy spectra and angular distributions at SURF. It also relies on the assumption that muon transport through the detector and detector response are correctly simulated in the LZ simulation framework BACCARAT (based on GEANT4 toolkit). Simulating muon-induced cascades and their development in and outside the detector has associated uncertainties that are difficult to estimate. By requiring the energy deposition in the TPC to be greater than 10 MeV, we effectively select events when a muon passes through the TPC and remove a relatively small contribution of events without a muon, when only low-energy secondary particles enter the TPC. No other energy cut is included so all events with a muon in the TPC (both in data and simulations) are considered in the analysis. Simulation of muon track passing through the detector and muon energy loss from ionisation along the track should be handled accurately by GEANT4. The second assumption about an accurate simulation of detector response becomes non-critical because the rate of events does not include information about energy deposition apart from the energy threshold. The ratio of measured-to-simulated rates does not depend much on the energy threshold around and above 10 MeV and the small difference in this ratio with changing the threshold can serve as an estimate of the systematic uncertainty.

A very low energy threshold is used for the skin, only to remove noise events. Similarly, energy threshold and pulse shape analysis in the OD only remove radioactive background and noise events leaving muon events intact. Hence, we do not anticipate any uncertainty linked to the thresholds in the skin or the OD.

The ratio of measured-to-simulated muon rates for low gain in Table 5.4 remains constant within statistical uncertainty for TPC energy thresholds of 5-50 MeV. For the TPC threshold of 10 MeV, this ratio is  $0.831 \pm 0.013$  (stat.)  $\pm 0.008$  (syst.), where systematic uncertainty is estimated from the change in the ratio with changing the threshold by a factor of 2-3. (Note that reducing the threshold will increase the fraction of events when a muon does not enter the detector thus increasing the dependence on simulation details).

Using Equation 5.1, the ratio of  $0.831 \pm 0.013$  (stat.)  $\pm 0.008$  (syst.) and the simulated muon flux of  $6.16 \times 10^{-9} \text{ cm}^{-2} \text{ s}^{-1}$ , we derive the reconstructed muon flux from the rate measurements as  $(5.119 \pm 0.080)$  (stat.)  $\pm 0.049$  (syst.)  $\times 10^{-9} \text{ cm}^{-2} \text{ s}^{-1}$ . This flux agrees well with the measurement in the nearby cavern reported in Ref. [34] ( $(5.31 \pm 0.17) \times 10^{-9} \text{ cm}^{-2} \text{ s}^{-1}$ ).

### 5.2.7 Evaluation of Average Rock Density

The difference in the reconstructed and simulated muon fluxes is primarily due to a different density of rock compared with the initial muon model. We assume here that the surface profile is known with sufficient accuracy and so is the laboratory position. There is a small dependence of the flux on the position within the laboratory but it is below the statistical uncertainty. The dependence of the flux on the rock composition has the second-order effect. If we attribute the lower muon flux in the measurements to the higher average rock density, we can evaluate what the realistic average rock density above and around the LZ location is.

We have calculated the muon flux at SURF with different densities of rock above the laboratory to match the measured (reconstructed from measurements) value. In this case, we used a simple approximation of a ‘flat’ surface profile above the lab taking into account only the Earth curvature (though with negligible effect for the flux at this depth). The simulated muon flux is matched with the measured one assuming the average density of  $(2.78 \pm 0.01) \text{ g/cm}^3$  which is 3.0% higher than initially assumed in the muon model (see Figure 5.10 for the flux dependence on the rock density). The statistical uncertainty of the muon rate measurements dominates the error here. This density is smaller than that reported in Ref. [34] ( $(2.89 \pm 0.06) \text{ g/cm}^3$ ) despite almost the same muon flux. The muon flux has been reconstructed for the place where the measurements of the rate were carried out, namely in the Davis cavern. The flux depends on the position in and around the cavern. For example, the muon flux 7 m above the cavern from where most muons in the simulations originated will be about 3% higher.

## 5.3 Modulation

### 5.3.1 Muon Pulse Shape in the Outer Detector

### 5.3.2 MMS Analysis

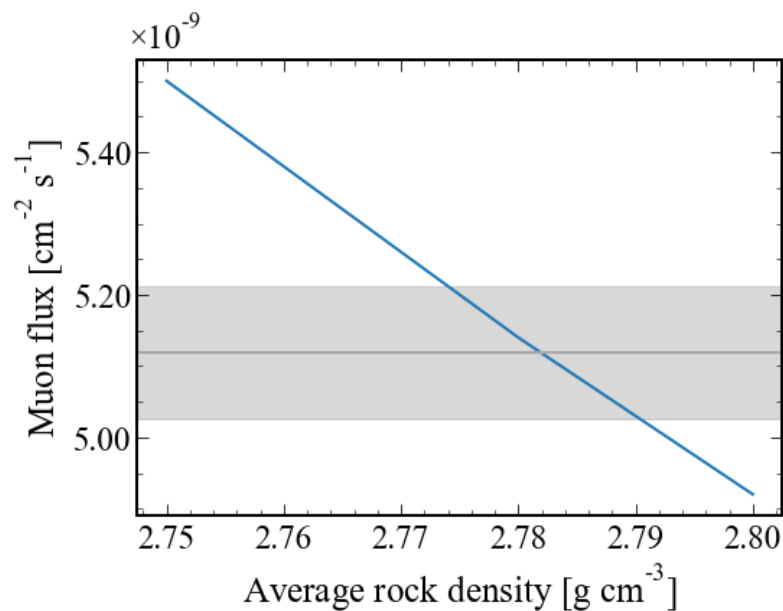


Figure 5.10: The muon flux dependence on average rock density within the muon model. The horizontal line and shaded section mark, respectively, the measured flux value and the combined statistical and systematic errors,  $(5.119 \pm 0.094) \times 10^{-9} \text{ cm}^{-2}\text{s}^{-1}$ .

## **6 Conclusion**

# Bibliography

- [1] J. Aalbers et al. (LZ). “Dark Matter Search Results from 4.2 Tonne-Years of Exposure of the LUX-ZEPLIN (LZ) Experiment”. In: (Oct. 2024). arXiv: 2410.17036 [hep-ex].
- [2] D. S. Akerib et al. “The LUX-ZEPLIN (LZ) experiment”. In: *Nucl. Instrum. Meth.* A953 (2020), p. 163047. ISSN: 0168-9002. DOI: 10.1016/j.nima.2019.163047. arXiv: 1910.09124.
- [3] D. S. Akerib et al. “Identification of Radiopure Titanium for the LZ Dark Matter Experiment and Future Rare Event Searches”. In: *Astropart. Phys.* 96 (2017), pp. 1–10. DOI: 10.1016/j.astropartphys.2017.09.002. arXiv: 1702.02646 [physics.ins-det].
- [4] B. J. Mount et al. “LUX-ZEPLIN (LZ) Technical Design Report”. In: *arXiv* (Mar. 2017). arXiv: 1703.09144 [physics.ins-det].
- [5] Marc Schumann. “Dual-Phase Liquid Xenon Detectors for Dark Matter Searches”. In: *JINST* 9 (2014), p. C08004. DOI: 10.1088/1748-0221/9/08/C08004. arXiv: 1405.7600 [astro-ph.IM].
- [6] L. W. Goetzke et al. “Measurement of light and charge yield of low-energy electronic recoils in liquid xenon”. In: *Phys. Rev. D* 96.10 (2017), p. 103007. DOI: 10.1103/PhysRevD.96.103007. arXiv: 1611.10322 [astro-ph.IM].
- [7] Carl Eric Dahl. “The physics of background discrimination in liquid xenon, and first results from Xenon10 in the hunt for WIMP dark matter”. PhD thesis. Princeton U., 2009.
- [8] Gregory Ransford Carl Rischbieter. “Signal yields and detector modeling in xenon time projection chambers, and results of an effective field theory dark matter search using LUX data”. PhD thesis. Albany U., 2022.
- [9] Peter Sorensen and Carl Eric Dahl. “Nuclear recoil energy scale in liquid xenon with application to the direct detection of dark matter”. In: *Phys. Rev. D* 83 (2011), p. 063501. DOI: 10.1103/PhysRevD.83.063501. arXiv: 1101.6080 [astro-ph.IM].
- [10] D. S. Akerib et al. (LUX-ZEPLIN). “Projected WIMP sensitivity of the LUX-ZEPLIN dark matter experiment”. In: *Phys. Rev. D* 101.5 (2020), p. 052002. DOI: 10.1103/PhysRevD.101.052002. arXiv: 1802.06039 [astro-ph.IM].
- [11] J. Aalbers et al. (LZ). “First Dark Matter Search Results from the LUX-ZEPLIN (LZ) Experiment”. In: *Phys. Rev. Lett.* 131.4 (2023), p. 041002. DOI: 10.1103/PhysRevLett.131.041002. arXiv: 2207.03764 [hep-ex].
- [12] E. Aprile et al. (XENON). “The XENONnT dark matter experiment”. In: *Eur. Phys. J. C* 84.8 (2024), p. 784. DOI: 10.1140/epjc/s10052-024-12982-5. arXiv: 2402.10446 [physics.ins-det].
- [13] S. J. Haselschwardt et al. “A Liquid Scintillation Detector for Radioassay of Gadolinium-Loaded Liquid Scintillator for the LZ Outer Detector”. In: *Nucl. Instrum. Meth. A* 937 (2019), pp. 148–163. DOI: 10.1016/j.nima.2019.05.055. arXiv: 1808.05595 [physics.ins-det].
- [14] Kaito Hagiwara et al. “Gamma Ray Spectrum from Thermal Neutron Capture on Gadolinium-157”. In: *PTEP* 2019.2 (2019), p. 023D01. DOI: 10.1093/ptep/ptz002. arXiv: 1809.02664 [nucl-ex].
- [15] Jun Cao and Kam-Biu Luk. “An overview of the Daya Bay reactor neutrino experiment”. In: *Nucl. Phys. B* 908 (2016), pp. 62–73. DOI: 10.1016/j.nuclphysb.2016.04.034. arXiv: 1605.01502 [hep-ex].

- [16] HAMAMATSU PHOTONICS K.K., Electron Tube Division. [https://hep.hamamatsu.com/content/dam/hamamatsu-photonics/sites/documents/99\\_SALES\\_LIBRARY/etd/LARGE\\_AREA\\_PMT TPMH1376E.pdf](https://hep.hamamatsu.com/content/dam/hamamatsu-photonics/sites/documents/99_SALES_LIBRARY/etd/LARGE_AREA_PMT TPMH1376E.pdf). Accessed: 2025-01-16.
- [17] L. Korley. “The Veto System of the LZ Dark Matter Experiment”. PhD thesis. Michigan U., 2023.
- [18] W. Turner et al. “Optical calibration system for the LUX-ZEPLIN (LZ) outer detector”. In: *Nucl. Instrum. Meth. A* 1010 (2021), p. 165551. DOI: 10.1016/j.nima.2021.165551. arXiv: 2102.06281 [physics.ins-det].
- [19] J. Aalbers et al. (LZ). “The design, implementation, and performance of the LZ calibration systems”. In: *JINST* 19.08 (2024), P08027. DOI: 10.1088/1748-0221/19/08/P08027. arXiv: 2406.12874 [physics.ins-det].
- [20] Masaaki Kobayashi et al. “YAlO<sub>3</sub>: Ce-Am light pulsers as a gain monitor for undoped CsI detectors in a magnetic field”. In: *Nuclear Instruments and Methods in Physics Research Section A: Accelerators, Spectrometers, Detectors and Associated Equipment* 337.2 (1994), pp. 355–361. ISSN: 0168-9002. DOI: [https://doi.org/10.1016/0168-9002\(94\)91103-7](https://doi.org/10.1016/0168-9002(94)91103-7). URL: <https://www.sciencedirect.com/science/article/pii/0168900294911037>.
- [21] H.J. Birch. “Development of the Optical Calibration System for the Outer Detector of the LUX-ZEPLIN Dark Matter Experiment”. Liverpool U., 2018.
- [22] Florian Jörg et al. “Characterization of a <sup>220</sup>Rn source for low-energy electronic recoil calibration of the XENONnT detector”. In: *JINST* 18.11 (2023), P11009. DOI: 10.1088/1748-0221/18/11/P11009. arXiv: 2306.05673 [physics.ins-det].
- [23] J. Aalbers et al. (LZ). “The data acquisition system of the LZ dark matter detector: FADR”. In: *Nucl. Instrum. Meth. A* 1068 (2024), p. 169712. DOI: 10.1016/j.nima.2024.169712. arXiv: 2405.14732 [physics.ins-det].
- [24] Eryk Druszkiewicz (LZ). “The Data Acquisition System for LZ”. In: *JINST* 11.02 (2016), p. C02072. DOI: 10.1088/1748-0221/11/02/C02072. arXiv: 1511.08385 [physics.ins-det].
- [25] D. S. Akerib et al. “Simulations of events for the LUX-ZEPLIN (LZ) dark matter experiment”. In: *Astroparticle Physics* 125 (Feb. 2021), p. 102480. ISSN: 0927-6505. DOI: 10.1016/j.astropartphys.2020.102480. arXiv: 2001.09363.
- [26] S. Agostinelli et al. (GEANT4). “GEANT4 - A Simulation Toolkit”. In: *Nucl. Instrum. Meth. A* 506 (2003), pp. 250–303. DOI: 10.1016/S0168-9002(03)01368-8.
- [27] Matthew Szydagis et al. “A Review of Basic Energy Reconstruction Techniques in Liquid Xenon and Argon Detectors for Dark Matter and Neutrino Physics Using NEST”. In: *Instruments* 5.1 (2021), p. 13. ISSN: 2410-390X. DOI: 10.3390/instruments5010013. URL: <http://dx.doi.org/10.3390/instruments5010013>.
- [28] E.H. Bellamy et al. “Absolute calibration and monitoring of a spectrometric channel using a photomultiplier”. In: *Nuclear Instruments and Methods in Physics Research Section A: Accelerators, Spectrometers, Detectors and Associated Equipment* 339.3 (1994), pp. 468–476. ISSN: 0168-9002. DOI: [https://doi.org/10.1016/0168-9002\(94\)90183-X](https://doi.org/10.1016/0168-9002(94)90183-X). URL: <https://www.sciencedirect.com/science/article/pii/016890029490183X>.
- [29] E.F. Fraser. “Calibration of the Outer Detector, Development of Data Quality Monitoring and Study of Laboratory Backgrounds for Dark Matter Searches with LUX-ZEPLIN”. PhD thesis. Liverpool U., 2022.
- [30] Feng Peng An et al. (Daya Bay). “Measurement of electron antineutrino oscillation based on 1230 days of operation of the Daya Bay experiment”. In: *Phys. Rev. D* 95.7 (2017), p. 072006. DOI: 10.1103/PhysRevD.95.072006. arXiv: 1610.04802 [hep-ex].

- [31] K. Abe et al. (Super-Kamiokande). “Solar neutrino measurements using the full data period of Super-Kamiokande-IV”. In: *Phys. Rev. D* 109.9 (2024), p. 092001. doi: 10.1103/PhysRevD.109.092001. arXiv: 2312.12907 [hep-ex].
- [32] J. Aalbers et al. (LZ Collaboration). “Dark Matter Search Results from 4.2 Tonne-Years of Exposure of the LUX-ZEPLIN (LZ) Experiment”. In: (Oct. 2024). arXiv: 2410.17036 [hep-ex].
- [33] M. L. Cherry et al. “Multiple muons in the Homestake underground detector”. In: *Phys. Rev. D* 27 (7 Apr. 1983), pp. 1444–1447. doi: 10.1103/PhysRevD.27.1444.
- [34] N. Abgrall et al. (Majorana). “Muon flux measurements at the Davis campus of the Sanford Underground Research Facility with the Majorana Demonstrator veto system”. In: *Astropart. Phys.* 93 (2017), pp. 70–75. doi: 10.1016/j.astropartphys.2017.01.013.
- [35] B. Abi et al. “Deep Underground Neutrino Experiment (DUNE), far detector technical design report, Volume II: DUNE physics.” In: *arXiv* (Feb. 2020). doi: 10.48550/arXiv.1512.06148. arXiv: 2002.03005 [hep-ex].
- [36] P. Antonioli et al. “A three-dimensional code for muon propagation through the rock: MUSIC”. In: *Astropart. Phys.* 7 (1997), p. 357. doi: 10.1016/s0927-6505(97)00035-2.
- [37] V. A. Kudryavtsev. “Muon simulation codes MUSIC and MUSUN for underground physics”. In: *Computer Physics Communications* 180 (2009), p. 339. doi: 10.1016/j.cpc.2008.10.013.
- [38] D.M. Mei et al. “Early results on radioactive background characterization for Sanford Laboratory and DUSEL experiments”. In: *Astropart. Phys.* 34 (2010), p. 33. doi: 10.1016/j.astropartphys.2010.04.003.
- [39] C. Zhang. private communication. 2014.
- [40] J. Heise. Preprint: arXiv:1401.0861v1. 2014.
- [41] M. Richardson. PhD thesis (University of Sheffield). 2015.
- [42] T. Gaisser. *Cosmic rays and particle physics*. Cambridge University Press, 1990.
- [43] V. A. Kudryavtsev, E. V. Korolkova, and D. Woodward. *Muon simulations for LZ using MUSIC and MUSUN*. LZ note. 2015.
- [44] Particle data group. *Muons in xenon liquid (Xe)*. data table.
- [45] E. Fraser. *OD Commissioning Energy Calibration*. 2021.